



TECHNISCHE
UNIVERSITÄT
WIEN



Diplomarbeit

Method Development for Characterisation and Classification
of antique silver coins using LIBS and LA-ICP-MS

Durchgeführt am Institut für
Chemische Technologie und Analytik E164,
Technische Universität Wien

Unter Anleitung von
Associate Prof. Dipl.-Ing. Dr.techn. Andreas Limbeck
Univ.Prof. Univ.DoZ. Dipl.-Ing. Dr.techn. Manfred Schreiner

Jakob Willner, BSc
Kudlichgasse 46/14
1100 Wien

Matrikelnummer: 01226233

Wien, 27.08.2019

Willner, Jakob

Eidstattliche Erklärung

Ich erkläre eidstattlich, dass ich die vorliegende Arbeit selbständig und ohne fremde Hilfe verfasst habe, andere als die angegebenen Quellen nicht verwendet habe und die den benutzten Quellen wörtlich oder inhaltlich entnommenen Stellen als solche kenntlich gemacht habe.

I declare that I have written the present work independently and without outside help, that I have not used any sources other than those indicated and that I have identified as such the sources used, either literally or in terms of content.

Wien, 27.08.2019

Willner, Jakob

Danksagung

Nach vielen Jahren bin ich nun endlich am Ende meines Studiums der technischen Chemie angelangt. Auch wenn der Fortschritt im Studium klarer Weise mit viel Arbeit und Mühe verbunden ist, kann ich im Nachhinein sagen, dass es für mich eine Zeit voller neuer Erfahrungen, bunter Ereignisse und schöner Momente war. Zweifellos sind für den schlussendlich Erfolg nicht nur die eigene Bereitschaft, Motivation und Arbeit zu investieren erforderlich, sondern auch Zeit zum Ausgleich, Entspannen und Spaß haben mit den Menschen, die einem wichtig sind.

An dieser Stelle möchte deshalb allen danken, die mich in diesem Lebensabschnitt, sowie davor und hoffentlich auch weiterhin, begleitet haben. Zuerst meinen Eltern Margarete und Willi, die mich immer bedingungslos unterstützt haben, ganz egal welchen Weg ich auch eingeschlagen hätte. Ebenso aufrichtig möchte ich all meinen guten Freunden danken. Die in Salzburg gebliebenen, Sevi, Mo, Clemens, Markus, Novi, und Carina,... danke, dass ihr egal wie lange wir uns nicht sehen mir immer das Gefühl gebt, es wären kaum mehr als eine Hand voller Tage vergangen. Den, wie auch ich, nach Wien ausgereisten, Steve, Clez, Fabi, Selina,... danke für die vielen schönen Stunden und Tage die wir gemeinsam verbracht haben. Zuletzt großen Dank an meine Kollegen aus der Arbeitsgruppe, Andreas, Max, Maxi, Felix, Lukas und Christopher, mit denen ich im vergangenen Jahr viel angenehme Zeit verbringen und von denen ich viel lernen durfte.

Table of Content

Kurzzusammenfassung	7
Abstract.....	10
1 Introduction.....	12
1.1 Historical Background	12
1.2 Previous work.....	13
1.3 Motivation and Objective	15
2 Theoretical Background	16
2.1 Laser Induced Breakdown Spectroscopy (LIBS)	16
2.1.1 Working Principle and Instrumental Setup	16
2.1.2 Laser – Matter Interaction	17
2.1.3 Typical Utilised Laser Sources	17
2.1.4 The Nd:YAG – Laser	18
2.1.5 LIBS – Emission Spectroscopy.....	20
2.2 Laser Ablation – Inductively Coupled Plasma – Mass Spectrometry (LA-ICP-MS)	21
2.2.1 Working Principle and Instrumental Setup	22
2.2.2 Laser Ablation.....	23
2.2.3 Inductively Coupled Plasma (ICP).....	24
2.2.4 Mass Spectrometer	24
2.2.5 Interferences with ICP-MS and Surpass Strategies	26
2.2.6 Isotopic Analysis	27
2.3 Tandem – LIBS/LA-ICP-MS.....	28
2.4 Lead Isotopy.....	29
3 Experimental	31
3.1 Instrumentation	31
3.2 Data Acquisition and Evaluation Tools.....	31
3.3 Samples and Chemicals.....	32
3.4 Sample Preparation	34

3.4.1	Roman Coins.....	34
3.4.2	Reference Materials and Inhouse Standards	34
3.5	Optical Microscopy	35
3.6	LIBS.....	35
3.6.1	Optimisation.....	35
3.6.2	Crater-Depth Determination - Profilometer	35
3.6.3	Sample Measurement	36
3.7	LA-ICP-MS	37
3.7.1	Optimisation.....	37
3.7.2	Liquid Measurement of Reference Materials	37
3.7.3	Sample Measurements	38
3.8	Tandem – LIBS/LA-ICP-MS.....	39
4	<i>Results and Discussion</i>	40
4.1	Optical Microscopy.....	40
4.2	LIBS.....	41
4.2.1	Optimisation.....	41
4.2.2	Measurement of Reference Spectra	42
4.2.3	Crater Depth Determination – Profilemeter	44
4.2.4	Data Evaluation Strategy.....	46
4.2.5	Sample Measurements	47
4.3	LA-ICP-MS	60
4.3.1	Optimisation.....	60
4.3.2	Data Evaluation Strategy.....	60
4.3.3	Liquid Measurements of Reference Materials	64
4.3.4	Sample Measurements	66
4.4	Tandem – LIBS/LA-ICP-MS.....	70
4.5	Example for the Procedure of Data Combination	73
5	<i>Summary and Conclusion</i>	75
6	<i>Outlook</i>.....	77
7	<i>Acknowledgements</i>.....	79

8	Appendix	80
8.1	Listing of Analysed Roman Denarii	80
8.2	μ -XRF and μ -SRXRF Results of Previous Work	86
8.3	Binary Ag/Cu Mixture	88
8.4	Certificates of Purchased Reference Materials.....	89
	List of Tables	91
	List of Figures	92
	List of Equations	94
	Bibliography.....	95

Kurzzusammenfassung

Unser Wissen über vergangene Kulturen basiert neben schriftlichen Überlieferungen zu einem nicht vernachlässigbaren Teil auf Resten jener Zeit wie zum Beispiel Ruinen von Gebäuden, Fundstücken aus Ausgrabungen, Grabbeigaben, Schmuck, Waffen, Währung und vielem mehr. In der Geschichtsschreibung älterer Zeiten fehlt es oft an Details und Chronologie, so dass die erwähnten Überreste für heutige Historiker einen wichtigen Bestandteil darstellen, um die Rätsel vergangener Ereignisse aufzuklären. Ein Thema, das in diesem Zusammenhang von großem Interesse ist, ist die Währung, da Währungsveränderungen durch politisch wichtige Ereignisse wie Führungswechsel, Kriegsbeginn oder -ende oder andere Ereignisse von historischer Bedeutung ausgelöst wurden. Konventionell beschäftigt sich damit die Numismatik, welche das Aussehen, die Münzprägung, die Form, das Gewicht und andere Äußerlichkeiten in einem historischen Kontext untersucht. Moderne Methoden der analytischen Chemie ermöglichen den Zugang zu weiteren Informationen, wie der chemischen Zusammensetzung der verwendeten Materialien, dem Nachweis von Spurenelementen und Verunreinigungen, der Isotopenzusammensetzung, der Phasenzusammensetzung, der Kristallitgröße und -form und vielem mehr. Auf diese Weise können weitere Fragen bezüglich der Rückverfolgung von Rohstoffquellen, zur Beurteilung der Qualität der Raffination und Herstellung sowie zur Klärung der Identität, Gemeinsamkeit oder des Unterschieds von Münzen, die gleich oder sehr ähnlich erscheinen, beantwortet werden.

Die enorme Größe und die lange Lebensdauer des Römischen Reiches führten im Laufe der Zeit zu zahlreichen Veränderungen in der Zusammensetzung seiner Währung, den Denaren. Eine der ersten überlieferten Änderungen fand unter der Regierung Kaiser Traian's (98 - 117 n. Chr.) statt, der eine groß ausgelegte Münz-einsammel- und -umschmelzinitiative organisierte, um die Kriegsvorbereitungen der Daker-Kriege zu finanzieren. Dies macht die Münzen der genannten Periode zu einem interessanten Thema für die chemische Analyse. Diese Arbeit ist auf die Charakterisierung und den Vergleich von Münzen vor, während und nach diesem Ereignis fokussiert.

Im Mittelpunkt dieser Arbeit stand die Methodenentwicklung zur Bestimmung von Haupt-, Neben- und Spurenbestandteilen sowie der Bleisotopenzusammensetzung mittels Laser Induced Breakdown Spectroscopy (LIBS), Laser Ablation – Inductively Coupled Plasma – Mass Spectrometry (LA-ICP-MS) sowie ein Tandem-Ansatz (LIBS / LA-ICP-MS). Die entwickelten Methoden wurden auf 66 Münzen aus der Regierungszeit von Traian und seinem Vorgänger Nerva angewendet.

Die mit LIBS ermittelte Zusammensetzung der Hauptkomponenten Silber und Kupfer sind stellvertretend für die beabsichtigte Legierungszusammensetzung, während Spurenbestandteile (z. B.

Gold, Blei, Wismut) für die Qualität des Raffinationsprozesses sowie der verwendeten Rohstoffe repräsentativ sind. Mittels räumlich aufgelöster Elementinformation (LIBS – Imaging) kann ein signifikanter Unterschied vom Kern der Münzen und der äußeren Schicht beobachtet werden. Diese Befunde geben Hinweise auf die Lagerbedingungen während der letzten zwei Jahrtausende durch das Vorhandensein von Korrosionsprodukten, in welchen typische Erdkrustenelemente wie Silizium, Aluminium, Magnesium, Calcium, Natrium und Kalium vorhanden sind. Durch das Vorhandensein oder Nichtvorhandensein bestimmter Elemente im Münzkern oder der Außenschicht kann auch eine mögliche spätere Nachbehandlung bestimmter Münzen angenommen oder ausgeschlossen werden. Die natürlich vorkommenden Verhältnisse der Bleiisotope ^{204}Pb , ^{206}Pb , ^{207}Pb und ^{208}Pb zeigen lokale Abweichungen von der natürlichen Häufigkeit. Die Bestimmung der Isotopenverhältnisse kann daher zur Zuordnung von Proben zu den zur Herstellung verwendeten Rohstoffen und, sofern Referenzen vorliegen, zu bestimmten Abbaugebieten, verwendet werden. Durch die Analyse der Isotopenverhältnisse der 66 römischen Münzen mittels LA-ICP-MS und den Vergleich der Ergebnisse hinsichtlich des überlieferten Konsulats aus Traians Regierungszeit und der Zeit der ursprünglichen Herstellung konnte festgestellt werden, dass keine klar unterscheidbaren Cluster auftreten. Während einige Münzen der gleichen Herstellungszeit ähnliche Isotopenverhältnisse aufweisen, unterscheiden sich andere erheblich. Diese Ergebnisse legen nahe, dass aufgrund der Größe des römischen Reiches zu dieser Zeit und seiner zahlreichen erfolgreichen Kriegsanstrengungen viele Silberquellen in Form von Minen, aber auch in Form von Beute von Eroberern zur Verfügung standen. Durch Mischen verschiedener Erzquellen mit anderen Silberobjekten und Zusammenschmelzen dieser Erze und Materialien zu Chargen für die Münzherstellung wird die ursprüngliche Bleiisotopensignatur verändert und kann nicht auf die verwendeten Rohstoffe zurückgeführt werden.

Die entwickelten Methoden wurden schließlich zu einer Tandem – LIBS/LA-ICP-MS-Methode kombiniert, die sowohl die Elementzusammensetzung als auch die Bleiisotopenzusammensetzung quasi gleichzeitig unter Verwendung des identischen Probenvolumens erfasst, welches durch das durch die Laserpulse abgetragene Material der Probe definiert wird. Dabei wird die gewonnene Information verhältnismäßig zum Eingriff in die Probe maximiert, was daher unter den entwickelten Methoden die minimal invasive Methode darstellt. Dies ist von großer Bedeutung für die Analyse historischer oder künstlerischer Objekte, da sie aufgrund ihrer Begrenztheit und Einzigartigkeit sehr wertvoll sind. Während bei der Bestimmung des Isotopenverhältnisses in der Tandemmethode einige Nachteile in Bezug auf die Präzision auftreten, welche jedoch durch wiederholte Messungen kompensiert werden können, sind die erhaltenen Emissionsspektren von gleicher Qualität wie bei der Single-LIBS-Methode.

Die gesammelten Informationen werden verwendet, um den Satz analysierter Münzen zu charakterisieren und zu klassifizieren und um ein besseres Verständnis der Geschichte einzelner Münzen zu erreichen. Die LIBS-Ergebnisse zeigen einen signifikanten Unterschied des Münzinneren zur Außenschicht, welche sich häufig durch Verunreinigungen aus der Umgebung und Korrosion hervorhebt und weiters eine Silberanreicherung aufweist. Die erstellten Elementkarten zeigen in den meisten analysierten Münzen inhomogene Elementverteilungen. Weiters sind Einschlüsse im Kern der Münzen charakterisiert. Die ermittelten Bleiisotopenverhältnisse zeigen keinen besonderen Zusammenhang der Münzen in Bezug auf die überlieferten Herstellungszeiten.

Durch weitere geringfügige Optimierungen könnten die entwickelten Methoden auch auf verschiedene Arten von Proben angewendet werden, beispielsweise zur Charakterisierung in verschiedenen Probenmatrizen, zur Identifizierung von Fälschungen oder für technologische Anwendungen.

Abstract

Our knowledge of past cultures is, besides written tradition, for an unneglectable part based on remnants of those times as for example ruins of buildings, findings of excavations, grave goods, jewellery, weaponry, currency and furthermore. Historiography of older times often lacks in detail and chronology, making the mentioned remnants an important piece for nowadays historians to pick the puzzles of past happenings together. One subject of major interest in this context is the currency, because monetary changes were initiated by politically important events as changes of leadership, the start or end of wars or other events of historical importance. Conventional this is examined in the field of numismatics, which studies the appearance, coinage, shape, weight and other externalities in a historical context. Modern methods of analytical chemistry give access to other internal properties, as the chemical composition of the used materials, detection of trace components and contamination, isotopic composition, phase composition, crystallite size and shape and more. Thereby further questions can be answered regarding the tracing of raw material sources, the assessment of the quality of refining and manufacturing, and in terms of clarifying the identity, unity or difference of coins that appear the same or very similar.

The enormous size and the long life time of the Roman Empire resulted in many changes in the composition of its currency, the Denarii, over time. One of the first documented major changes was under the rule of Emperor Traian (AD 98 - 117), who organized a widespread coin collection initiative to fuel the upcoming war efforts of the Dacian Wars, making the coins of the mentioned time span an interesting subject to chemical analysis. This work focuses on the characterisation and the comparison of coins from before, during and after this event.

In this work's focus was the method development for determining main-, minor-, and trace components, as well as the lead isotopic composition, using Laser Induced Breakdown Spectroscopy (LIBS), Laser Ablation – Inductively Coupled Plasma – Mass Spectrometry (LA-ICP-MS) as well as a Tandem approach (LIBS/LA-ICP-MS). The developed methods were applied on a set of 66 coins from the ruling time of Traian and his predecessor Nerva.

The with LIBS determined composition of the main components, silver and copper represent the intended recipe of the alloy, whereas trace components (i.e. gold, lead, bismuth) are representative to the quality of the refining process as well as the used raw material. By obtaining spatially resolved information (LIBS – imaging) a major difference from the bulk of the coins and the outer layer can be observed. These results give hints about the conditions of the storage over the last two millennia through corrosion products, with typical earth crust elements like silicon, aluminum, magnesium,

calcium, sodium and potassium being present. Through presence or absence of certain elements in the bulk or the outer layer also a potential later treatment of certain coins might be assumed or excluded. The with LA-ICP-MS determined ratios of the lead isotopes ^{204}Pb , ^{206}Pb , ^{207}Pb and ^{208}Pb are locally differing from the mean natural abundance. Therefore, the determination of isotope ratios can be used to assign samples to the for manufacturing used raw materials and, if references are available, to certain mining areas. By analysing the isotope ratios of the 66 roman coins and comparing the results with regard to the traditioned consulate of Traian's reign and time of original manufacturing, it could be observed that no clearly distinguishable clusters occur. While some coins of the same manufacturing time show similar isotope ratios, others are significantly different. These results suggest that, due to the size of the roman empire at that time and its numerous successful war efforts, plenty of silver sources were available in form of mines but also in form of loot from conquerors. By mixing different sources of ores with other silver objects and melting them together in batches for coin production, the original lead isotopic signature is disguised and cannot be related back to the used raw materials.

The developed methods were finally combined into a Tandem – LIBS/LA-ICP-MS method, that acquires both the elemental composition and the lead isotopic composition quasi at the same time using the intrinsic identical sample volume, that is defined by the ablated material of the laser pulses. Thereby the gained information is maximised relative to the sample invasion, making the tandem setup to the minimal invasive method. This is of major importance in analysis of historical or art objects, as they are very valuable due to their limitation and uniqueness. While some drawbacks occur in precision of the isotope ratio determination, that can be compensated by repeated measurements, the obtained emission spectra are of the same quality as in the single LIBS method.

The collected information is used to characterise and classify the set of analysed coins and to reach a better understanding of the history of individual coins. LIBS results show a significant difference of the coins bulk to the outer layer, that is often affected by contamination of the surrounding and corrosion and shows silver enrichment. The created elemental maps show inhomogeneous element distribution in most of the analysed coins. Further, particulate inclusion in the bulk of the coins are characterised. The determined lead isotope ratios show no particular classification of the coins relating to the traditioned manufacturing time.

By further minor optimisation, the developed methods could also be applied on different kinds of samples, as characterisation in different sample matrices, the identification of forgeries or for technological applications.

1 Introduction

1.1 Historical Background

The Roman Empire lasted from the eighth century before Christ (BC) until the seventh century after Christ (AD) and had an essential influence in shaping culture beyond the borders of today's Europe, with respect to politics, law, technology, religion, philosophy, art and currency. Beside written traditions and old historical records, our knowledge of this time is for an unneglectable part based on remnants, excavations and finds from that time. Next to buildings, grave goods, tools, weapons, jewellery and more, a major subject of interest is the currency. [1]

Roman coins were produced with various metals and alloys, mostly gold, silver, copper, brass and bronze. The Roman Denarius started out as a coin made of pure silver. In the millennial existence of the Roman Empire, the currency underwent many changes in its appearance and its chemical composition due to political events. It was common that a new emperor reshaped the circulating denarii with illustrations of himself or some icon of belief or an important event. With the growth of the empire and the during passing of centuries, finance politics, inflation and the change of resources and refining processes also lead to the decrease of the finesse. The ever-increasing need for money to finance wars and standing armies to defend borders led to various tricks where emperors tried improve their household by "printing" new money." The decrease in finesse was done by adding more and more copper to the denarii and thus decreasing the material value of the coin. By the end of the third century AD it only contained up to five percent silver. [2], [3]

A period of exceptional interest is the time of emperor Marcus Ulpius Trajanus' reign (AD 98 – 117). Trajan's reign was marked by militant expansion. After the Dacian wars (AD 101/102 and AD 105/106), the annexation of the Nabataean kingdom (AD 106) and the great expansion campaigns to the east until the Persian Gulf (AD 113/117), the Roman Empire reached its greatest expansion ever (Figure 1.1). On one side, to run these wars, Trajan had to take care to provide the necessary finances. On the other side, a giant influx of silver and other resources was gained through plundering after the successful expansion. Both sides are highly related on the silver content of the currency at that certain period. Because of this vast density of historical events, Trajan's rule is one of the preferred subjects of historic and numismatic research. [3], [4]



Figure 1.1: Map of the Roman Empire at its biggest expansion in 117 AD. [5]

A big issue for historical research is the fact, that for this time no continuous written tradition is preserved. An antique biography of Trajan also is not available. One of the only sources of written evidence for these happenings come from a much later collection of unconnected byzantine excerpts called “Cassius Dios” and, as already implied, is not continuously preserved. Though one of those excerpts (by Ioannes Xiphilinos) mentions, that in the early time of Trajan’s emperorship a large scaled smelting initiative was performed. In this situation the coinage remains as the only continuous source through the whole period of Trajan’s ruling, giving access to happenings by numismatic research.

Academic numismatic studies the coins by appearances like size, weight, coinage image and their historical context. Nowadays, by using modern techniques for chemical analysis, further information is accessible because of the possibility to measure the composition of the used materials. Minor and trace components can give hints to a change in resources (metal ore) and the quality of the refining and production process whereas the isotopic composition of certain elements can provide additional information leading to identification of the mining area of the used metal ore. [4], [6], [7]

1.2 Previous work

The already in the in 1860 by Theodor Mommsen published work “Geschichte des römischen Münzwesens” stated, that the silver content of the denarii decreased to about 80 % under Trajan’s rule [8]. This statement was confirmed by Josef Hammer in one of the first metallurgical analyses of Greek and Roman coins [9]. Though only six trajanid denarii had been analysed, that statement was accepted

as a reliable source until in 1970, when David R. Walker started a broad program of analyses of Roman coinage using X-ray fluorescence analysis (XRF). He concluded that the silver content decreased just slightly from approximately 93 % to 88 – 90 % between AD 104 – 107. That result became a new reference point for economic historians studying Trajan’s monetary policy. [10]

Walkers investigation was also invalidated after some years by Butcher and Ponting, showing an average silver content of around 87 % in the second consulate (AD 98 – 99, before the first Dacian War) and only about 80 % in the fifth consulate (AD 104 – 107). Butcher’s error was caused by acquiring only information of the surface with XRF. However, the surface zone was enriched of silver through the way the coins were treated (acid leaching and partial oxidation [11]) in the manufacturing process and therefore is not representative for the complete alloy. [3], [11]

Still, only these two periods have been analysed so far, until a new project was started. The project “*Finances and coinage in the reign of Trajan*”, funded by the Austrian Science Fund (FWF), analysed also three coins of Trajan’s predecessor Nerva and a set of 69 coins through all six consulates of Trajan’s rule. The coins were purchased in two auctions on the free market. The analyses were performed using micro X-ray fluorescence (μ -XRF), micro synchrotron radiation-XRF (μ -SRXRF) and scanning electron microscopy – energy dispersive X-ray analysis (SEM-EDX) on the cross-sections of the coins to gain reliable information of the core composition of the alloys, and first results were published in 2007. Additional to the main components silver and copper, also traces of lead, gold and bismuth were determined. It was shown, that after the second consulate the average silver content of the core alloy decreased from 87 – 93 % to around 80 % (Figure 1.2). These results are in accordance with written tradition of Trajan’s smelting initiative and the assumed preparation time for the first Dacian War.

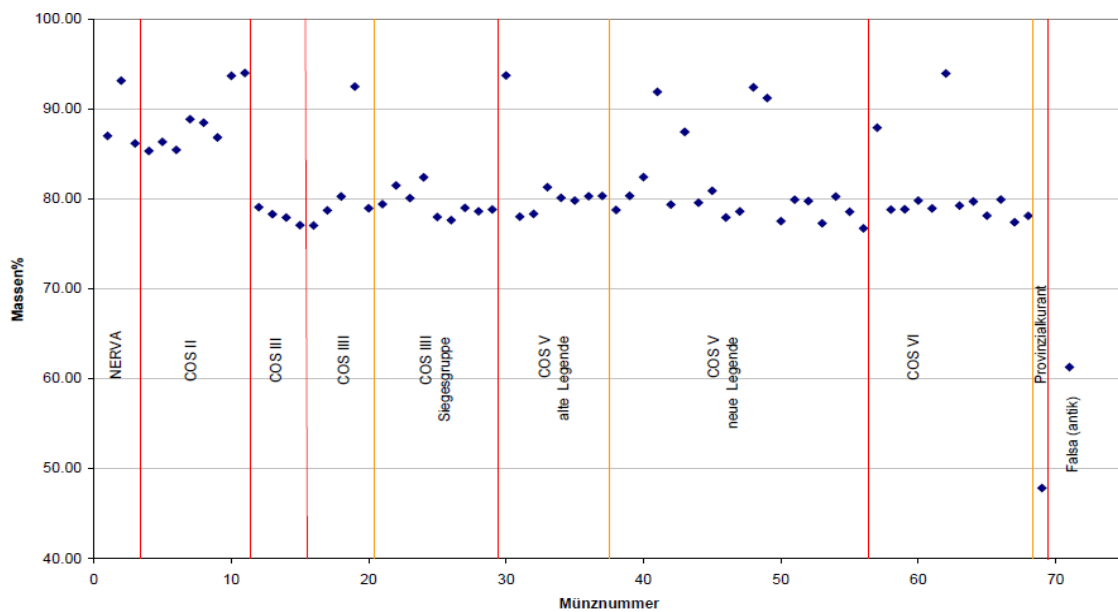


Figure 1.2: Silver content of analysed coins with SEM-EDX. [4]

Further a comparison of the element ratios Au/Ag, Bi/Ag and Pb/Ag has been performed and a change between the fourth and fifth consulate could be observed. This suggests that through the expansion and plundering after the successful wars, new sources of silver ore and silver metal were accessible, leading to a less refined silver bullion supplied to the Roman mint from the fifth consulate on. [3], [4]

1.3 Motivation and Objective

The same coins that have been analysed in the project *“Finances and coinage in the reign of Trajan”* were used in this work. They were received by Prof. Schreiner (Institute of Natural Sciences and Technology in the Arts, Academy of Fine Arts, Vienna), to use for further investigation as subject of a master thesis. As described above, already detailed investigation has been performed, regarding the main components silver and copper as well as traces of lead, gold, manganese and bismuth. SEM-Images of some coins show the silver enriched surface layer, that is due to the old age of the coins also heavily corroded. However, no other than the mentioned elements have been measured and with the used spectroscopic methods, no isotopic information is accessible.

Therefore, in this work, Laser Induced Breakdown spectroscopy (LIBS) is used as a method for multielement determination. Thereby also information about alkali metals (sodium, potassium, ...), alkali earths metals (calcium, magnesium, barium, ...), and transition metals (aluminium, silicon, ...) can be measured simultaneously. Some of them are of special interest concerning the corrosion layer of the coins and give hints about the whereabouts over the last nearly 2000 years. Furthermore, the trace elemental pattern can be used for heritage studies. The second applied method in this work is Laser Ablation – Inductively Coupled Plasma – Mass Spectrometry (LA-ICP-MS), by which lead isotope ratios were measured without sample pre-treatment (digestion in strong acids).

The objective was on one hand, to develop a robust LIBS and LA-ICP-MS method for measurement of archaeological coins and on the other hand to use the entirety of the acquired information to characterise and classify the samples, and further to possibly allow specific statements about individual coins. Because of the high value of antique objects, the method should be minimal-invasive with the best possible gain of sample information. Therefore, a Tandem-LIBS/LA-ICP-MS approach was attempted, where LIBS and ICP-MS data can be acquired simultaneously.

Besides characterisation and classification of coins, the developed method could also be used on other objects after some minor changes. For instance, for determination of forgeries, for provenance studies of non-metallic samples or for technological applications.

2 Theoretical Background

2.1 Laser Induced Breakdown Spectroscopy (LIBS)

Since the invention of the laser in 1960 [12] the requirements for a new method of atomic emission spectroscopy were given. About 20 years later, in the early 1980s, the pioneering work for modern LIBS systems was done by D. A. Cremers and L. J. Radziensky at Los Alamos National Laboratory (USA). From then on, rapid development made LIBS, also related to as laser-induced plasma spectroscopy (LIPS) or laser spark spectroscopy (LSS), to a nowadays very valuable analytical tool with many major advantages. LIBS can give access to all elements of the periodic table in all kinds of solid, liquid and gaseous samples down to the ppm level. Because of relatively little space requirement as well as low operation costs, LIBS is a very attractive method with numerous applications as in quality control, geochemical analysis, forensics, material analysis (metals, ceramics and polymers), biomedicine and cultural heritage studies. [13]

2.1.1 Working Principle and Instrumental Setup

A focused laser-pulse is shot onto a sample. Due to the extremely high energy density a localised plasma emerges at the point of focus on the sample, causing ablation, atomisation and even partial ionisation and excitation. The decay of the excited electronic states leads to the emission of specific radiation, corresponding to the energy difference of the involved electronic states. Through a collection optic the emitted radiation is transmitted to a spectrometer, where it is separated by wavelengths and finally detected. A scheme of a LIBS instrument is shown in Figure 2.1. [13]

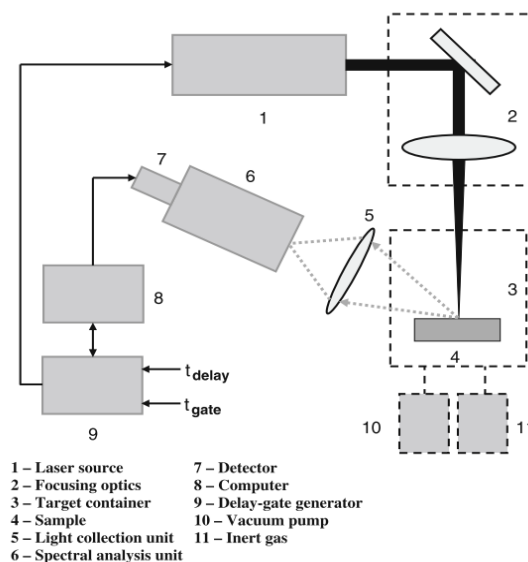


Figure 2.1: LIBS instrumental setup [13].

2.1.2 Laser – Matter Interaction

2.1.2.1 Gases

In general gases interact very weakly with laser radiation. However, given high laser intensities, a strong increase in absorption is observable due to ionisation. There are two effects responsible. At the very beginning of the laser pulse no atoms are ionised and the ionisation potential I is usually several times higher than the energy $h\nu$ of a single photon. But through multiphoton ionisation, the simultaneous absorption of n photons is resulting in the absorbed energy $n h \nu > I$ and therefore promoting an electron into a free state. With a free electron in the laser beam, it can acquire energy from the laser field by the effect of inverse bremsstrahlung. After reaching an energy higher than the ionisation potential I , it can ionise another atom through electron impact, resulting in two free electrons. From then, an avalanche-like ionisation continues until the end of the laser pulse, leading to a plasma. With the degree of ionisation, the plasma's absorption increases and therefore it is heated to several thousand degrees Kelvin, exciting electronic states of present atoms and ions. [13]

2.1.2.2 Condensed Matter

In terms of plasma formation, the interaction of laser radiation with condensed matter follows mainly the same path as with gaseous matter, but with some important differences. Due to the electronic structure of solids, the radiation couples much quicker with the lattice via phonon vibrations and transforms most of the energy into heat. Compared to gases the plasma formation is therefore delayed until vaporisation of the surface atoms occurs, which decouples surface species from the bulk.

In metals the energy is absorbed through free-free transitions of electrons in the conduction band, following the mechanism of inverse bremsstrahlung. In semiconductors it works the same way, provided that the photon energy is high enough to promote an electron from the valence band to the conduction band. If that's not the case, at sufficiently high laser flux, electrons of the valence band can still be promoted to the conduction band via multiphoton absorption. The accumulated energy is then transferred to the phonon system by the decay of the excited states, leading to sample heating, melting and finally vaporisation. The ionisation of the vaporised atoms and ions generates a plasma as previously described for gases, whereas the plasma's expansion properties differ, due to the presence of the solid target material and matrix effects. [13]

2.1.3 Typical Utilised Laser Sources

The most important laser properties for LIBS experiments are pulse energy, wavelength, pulse duration and beam quality factor M^2 . The laser intensity must be high enough to form a plasma. The wavelength is responsible for the absorption behaviour, the energy density, the surface penetration ability with

different samples, the bond breaking and ablation mechanism as well as for the plasma properties. The pulse duration varies from nanoseconds to femtoseconds, whereas the main difference is, that with a nanosecond laser pulse, ionisation, heating and vaporisation all occur during the laser pulse. With femtosecond pulses these phenomena don't occur until the end or after the laser pulse, because the pulse duration is shorter than the electron to ion energy transfer time, the electron heat conduction time and the expansion time. Therefore, thermal damage and the heat affected zone on the sample are much smaller. The beam quality factor describes the deviation of the energy density distribution along the beam cross section from an ideal Gaussian distribution and is usually between 2 and 10 (for Gaussian distribution $M^2 = 1$). [13]

There are various commercially available laser sources with wavelengths ranging from UV - IR, of which a selection is shown in Table 2.1. In this work a frequency multiplied Nd:YAG laser was used for both LIBS and laser ablation (-ICP-MS) and therefore is discussed in more detail.

Table 2.1: Laser sources used in LIBS: [13]

Laser type	Wavelength (nm)	Pulse duration (ns)	Energy/pulse (mJ)
CO ₂ Q-Switched	10.6×10^3	200	100
Er:YAG Q-switched	2.94×10^3	170	25
Nd:YAG	1.064×10^3	4–10	0.1–3
Nd:YAG second harmonic	532	4–8	0.05–2
Nd:YAG third harmonic	354.7	4–8	0.02–0.7
Nd:YAG fourth harmonic	256	3–5	0.01–0.3
Ruby Q-switched	694.3	5–30	1–50
Ruby ps pulse	694.3	10^{-2}	0.01–0.5
N ₂ laser	337.1	3–6	0.1–0.6
XeCl excimer	308	20–30	0.5×10^3 – 10^3
KrF excimer	248	25–35	0.5×10^3 – 10^3
ArF excimer	193	8–15	8–15
Fiber laser—Ytterbium doped	1.03 – 1.08×10^3	5×10^{-5} – 10^3	^a
Fiber laser—Erbium doped	1.53 – 1.62×10^3	5×10^{-5} – 10^3	^a
Ti:sapphire	800	2×10^{-5} – 2×10^{-4}	1–5

^a Depends on both the pulse duration and the pulse repetition rate

2.1.4 The Nd:YAG – Laser

The Nd:YAG laser (neodymium-doped aluminium garnet, Nd:Y₃Al₅O₁₂) is a solid state laser in which Nd:YAG is used as active laser medium. It is operated in continuous or in pulsed mode and its main output wavelength is 1064 nm (near infrared). By principle, the Nd:YAG laser is a four-level laser. That means that four energy states are involved in the process. Thereby radiation at several different wavelengths is emitted, including 1440, 1320, 1120 and 940 nm. [14]

Each laser consists of three principal elements: an energy source, an active medium and an optical resonator. The energy source, in this case a flash lamp, provides the energy, being absorbed by the active medium and leads to population inversion of the quantum states. In the active medium, the Nd-doped YAG rod, the electronic transitions take place, which lead to the emission of characteristic radiation referring to the involved states. The optical resonator consists of two mirrors on both sides

of the active medium and is responsible for reflecting the emitted radiation back into the active medium, leading to more radiation by stimulated emission. On one side of the Nd:YAG rod is a totally reflecting mirror, on the output side a partially reflecting mirror is placed, allowing the laser beam to exit. [14], [15]

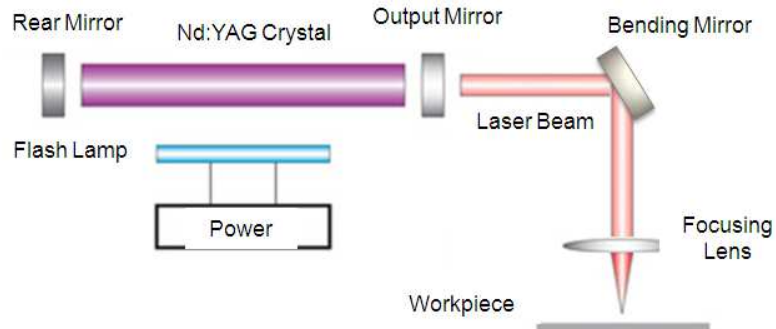


Figure 2.2: Schematic construction of a solid state Nd:YAG laser [15].

There are three ways of photon interaction with the atoms of the active medium: Radiation absorption (Figure 2.3, left) brings electrons from the ground state into a higher energy level. By spontaneous emission (Figure 2.3, right), an excited electron falls back into a lower state, emitting the energy difference of the involved states ($h\nu = E_2 - E_1$).

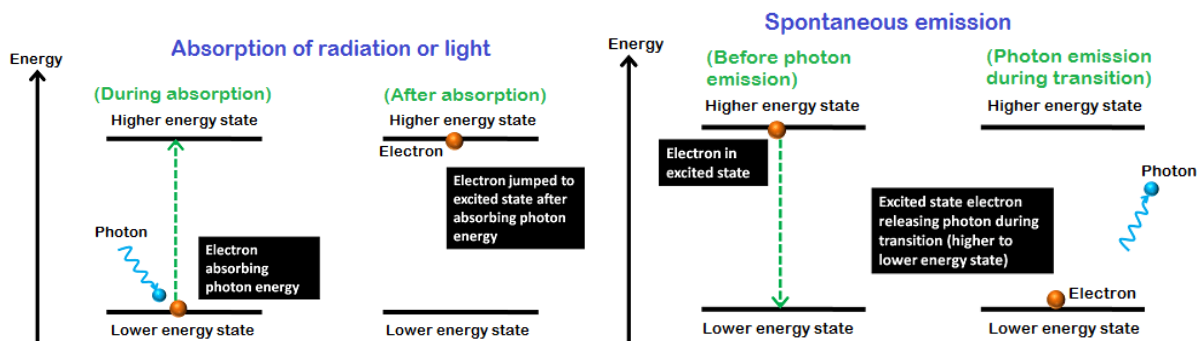


Figure 2.3: Energy scheme for absorption (left) and spontaneous emission (right) [14].

Stimulated emission (Figure 2.4) takes place, when an excited electron absorbs the photon energy, falls back to the lower state and thereby releases two photons.

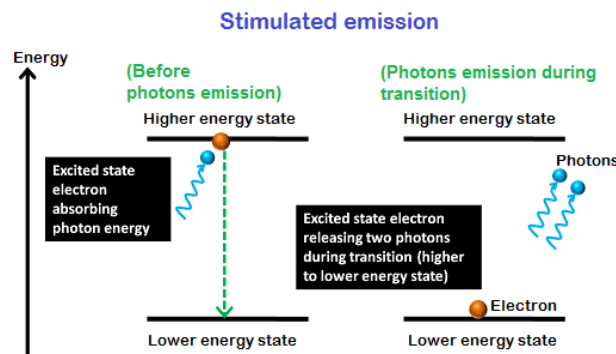


Figure 2.4: Energy scheme for stimulated emission [14].

By frequency multiplying it is possible to produce electromagnetic waves with an integer multiple of the output wavelength [16]. Table 2.1 shows the output wavelength and the second to the fourth harmonic of a Nd:YAG laser. The laser ablation system used in this work was equipped with a fifth harmonic output wavelength of 213 nm, whereas the LIBS/LA Tandem system was operating at the fourth harmonics of 266 nm.

2.1.5 LIBS – Emission Spectroscopy

2.1.5.1 Principle

In most general terms optical emission spectroscopy is a method for the measurement of characteristic emitted electromagnetic waves of a sample due to excitation and consequently decay of electronic states. Excitation is achieved by an external energy source, for example a flame, an electric arc or spark, an inductively coupled plasma or a laser. The emitted radiation is then separated and detected in a spectrometer and enables qualitative and quantitative characterisation of the investigated sample.

In terms of LIBS the energy of a laser is transferred to the sample, forming a plasma which is then further heated up during the length of the laser pulse. This leads to an atomisation of the sample in the plasma and partially ionisation and excitation of both ions and atoms. Depending on the energy, at the beginning, mainly ionic emission lines are emitted, then atomic emission lines of the present elements and at last molecule bands are emitted. When the plasma is cooling down recombination takes place and the formed clusters and molecules are emitting cluster lines or molecule bands. Also, the background signal changes significantly during the evolution of the plasma conditions. Therefore, in LIBS the choice of the time in which the spectra are recorded is an important measurement parameter to optimise the signal to background ratio (S/B) and the signal to noise ratio (S/N) of the area of interest. This is set by the gate delay, which defines the time passing between the laser pulse and the recording of the spectra and is typically set between 0.1 μs and 1 μs for element analytics and > 1 μs for the measurement of molecules. Depending on what sample and which feature is desired to be measured, an optimisation of the system parameters is necessary to achieve a good measurement performance. [13], [17]

2.1.5.2 Spectrometer

The spectrometer consists of a unit to separate different wavelengths of the incident radiation and a detection system. For wavelength separation monochromators or polychromators are used. Both contain diffractive elements, for example a diffraction grating or a prism, to split the wavelengths. A monochromator has an exit slit. At any moment only one selected wavelength reaches the detector and therefore, to record a spectrum, sequential scanning is necessary. With a polychromator the spatially separated wavelengths reach the detector simultaneously. Therefore, a detector array with

pixels is needed to achieve wavelength resolution. This limits resolution compared to a monochromator, but much faster measurement, as well as the measurement of whole spectra of transient signals, is possible.

Figure 2.5 shows schemes of the commonly used Czerny Turner and Echelle polychromators.

The Echelle polychromator has two diffractive elements. The Echelle grating separates incident wavelengths in one spatial dimension and the prism separates different diffraction orders in the perpendicular spatial dimension. Another example for a polychromator is a circular arranged Paschen-Runge-Polychromator.

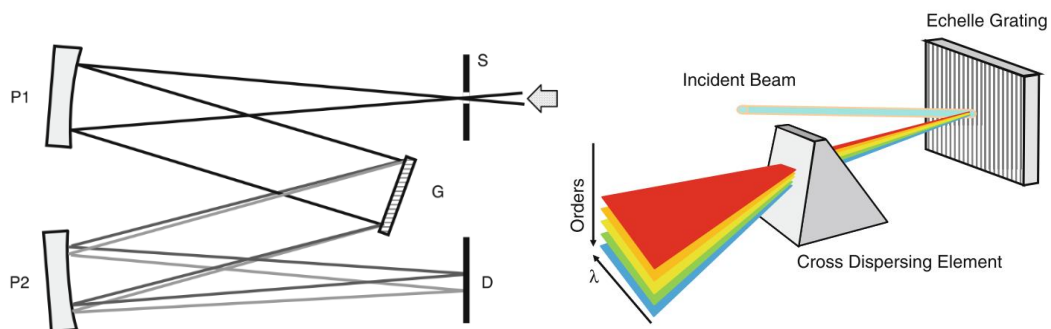


Figure 2.5: Schematic of Czerny-Turner- (left) and Echelle-spectrometer (right). S...entrance slit, P...spherical mirror, G...diffraction grating, D...detector. [13]

After wavelength separation, the electromagnetic radiation is detected and converted to an electric signal. Therefore, commonly used detectors are the Photomultiplier Tubes (PMT), (intensified) Photodiodes or Photodiode Arrays (PD, PDA, IPDA) and (intensified) Charge Coupled Devices (CCD, ICCD).

Various combinations of wavelength separators and detectors are used, differing in sensitivity, triggerability, pixel number, wavelength range, resolution and the cost.

Finally, electronics are used to control the trigger-gated detection. It is responsible for controlling the delay time, to remove the high intensity background signal of the early phase of the plasma formation and for the integration time, for improving the analytical signal. [13]

2.2 Laser Ablation – Inductively Coupled Plasma – Mass Spectrometry (LA-ICP-MS)

After first papers on ICP-MS were published in the 1980s, the first commercially available instrument was introduced in 1983 by PerkinElmer SCIEX [18].

Most elements of the periodic table can be measured with extremely low detection limits down to the ppt-level ($10^{-9} \text{ } \mu\text{g/l}$) and a high dynamic range with linear response. In general solids, liquids and gases can be analysed. The mass resolution, sensitivity, throughput and cost depend on the kind of mass analyser that is used, where each has unique specifications (described in chapter 2.2.4.2).

Mass spectrometry has some major advantages compared to optical methods: The obtained spectra are simple in comparison to optical emission spectra and the sensitivity for most elements is a factor 10 to 1000 higher than with optical methods. Due to isotopic information, the powerful tool of isotopic dilution is accessible for quantification purposes. Because of its possibilities as well as many commercially available systems with fully automated equipment as autosamplers, the ICP-MS is nowadays widely used in analytic laboratories, in industry and university research. Whilst most ICP-MS are equipped with just a liquid sample introduction system, Laser Ablation (LA) is a sample introduction technique for solid sampling, giving the possibility to spare labour-intensive sample digestion and the related cost because of the consumption of high purity chemicals and staff needs. [19]

2.2.1 Working Principle and Instrumental Setup

The sample material is ablated by a high energy laser pulse, which produces a fine particle aerosol. By a carrier gas flow the aerosol is transported to the plasma torch where it is vaporised, atomised and ionised. Through an interface of two cones the ions get from the plasma (normal pressure) into the mass spectrometer (high vacuum). The extracted ions are then separated in the mass filter by their mass to charge ratio (m/z) and finally detected. A schematic setup of a typical LA-ICP-MS is shown in Figure 2.6. In the following sections each part will be explained a little bit more detailed.

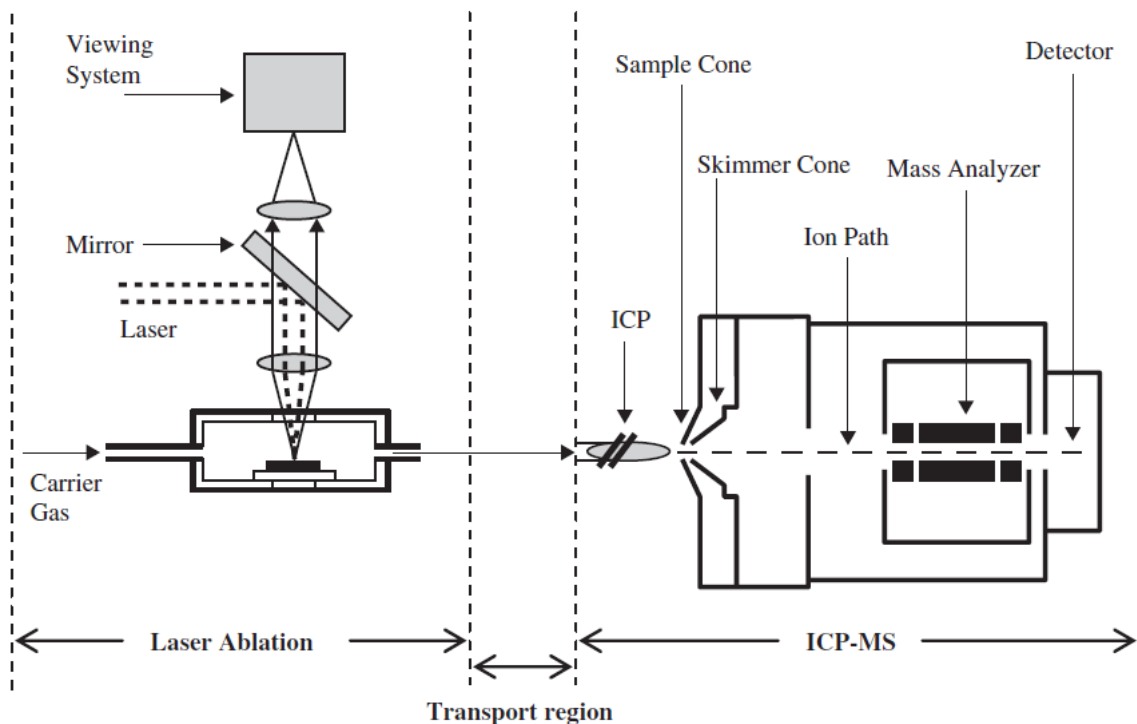


Figure 2.6: Schematic LA-ICP-MS setup. [19]

2.2.2 Laser Ablation

When the ICP-MS coupling first was established, it was used only for gases and liquid analysis. The samples were transported into the plasma by a gas flow after being nebulised to a fine aerosol. Two years later, Alan Gray of the university of Surrey (UK) discovered that the fine aerosol that is necessary for efficient atomisation and ionisation can be generated directly of solid samples using laser ablation. Until today LA has developed into the most versatile solid sampling (SS) method for ICP-MS or ICP-OES. The processes happening when the laser pulse impacts the sample are as for LIBS, described in 2.1.2 Laser – Matter Interaction. However, the effect of interest here is the material ablation and generation of a fine particle-aerosol. Figure 2.7 shows the ablation process and the fine particle-aerosol that is produced after the impact of a laser pulse.

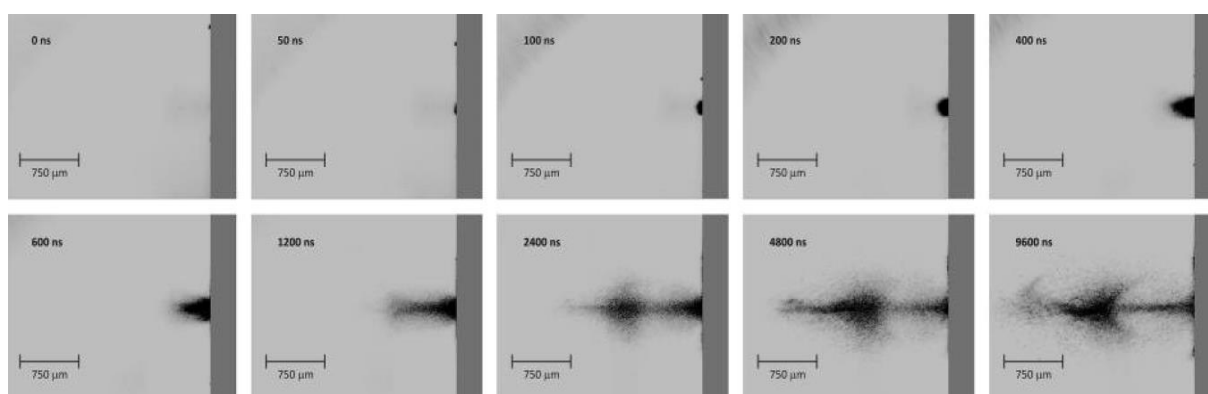


Figure 2.7: Material ablation and aerosol formation after laser impact. [20]

Generally, material from a depth of 0.02 – 5 µm is ablated by one laser shot, depending on laser energy and absorption behaviour of the sample. [19]

Preferably lasers with low wavelengths in the UV are used for LA for following reasons: There is a better and less material depending absorption for the sample and less heat effects occur than with longer wavelengths. Lower wavelengths have a higher photon energy and penetrate the plasma that forms on the sample surface better, leading to more energy being transferred to the surface. Furthermore, the mechanism works by breaking bonds rather than by ablating material through heat effects. This results in a narrower particle size distribution and less elemental fractionation that is caused by different volatility of materials.

Other important factors are the pulse duration and the choice of carrier gas. Shorter pulse lengths in the femtosecond range eliminate plasma shielding, heat effects and elemental fractionation. As carrier gas traditionally Argon, which is also used as plasma gas, was used. Nowadays Helium is used due to better properties regarding ablation and transport and the particle size distribution being shifted towards smaller particles. The lower density of Helium and its higher heat conduction increases the

transport efficiency and the higher ionisation potential leads to a smaller plasma and therefore less heat effects as well as less particle growth through condensation of smaller particles. [19]

2.2.3 Inductively Coupled Plasma (ICP)

After first developed the inductively coupled plasma (ICP) was originally used as for spectrochemical analysis, due to its capability to atomise and excite higher electronic states. In coupling with mass spectrometry its main role is to be the ion source. Therefore, effective vaporisation and atomisation is necessary, because the particles formed by laser ablation can condensate or agglomerate with other particles during the transport to the ICP.

An ICP is formed by an inert gas, most commonly Argon, directed into a plasma torch (Figure 2.8). The plasma torch consists of three concentric quartz tubes. The inner tube carries the carrier gas flow with the sample-aerosol and the middle tube carries Argon to form the plasma, both with flow-rates about 1 l/min. The outermost tube carries Argon with a flow of approximately 15 l/min functioning as cool gas to keep the tip of the torch from melting. Outside this tube a copper coil is applied with a radio frequency (RF), that induces a magnetic field. After an igniting spark, that ionises the first few Argon atoms, the free electrons are accelerated in the magnetic field and collide with more Argon, ionising them and thus forming the plasma. Depending on the position in the plasma, temperature reaches from 5000 to 10000 Kelvin. The frequency of the applied RF is in most commercial instruments either 27.12 or 40.68 MHz with a typical power of 900 – 2000 W. [19], [21]

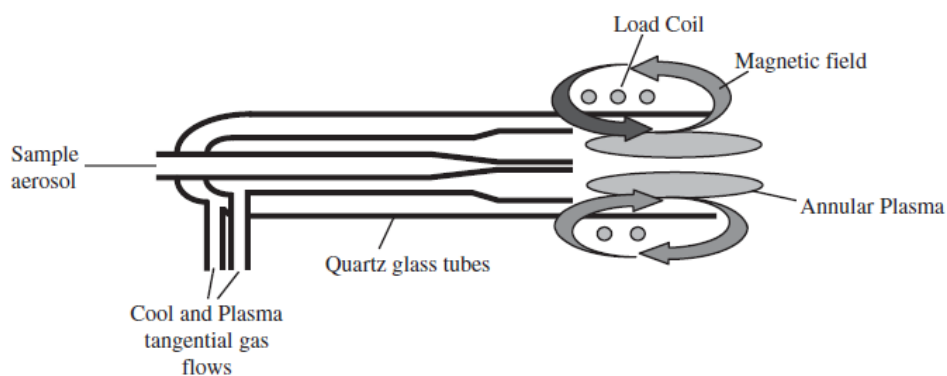


Figure 2.8: Scheme of a typical plasma torch. [19]

The degree of ionisation can be calculated by the Saha-equation, depends on the first ionisation potential of the element and the temperature, and varies from nearly 100 % for alkali and alkali earth elements to about 30 – 0 % for non-metals and noble gases with a high ionisation energy.

2.2.4 Mass Spectrometer

A mass spectrometer (MS) consists of an ion source, a mass analyser and a detector. There are many kinds of different combinations of these and, also coupling techniques of MS with separation

techniques as for example gas chromatography (GC-MS), liquid chromatography (LC-MS) or capillary electrophoresis (CE-MS).

The inductively coupled plasma, which was used as an ion source in this work, was already discussed. Other ionisation techniques are for example electron impact (EI), chemical ionisation (CI), atmospheric pressure photo ionisation (APPI), atmospheric pressure chemical ionisation (APCI), electrospray ionisation (ESI), desorption electrospray ionisation (DESI) and matrix assisted laser desorption ionisation (MALDI). However, most of them are commonly used for organic and biological mass spectrometry.

2.2.4.1 Sample Introduction / Interface

When liquid sampling is performed, the sample aerosol is formed by a nebuliser and carried by an inert gas into a spray chamber, where too big droplets are secreted, and the small droplets are carried into the torch. Using Laser Ablation, the sample aerosol is carried by a gas flow into the centre tube of the plasma torch. The ions formed in the plasma then get through the sample cone into an expansion stage with a pressure of about 2 mbar and then through the skimmer cone into an immediate stage with approximately $10^{-7} - 10^{-8}$ bar, where the ion beam is focused by ion lenses. Then, the different mass-to-charge ratios are separated and detected at the analyser stage with a pressure of $10^{-8} - 10^{-9}$ bar. [19]

2.2.4.2 Mass Analyser

The mass analyser separates ions according to their mass-to-charge ratio (m/z). To separate the ions, a collision free path of the ions is essential, hence a pressure of $10^{-8} - 10^{-9}$ bar is required, varying with the type of mass analyser that is used. Ions entering the mass analyser have a certain energy, velocity and momentum. By determination of a set of two of these properties, m/z can be obtained. Based on this principle many kinds of mass analysers are available differing in resolution, limit of detection, transmission, and cost.

Available mass analysers are the quadrupole-, magnetic sector-, double focusing sector field-, time of flight- and ion trap – mass analysers. In this work a quadrupole was used and therefore is discussed in more detail. [19], [21]

The quadrupole mass filter (Figure 2.9) is built of four electrically conduction rods, with each pair of them placed parallelly and applied to alternating current in radio frequency with a phase shift of 180° . This results in a changing magnetic field between the rods and forces ions onto screw-like path. Depending on the applied frequency, only ions with a certain m/z keep a stable path through the centre

of the rods, the others drift outside and don't reach the detector. The desired m/z ratios are scanned sequentially and thus the ions of interest are not counted simultaneously.

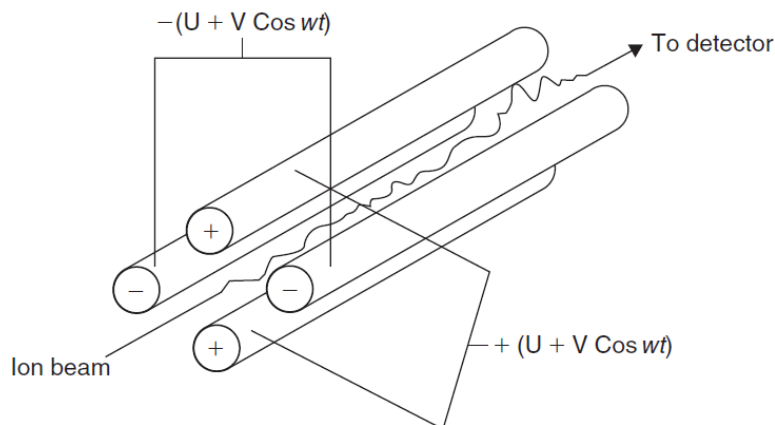


Figure 2.9: Schematic diagram of a quadrupole mass analyser. [19]

This working principle allows a relatively low resolution, being capable of distinguishing a difference of approximately 0.1 - 0.5 atomic mass units. But it is very cheap, has a very high scan speed and, therefore, the quadrupole the most widely used mass filter. [19]

2.2.4.3 Detection

For ion counting two kinds of detectors are used. For high abundances a Faraday Cup is used, which consist of a metal cage and an electrode connected to ground. The charge of the ions reaching the detector are neutralised by electrons flowing from the ground. This leads to a potential drop that allows the measurement of currents down to 10^{-15} A after signal amplification.

To measure currents below 10^{-15} A or to detect single ions, an electron multiplier is required for detection. The ion beam strikes a conversion plate, which converts an ion to an electron. The emitted electrons are accelerated by an applied voltage to a dynode. The dynode is coated with a metal oxide that has a high secondary electron emission. The secondary electrons are again accelerated to the next dynode causing an electron avalanche. With usually 15 – 18 dynodes, an amplification of 10^7 – 10^8 is gained. [19]

2.2.5 *Interferences with ICP-MS and Surpass Strategies*

Spectroscopic Interference is caused, when two species have the same nominal m/z – ratio. This can be the case if either the interfering element is an isotope of another element (isobaric interference), the interfering species is a molecule formed in the plasma, with the same nominal m/z – ratio (polyatomic interference) or if an ion is multiply charged in the ICP and has the same m/z – ratio as a single charged ion that has multiple times less mass. These interferences may be overcome by choosing an alternative isotope of the analyte, but that may result in a loss of sensitivity. Another

possibility is to use a high-resolution mass filter, which can resolve two species with the same nominal m/z – ratio. But because of the very high cost and space requirement of such an instrument, other ways to surpass these problems have been of major interest for research and manufacturers.

Up to now three principal methods are common to this end, called cool plasma operation, reaction cell and kinetic energy discrimination combined with a triple-quadrupole. Cool plasma operation suppresses many polyatomic interferences by limiting the RF-power to about 600 W and using a slightly modified plasma torch that contains a grounded shield. Drawbacks are a less stable plasma and less sensitivity because of decreased ionisation efficiency. In the reaction cell approach, a reaction cell is installed prior to the mass analyser. A gas is introduced in the reaction cell, that either chemically reacts, collisionally dissociates or neutralises the interference with much faster kinetics than the analyte, or the opposite way. The working principle of kinetic energy discrimination is that polyatomic species have a larger collision cross-section, and therefore collide more often with the collision gas than monoatomic analytes, when passing a gas filled chamber. At the exit of the collision cell an energy barrier is installed, thus only species that have enough kinetic energy left can reach the mass analyser. [18], [19]

2.2.6 *Isotopic Analysis*

Isotope ratio measurements were performed since the very beginning of ICP-MS. However, the application range was limited due to rather poor precision compared to thermal ionisation mass spectrometry (TIMS). Since the introduction of the multi-collector ICP-MS (MC-ICP-MS) and the thereby improved precision, ICP-MS is widely used in many fields of research that include isotopic ratio measurements. Typical applications are isotope dilution for calibration in quantitative analyses of all kinds, radioanalytical applications (nuclear energy industry, clinical analytics), isotopic tracer labelling (bio-analytics, clinical analytic), the determination of natural isotope ratios (geochronology and geology) and archaeometric and archaeological applications. Though, as mentioned single-collector ICP-MS is limited in precision, still some tasks can be performed, depending on what precision is required. [19]

Generally, to measure correct isotope ratios, several effects must be accounted for. Fractionation occurs by mass discrimination in sampling, the aerosol transport, the ionisation and the transport of the ions through the interface into the mass spectrometer. At Laser Ablation, a mass fractionation takes place through slightly different volatilities of different isotopes of the same element. On the transport to the ICP, the lighter isotopes have a higher tendency to have contact with the tubing walls and get adsorbed, due to higher diffusion coefficients. Further, when the ions pass over from normal pressure out of the ICP, they enter the sample cone into vacuum and the then skimmer cone into high

vacuum. In this process, the ion beam expands because of the decreasing pressure. Lighter isotopes have less inertia and tend to drift further out of the ion beam than heavier isotopes, and thus less of the lighter isotopes reach the mass analyser and finally the detector. All those effects create an offset of the measured isotope ratio, called bias. [19], [22], [23]

Measured isotope ratios can be corrected for mass discrimination by using external calibration. For that, reference materials with certified isotope ratios are measured and a discrimination factor of empirical models is calculated. Frequently used models are a linear model, a power model or an exponential approach. If no fitting certified reference material is available, materials that are known to have the natural isotopic composition and no locally depending variation can be used. To compensate for instrumental drifts during a series of measurements, the unknown samples should be bracketed by the reference samples. Another approach is to determine the isotopic ratios as delta values. Thereby the isotopic ratios of the sample are subtracted by those of the bracketing standard. [19], [22]

2.3 Tandem – LIBS/LA-ICP-MS

As mentioned in 2.2.4, MS is often coupled to another technique as detector. These techniques are called coupling techniques or tandem techniques. By virtue of the similarity of the required instrumentation for LIBS and LA, it is clear that these techniques can be coupled to Tandem LIBS/LA-ICP-MS. The laser pulse ablates material of the sample surface, forming a particle aerosol and induces a plasma that emits an optical spectrum at the same time. The optical spectrum is collected by the collection optics unit to the LIBS spectrometer and the aerosol is transported by a carrier gas flow into the ICP-MS. This has the main advantage, that the LIBS spectrum and the mass spectrum is obtained quasi-simultaneously, giving more information of the ablated sample volume. Furthermore, with LIBS some elements can be measured, that are not as easily accessible for LA-ICP-MS, which however can access isotopic information.

Nevertheless, it must be said, that parameter optimisation is a compromise of best ablation and aerosol forming conditions versus best plasma forming and excitation conditions. For LIBS, an Argon atmosphere is preferred over Helium. Because of its lower ionisation energy, the Argon plasma emerges bigger and produces more emission. For ICP-MS Helium is preferred, because smaller particles and a narrower particle size distribution is received. In terms of wavelength, slightly longer wavelengths are better absorbed by the plasma, giving it more energy for the excitation of sample atoms, whereas shorter wavelengths penetrate the plasma better and ablate more material that is transported to the ICP-MS. [13], [19], [24]

Because in this work the samples are antique objects, a Tandem setup is of special interest because the resulting minimised invasiveness. Finds of ancient times or art objects are considered very valuable and therefore, destruction during a measurement process is to avoid as far as possible. With a Tandem LIBS/LA-ICP-MS setup, two types of complementary information are gained with a minimal invasive sample consumption.

2.4 Lead Isotopy

Lead (Pb) has the atomic number 82 and three stable isotopes with masses of 206, 207 and 208 atomic mass units (amu). Other lead isotopes (^{202}Pb , ^{209}Pb , ^{210}Pb , ^{211}Pb , ^{212}Pb , ^{214}Pb) are unstable with short half-life and occur only in very low traces. ^{204}Pb is a primordial radio nuclide (of first order), which means that the whole amount of ^{204}Pb was present at the formation of the earth around 4.6 billion years ago. It has a rather long half-life ($t_{1/2} > 1.4 \cdot 10^{17}$ a) and is therefore often considered as stable. ^{206}Pb , ^{207}Pb and ^{208}Pb are the stable end products of the different natural decay chains (Figure 2.10), starting with the radio nuclides ^{238}U (Uranium series \rightarrow ^{206}Pb), ^{235}U (Actinium series \rightarrow ^{207}Pb), and ^{232}Th (Thorium series \rightarrow ^{208}Pb). ^{208}Pb is with a mass of 208 amu the heaviest stable isotope existing. [25], [26]

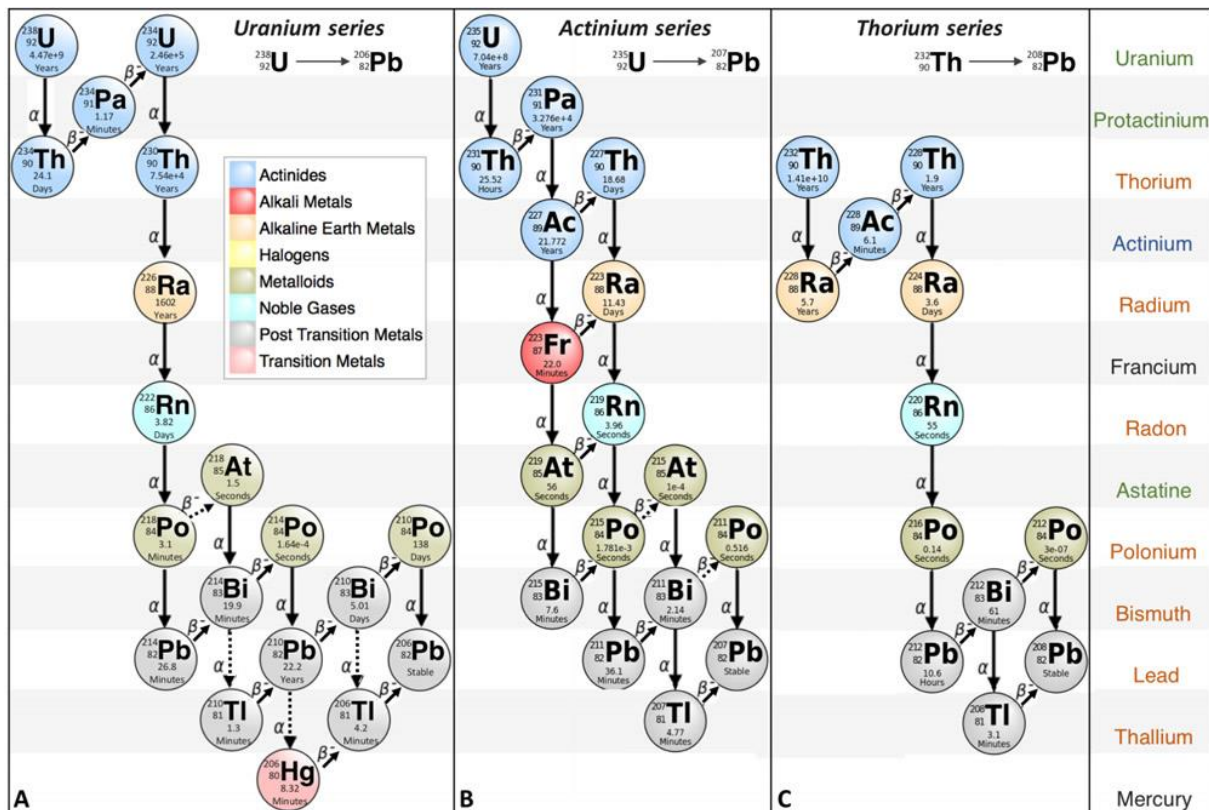


Figure 2.10: Natural radioactive decay chains. [27]

The earth's crust's average lead isotopic composition is listed in Table 2.2. However, through the link with the radioactive decay chains, the isotopic composition of lead ores varies considerably, depending on the ore's age and content of parent isotopes of the decay chains. This leads to significant local differences. An example for the different Pb isotopic composition of mining areas is shown in Figure 2.11. During industrial processing, manufacturing of art objects or even in biochemical processes, the isotopic composition usually is not noticeably changed. This enables the possibility to provide information on the provenance of archaeological objects by measurement of the isotopic composition and comparison with references. Following the same principle, authenticity of art objects can be evaluated. [19], [28]

Table 2.2: Medium abundance of lead isotopes: [29]

Lead isotope	Average abundance
^{204}Pb	1.4 %
^{206}Pb	24.1 %
^{207}Pb	22.1 %
^{208}Pb	52.4 %

For lead, local differences in the isotopic compositions are often big enough, to be measured with a single collector ICP-MS with sufficient precision to allow statements. This makes the measurement of lead isotopy for archaeological studies accessible to a large community, because the clear majority of mass spectrometers in the world are equipped with single channel detection (approximately 99 %). [22]

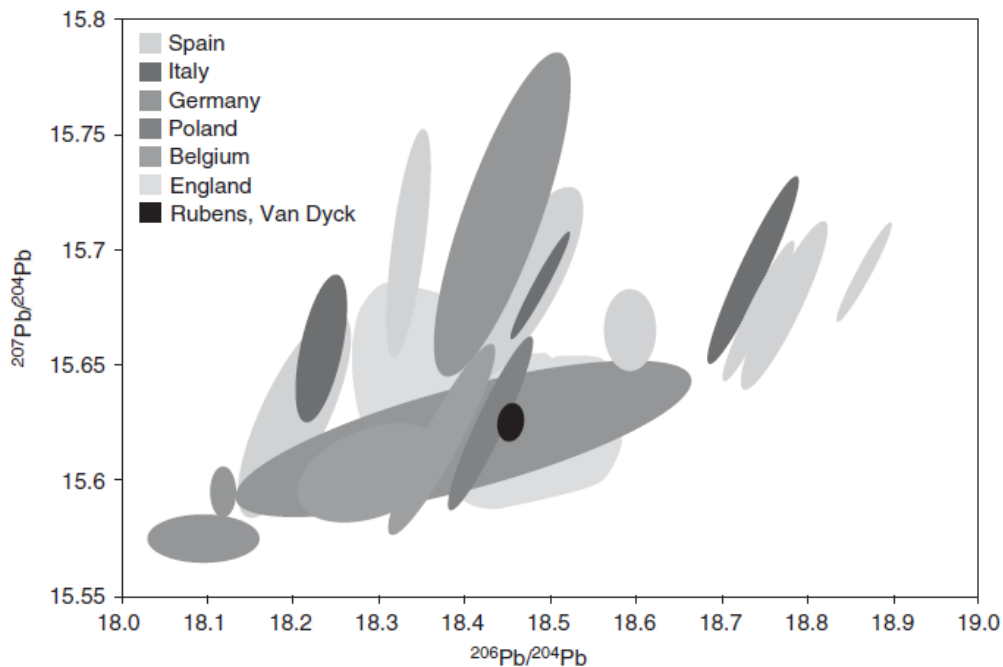


Figure 2.11: Bivariate plot – Isotopic ratios of Pb from different mining areas. [30]

3 Experimental

3.1 Instrumentation

The used LIBS instrument was a Tandem J200 from Applied Spectra (Berkeley, California, USA) was equipped with a frequency quadrupled 266 nm Nd:YAG laser source, a Czerny-Turner spectrometer and a six-channel CCD detection system. The mass spectrometer was a single quadrupole (SQ) ICP-MS instrument of the iCAP series from Thermo Scientific (Bremen, Germany). As an additional laser ablation system, the NWR 213 from ESI's New Wave Research (Fremont, California, USA), equipped with a 213 nm (fifth harmonic) Nd:YAG laser source was used.



Figure 3.1: Tandem J200 LIBS instrument (left), iCAP SQ-ICP-MS instrument (center) and NWR 213 LA unit (right).



Figure 3.2: Olympus GX51 microscope (left) and DektakXT profilometer (right).

Microscopic pictures were obtained with an Olympus GX51 inverse microscope and edited with GIMP 2.10. For morphologic profile measurement the DektakXT profilometer from Bruker was used.

3.2 Data Acquisition and Evaluation Tools

Data acquisition during the measurements was done with the manufacturer's software for all used instruments. The Qtegra 2.10 software by Thermo Fisher was used for ICP-MS data, Aurora v18 by Applied Spectra for LIBS data, Active View by New Wave Research for control of the laser, as well as the Olympus instrument software for the microscope and Bruker instrument software for the

profilometer. Data evaluation was performed for some parts with the instrument software Qtegra (ICP-MS) and Aurora (LIBS), but most parts were done manually with Microsoft EXCEL and OriginPro 2016. The elemental images were created with Epina ImageLab 2.93 and microscopic pictures were edited with the freeware GIMP 2.10.

3.3 Samples and Chemicals

As mentioned in the introduction (1.2), the samples of roman denarii used in this work were already examined in previous work. Therefore, cross-sections have been prepared and embedded in epoxy resin (Figure 3.3). These embedded samples were received from Prof. Schreiner (Academy of Fine Arts, Vienna) and contained a set of 68 denarii through all six consulates of Trajan's rule, as well as three of the period of his predecessor Nerva. A complete listing including numbering of the analysed coins is attached in the Appendix (8.1).

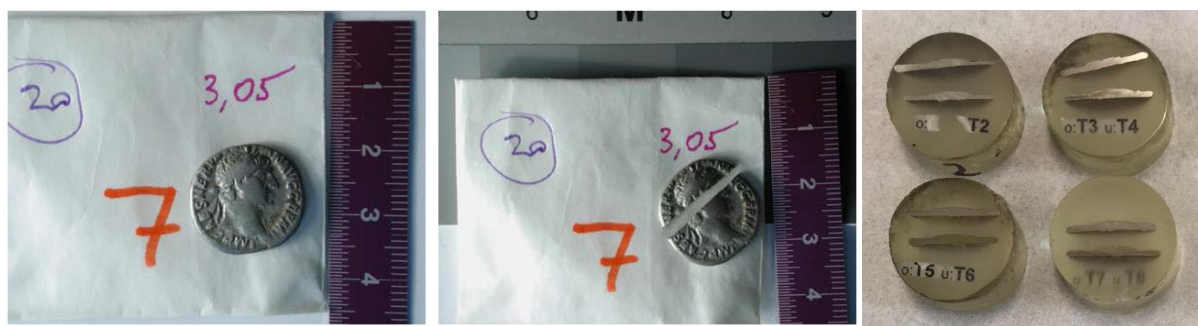


Figure 3.3: Roman denarius: whole (left), cut through (center) [31] and embedded (right).

In order to find non-interfered emission lines of each investigated element for evaluation of the LIBS experiments, pure metals were used to obtain reference spectra. For Pb-isotope measurements, the certified reference material "ERM®-EB400" (hereinafter referred to as "BAM") has been purchased. It consists of scraps of bronze with approximately 94 % copper, 6 % of tin and traces of lead with certified isotope ratios. The certified reference material "133X AGA1" (type: archaeological silver – composition similar to samples, hereinafter referred to as "MBH"), a disk made of a silver alloy with certified amounts of alloying and trace elements, has been purchased and used for both LIBS and LA-ICP-MS experiments. The used standards and reference materials are listed in Table 3.1 and shown in Figure 3.4.

Table 3.1: Used reference materials (numbering refers to Figure 3.4):

Number	Material / Designation	Comments
1	Ag	Sputter target, > 99,999 %
2	Cu	Electrolytically deposited copper on Si-wafer, high purity
3	Au	Sputter target, > 99,999 %
4	Pb	Source unknown ²
5	Zn	Sputter target, > 99,999 %
6	Sn	Sputter target, > 99,999 %
7	Bi	Source unknown ²
8	MBH	Purchased of MBH Analytical LTD, 0.207 ± 0.007 % Pb ¹
9	BAM	Purchased of „Bundesanstalt für Materialforschung und -prüfung“ (BAM), 44.9 ± 2.3 ppm Pb ¹

¹Certificates attached in Appendix (888.3, Figure 8.3, Figure 8.4, Figure 8.4).

²Inhouse Standard.

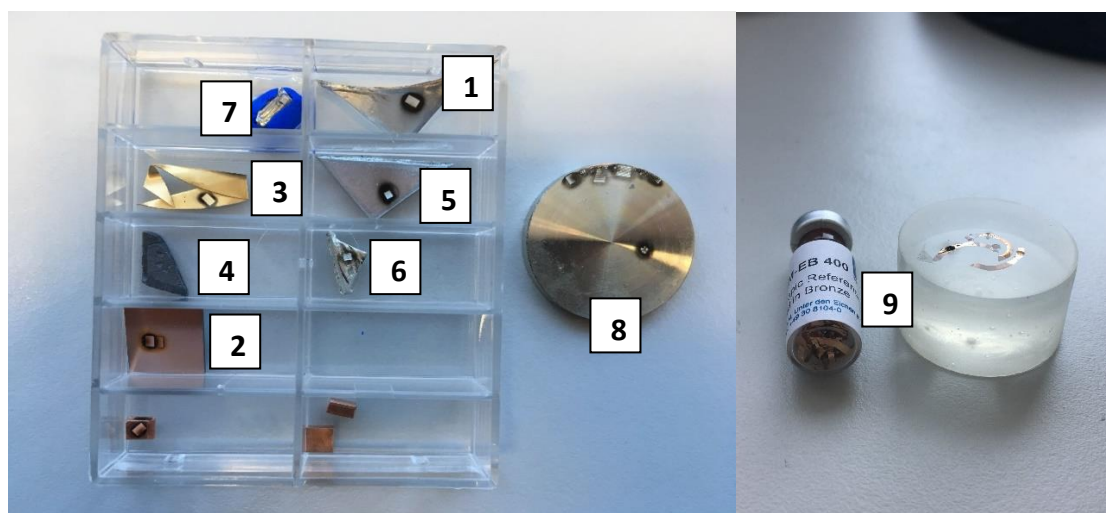


Figure 3.4: Reference Materials: pure metals and MBH (left), BAM - scraps as purchased and after embedding (right). Numbering refers to Table 3.1.

The chemicals that were used for digestion and sample cleaning are listed in Table 3.2.

Table 3.2: Used chemicals:

Chemical	Distributor	Purity
Conc. HNO ₃	EMSURE® Germany	p.a.
Ethanol	EMSURE® Germany	p.a.
Ultra-pure water (>16.2 MΩ)	MilliQ device**	-

*p.a... pro analysis

**reverse osmotic pre-purification followed by fine cleaning step with Thermo Scientific Barnstead EASYPURE II

3.4 Sample Preparation

3.4.1 Roman Coins

To produce reproducible results with laser ablation and LIBS analysis, a smooth and scratch-free surface is required. Therefore, the embedded cross-sections were grinded in a first step with a 2000 mesh abrasive paper and second step with 4000 mesh. Afterwards they were polished on a buff, using a 3 µm diamond paste and lubricant and then cleaned with an ethanol soaked polymer fabric.

3.4.2 Reference Materials and Inhouse Standards

3.4.2.1 Solid Samples

The pure metals (Figure 3.4, no. 1-7) that were used for the measurements of LIBS reference spectra, if non-plane, were flatted, and the surface was polished as described in section 3.4.1. For LA-ICP-MS measurement of the BAM reference material, the scraps were embedded in resin (Figure 3.4, no. 9).

3.4.2.2 Liquid Samples

For liquid Pb-isotope measurements, BAM and MBH were digested using nitric acid. Scraps were cut from the edges of the MBH disc with a scalpel and weighed on an analytical balance into a test tube. The BAM was available as scraps and could directly be weighed. The scraps were dissolved in 0.1 ml concentrated nitric acid at room temperature over 18 hours. After complete dissolution the solution was diluted 1:100 with ultra-pure water to a final volume of 10 ml.

Table 3.3: Sample intakes and resulting concentrations:

Sample	Pb - Concentration in the solid	Sample intake	Pb - Concentration in the stock solution (S)
MBH	2070 ppm	5.3 mg	77.3 mg/l
BAM	44.9 ppm	19.9 mg	6.3 mg/l

The received 1 vol% nitric acid stock solutions were used to produce a dilution series for each of the two reference materials. For dilution 1 vol% nitric acid was used. The sample intakes and resulting concentrations are shown in Table 3.3. The dilution series are listed in Table 3.4.

Table 3.4: Dilution series of dissolved reference materials:

Designation*	Dilution	Resulting concentration
MBH – D1	1 S:12	6.4 mg/l
MBH – D2	1 D1:6	1.05 mg/l
MBH – D3	1 D1:10	105 µg/l
BAM – D1	1 S:6	1.05 mg/l
BAM – D2	1 D1:10	105 µg/l

*S...Stock solution
D...Dilution

3.5 Optical Microscopy

After adjusting the white-balance, the images were recorded in panorama mode in 50x magnification without the use of a filter and with an exposure time of 12 milliseconds. In panorama mode, while scanning the sample, single images are recorded and stitched together to form an image of the whole scanned area. With the acquired images, the coins were checked for scratches and their appearance regarding visible characteristics as layers and inhomogeneities.

3.6 LIBS

3.6.1 Optimisation

Depending on the elements of interest and the nature of the sample, the measurement parameters need to be individually optimised for each method to obtain high intensity and least noise and interference. The optimisation was performed in a way to find fitting measurement parameter, that would allow later coupling with the ICP-MS to a Tandem-LIBS/LA-ICP-MS method. Therefore, helium was chosen as measurement atmosphere, though with argon usually higher intensities are achieved. The MBH-reference material was used for test measurements, setting varying measurement parameters to find an optimal signal-to-noise ratio (S/N). The shot frequency was set to 10 Hz in every experiment. The varied parameters are listed in Table 3.5. The optimised setting of parameters is shown in results section (4.2.1, Table 4.1).

Table 3.5: For S/N optimisation varied measurement parameters:

Parameter	Variation range	Step width
Laser energy	30 – 80 %	10 %
Spot size	50 – 100 μm	10 μm
Gate delay	0.1 – 1.0 μs	0.1 μs

To obtain a minimally invasive method, the influence of the number of accumulated shots for an adequate S/N ratio was investigated.

3.6.2 Crater-Depth Determination - Profilometer

Using the optimised LIBS parameters (Table 4.1), a series of laser pulses were shot on the MBH to determine the material ablation per laser pulse. One up to thirty pulses were fired, each series on a different spot. Three replicates were performed to obtain an average value and a deviation. The resulting craters were measured, using the imaging mode of the Profilometer. The measurement parameters are shown in Table 3.6.

Table 3.6: Measurement parameters of the profilometer:

Image size	2.5 x 1.25 mm
Line distance	10 μm
Scan speed	50 $\mu\text{m/s}$

3.6.3 Sample Measurement

3.6.3.1 Point Measurements

Based on the recorded microscopic images, points of interest were selected on each coin to acquire representative measurements. Spots were set in the core, the corrosion layer and on visible anomalies and inhomogeneities. The measurements were performed with 15 pulses on a single spot using the optimised measurement parameters (Table 4.1). The first five pulses were performed as a pre-ablation step to guarantee a contamination free sample surface and the following ten pulses were used for evaluation.

3.6.3.2 Imaging

The data for the LIBS – images was acquired by selecting a line pattern and scanning the selected regions. While a line is scanned in x-direction, laser pulses are repeatedly shot, and spectra are recorded for each laser pulse creating a pixel of the image. After finishing a line, the next line is scanned with an offset in the y-direction and so on. When the selected region is scanned completely, one layer is finished. More layers are recorded by repeatedly scanning the same pattern. The corresponding parameters are shown in Table 3.7. The laser parameters are shown in the optimisation results (Table 4.1). Of each coin 5 layers have been recorded. Figure 3.5 shows a microscopic image of coin no. 63 before after scanning. The used spot size of the laser of 80 μm refers to the lateral resolution of the raw image and can be seen by the grid size of the laser craters in the coin after scanning (Figure 3.5, below).

Table 3.7: Imaging parameters:

Pattern type	Line Pattern
Repetition rate	10 Hz
Scan speed	1.5 mm/s
Line distance	160 μm
Line length	15 – 25 mm*
Layers	5

*Depending on the size of the imaged coin.

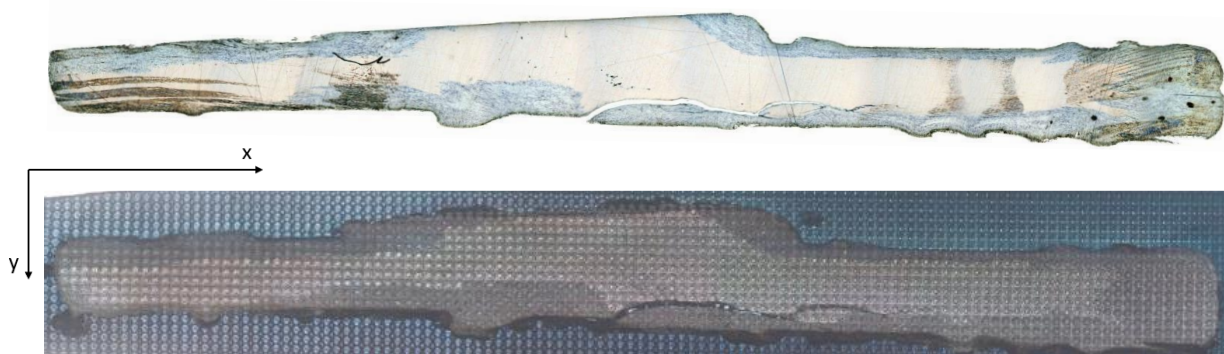


Figure 3.5: Microscopic image of coin no. 63 before (above) and after recording 5 layers of LIBS image (below).

3.7 LA-ICP-MS

3.7.1 Optimisation

Before each measurement session, the signal intensities of ${}^7\text{Li}$, ${}^{115}\text{In}$ and ${}^{238}\text{U}$ is checked by measuring the NIST 612 reference glass with standardised parameters (Table 3.8) and compared to a check list. If the signals were not within the desired regions, an automated system tuning was performed, varying several settings like nebuliser gas flow, extraction lens voltage, detector voltage, plasma torch position and furthermore to acquire maximum ${}^{115}\text{In}$ signal intensity and minimal CeO – rates.

Table 3.8: Standard LA – parameters for signal check and optimisation:

Spot size	80 μm
Laser energy	70 %
Repetition rate	10 Hz
Carrier gas flow	650 ml He/min
Scan speed	5 $\mu\text{m/s}$
Laser warmup	10 s

Regarding the lead isotope measurements, the system was optimised by measuring the MBH with laser ablation and varying the dwell times for each measured isotope using 3, 5, 7 and 10 ms. The laser repetition rate was varied from 10 to 20 Hz, aiming for a minimal standard deviation of the signals.

3.7.2 Liquid Measurement of Reference Materials

The BAM reference material with certified lead isotope ratios only contains 45 ppm Pb. Measured with LA-ICP-MS, the gained signal levels are significantly below 10^6 counts per second for the most abundant lead isotope (${}^{208}\text{Pb} \sim 52.4\%$) and far below 10^5 cps for the least abundant isotope (${}^{204}\text{Pb} \sim 1.4\%$). Due to counting statistics these signal values are not sufficiently high for a precise ratio determination and the BAM could not be used as a bracketing standard for sample measurements. The MBH reference material has 0.2 % Pb and provides enough intensity in LA-ICP-MS, but the lead isotopic ratios are not

certified. As in liquid measurements the signals are much more constant, the ratio determination is more precise. Therefore, the Pb – isotope ratios of the MBH were determined by measuring solutions of the in nitric acid digested BAM and MBH and correcting the obtained values of the MBH according to the bias of the obtained BAM values to the certified values. The MBH could then be used as a bracketing standard for sample measurements with laser ablation.

The solutions were prepared according to section 3.4.2.2 and the measurements settings are shown in Table 3.9. The stock and the dilutions of BAM were split into two and measured twice independently.

Table 3.9: Liquid measurement parameters:

Sample loop volume	1 ml
Sample flow rate	0.4 ml/min
Nebuliser gas	Argon
Nebuliser gas flow rate	0.95 l/min
Measured isotopes	²⁰² Hg, ²⁰⁴ Pb, ²⁰⁶ Pb, ²⁰⁷ Pb, ²⁰⁸ Pb
Plasma power	1400 W
Dwell times	7 ms
Measurement time	120 s

3.7.3 Sample Measurements

Each measurement was performed four times, using line scans with different spot sizes and laser energies. By this procedure data in different magnitudes of intensity was acquired. To minimise the influence of fractionation effects caused by different ablation conditions, the parameters were varied in a way to keep the laser fluence as constant as possible on a value of 4 J/cm². The sample measurements were bracketed by the MBH and BAM reference materials do allow correction for instrumental bias and drift.

The laser ablation parameters are listed in Table 3.11, the ICP-MS settings in Table 3.12.

Table 3.10: LA – parameters of different line scans:

	BAM ¹				MBH ²				Coins ²			
Line no.	1	2	3	4	1	2	3	4	1	2	3	4
LE ³ [%]	100	80	50	100	50	50	50	50	50	50	50	50
Spot size [µm]	100	100	100	200	80	50	25	10	80	50	25	10

¹spot: focused beam

²spot: imaged aperture

³LE...Laser energy

Table 3.11: LA – parameters of all line scans:

Laser fluence	4 J/cm ²
Repetition rate	20 Hz
Carrier gas	Helium
Carrier gas flow	650 ml/min
Scan speed	5 μm/s
Laser warmup	10 s

Table 3.12: ICP-MS – sample measurement parameters:

Nebuliser gas	Argon
Nebuliser gas flow rate	0.8 l/min
Plasma power	1400 W
Measured isotopes	²⁰² Hg, ²⁰⁴ Pb, ²⁰⁶ Pb, ²⁰⁷ Pb, ²⁰⁸ Pb
Dwell times	7 ms
Measurement time	120 s

3.8 Tandem – LIBS/LA-ICP-MS

The embedded samples were put in the sample chamber of the LIBS instrument. The sample chamber was flooded with 0.8 l/min helium and the gas outlet was connected to the plasma torch of the ICP-MS with a PTFE tube. The LIBS parameters were set according to Table 4.1 except for the pulse repetition rate, which was set to 5 Hz because with the maximum of 10 Hz, the signal intensities on the ICP-MS were too high. The ICP-MS parameters were set according to Table 3.12 and the total data acquisition time was 20 seconds. 15 laser pulses were performed for each sample measurement, resulting in a signal time of approximately three seconds plus the additional washout time. All measurement spots were set in the cores of the coins. On each sample 15 up to 20 spots were measured in the selected region. The measurement sequence is shown in Table 3.13.

Table 3.13: Measurement sequence for Tandem – LIBS/LA-ICP-MS experiments:

Sample	MBH	Coin 45	Coin 26	Coin 71	Coin 45	Coin 72	MBH
No. of Spots	15	15	20	20	15	20	15

4 Results and Discussion

4.1 Optical Microscopy

Figure 4.1 shows the microscopic images of cross sections of selected coins. The polymer matrix was removed out of the images by masking it with the GIMP imaging software. It can be observed, that the cross-sections of the coins vary strongly in their appearance. Visible characteristics are the cores of the coins, containing the composition of the original alloy, corrosion layers and inhomogeneous sections inside the coins.

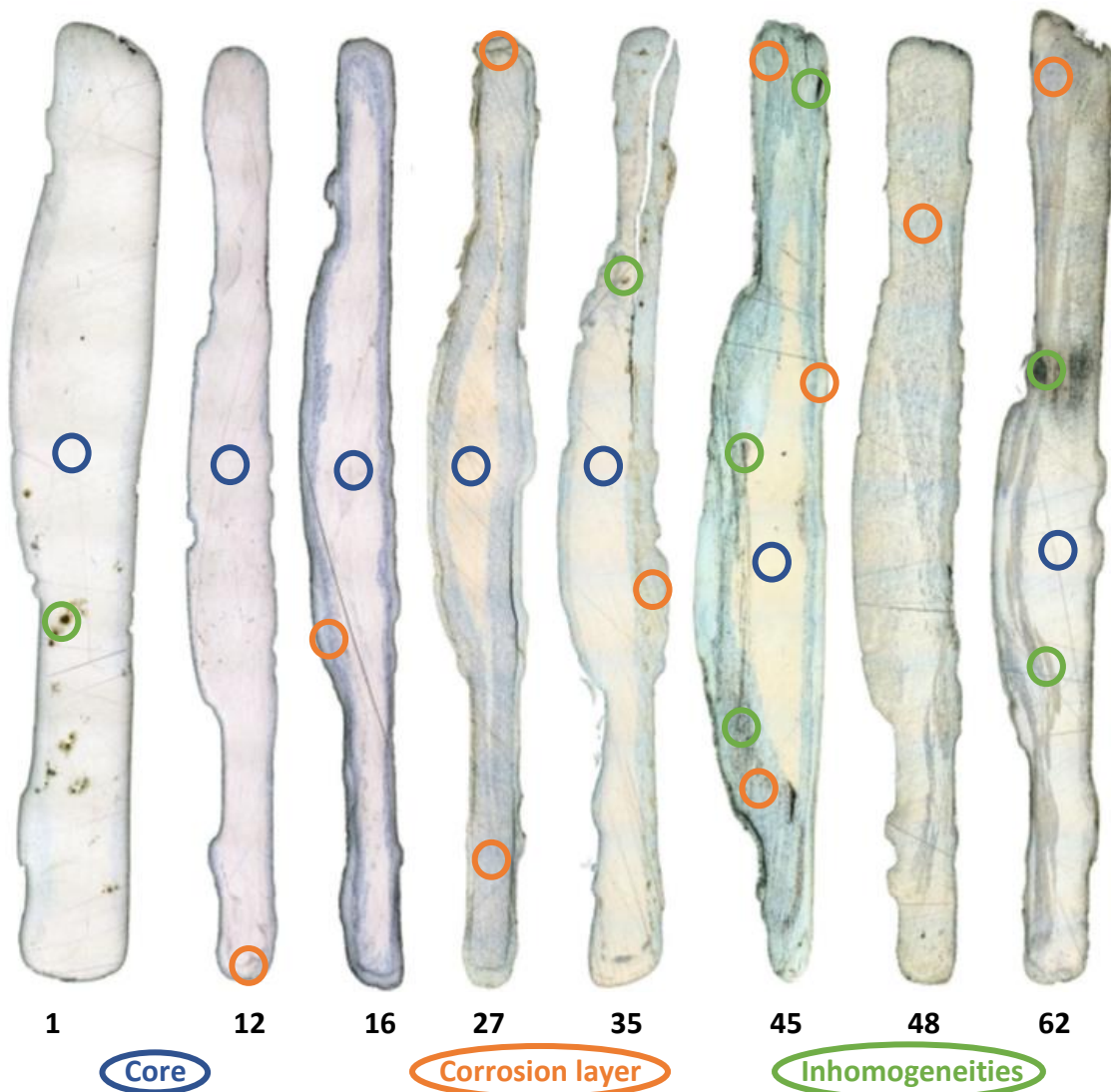


Figure 4.1: Microscopic images of selected coins in 50x magnification (left to right: no. 1, 12, 16, 27, 35, 45, 48, 62).

The corrosion layers appear blueish and vary in their thickness, from nearly not present (coins no. 1 and 12) up to nearly through the entire coin (no. 48). In some coins two layers with different appearance can be seen (coins no. 16, 27 and 45) and some coins show inhomogeneous parts, that

could be inclusions or precipitates. By analysing selected spots of the coins with LIBS, more precise statements about the composition of visible characteristics can be made (see in section 4.2.5).

4.2 LIBS

4.2.1 Optimisation

The optimisation was carried out by repeatedly performing measurements on the MBH reference material with varying laser parameters (Table 3.5), aiming for maximum intensity, as well as possibly low standard deviation in repeated measurements, of selected silver and copper emission lines. The selected lines are shown in Figure 4.2 (section 4.2.2).

The best results with and optimal S/N – ratio could be obtained with the parameters that are listed in Table 4.1.

Table 4.1: Optimised LIBS parameters:

Spot size	80 μm
Beam	focused
Laser energy	50 %*
Gate delay	0.3 μs
Gate width	1.05 ms

*100 % \pm 30 mJ pulse energy

With ten accumulated shots, a sufficient S/N – ratio could be received. Therefore, further point measurements were done with 15 pulses, whereby the first five pulses were done as pre-ablation to guarantee a contamination-free surface and pulse 6 -15 were accumulated.

4.2.2 Measurement of Reference Spectra

Additional to the main components silver and copper, further elements as lead, gold and bismuth are already known to be present in the coins from previous work. In order to evaluate those elements using LIBS and to create images showing their distributions in the samples, reference spectra of the pure metals were recorded. Because the majority of the emission lines of these elements interfere with one another, non-interfered lines were searched for to allow evaluation by clear assignment of an emission line to one element of interest. Sections of the reference spectra with marked non-interfered emission lines, that were chosen for evaluation, are shown in Figure 4.2. The spectra were recorded with the optimised parameters shown in Table 4.1.

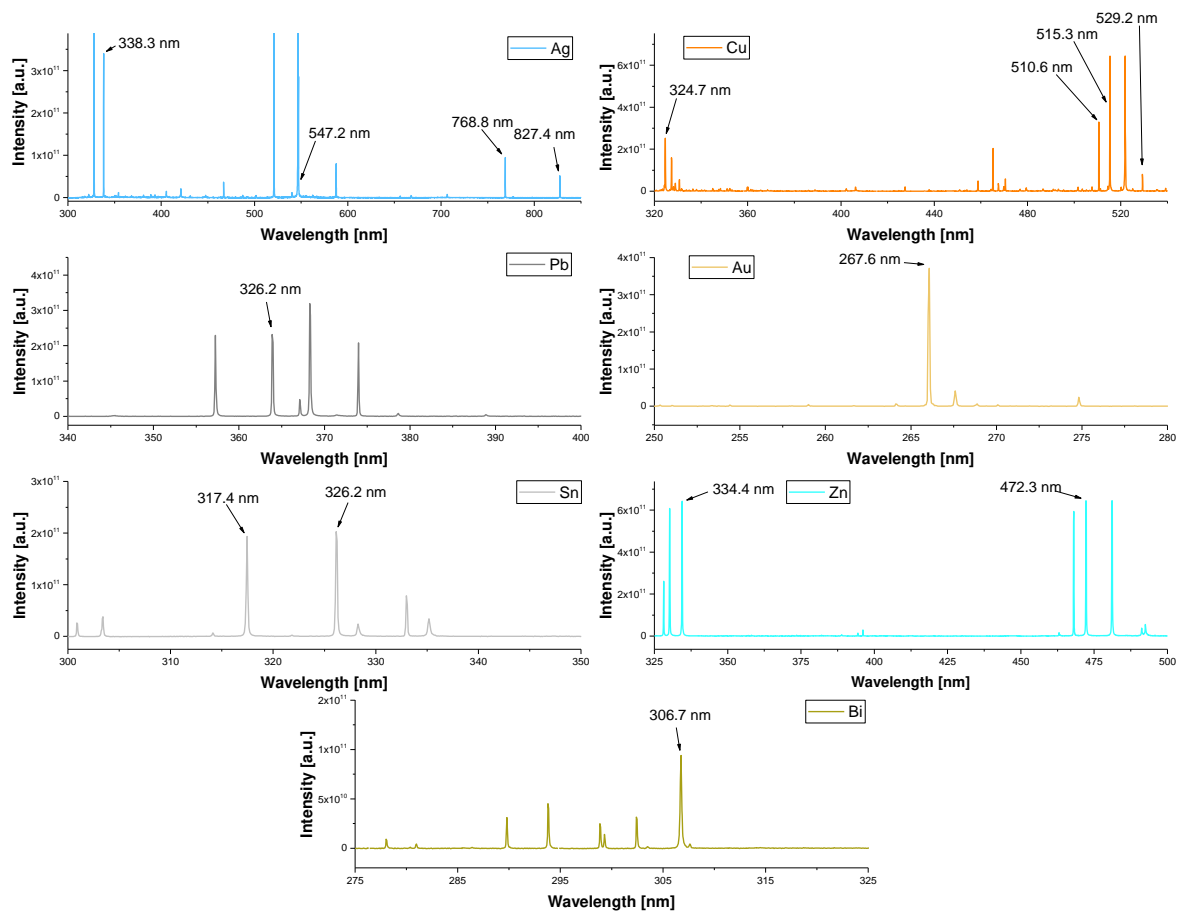


Figure 4.2: Section of the LIBS reference spectra of pure metals with markings to the evaluated emission lines.

Several more elements were to be expected in the outermost, corrosion affected layers of the coins that were in contact with the environment for nearly two thousand years. The corrosion layers of a set of coins were analysed and the emission lines of interest were identified and assigned using the NIST LIBS database as a reference [32]. The total spectra of coin no. 53 (measurement spot shown in a black sphere in Figure 4.3) and the MBH reference material are shown in Figure 4.4. The differences that can be observed in the unmagnified spectra are mostly caused by strong differences in the concentrations of the main components silver and copper.



Figure 4.3: Microscopic image of coin no. 53 (COS V, approx. AD 110) with measurement spot marked as black circle. The corresponding spectra is shown in Figure 4.5 and enlarged sections of interest in Figure 4.5.

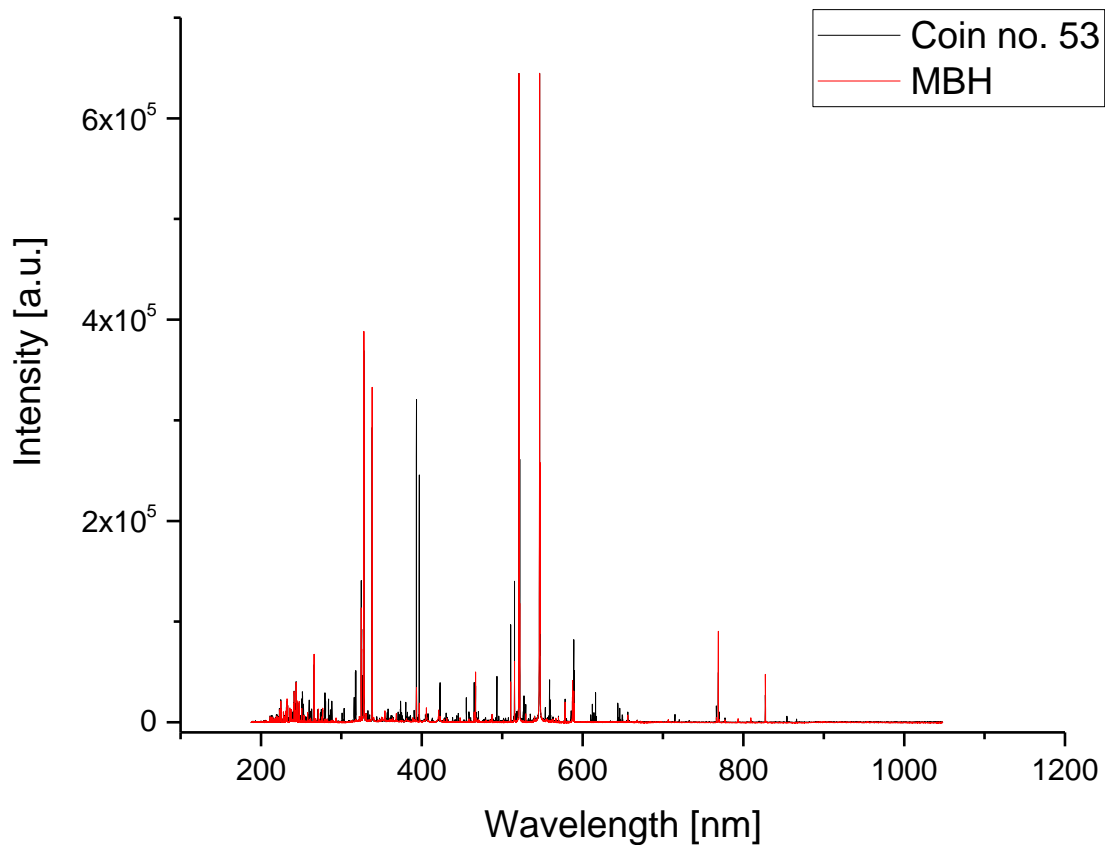


Figure 4.4: Total LIBS spectra of coin no. 53 and MBH.

Figure 4.5 shows sections of the spectra with the not interfered emission lines of sodium, potassium, calcium, magnesium, barium, silicon and aluminium marked. Sodium, calcium and potassium is present in the MBH, though it is not certified as component. This is most probably caused by contamination through sample handling. It can be observed that the signals of these elements are much higher in the spectra of coin no. 53, where it is assumable to be a component in the corrosion layer. In contrast to

the spectra of the MBH, in the coin's spectra also magnesium, silicon, aluminium and barium can be seen. These are elements that are typically present in the earth's crust and environment part of the coin's corrosion layer.

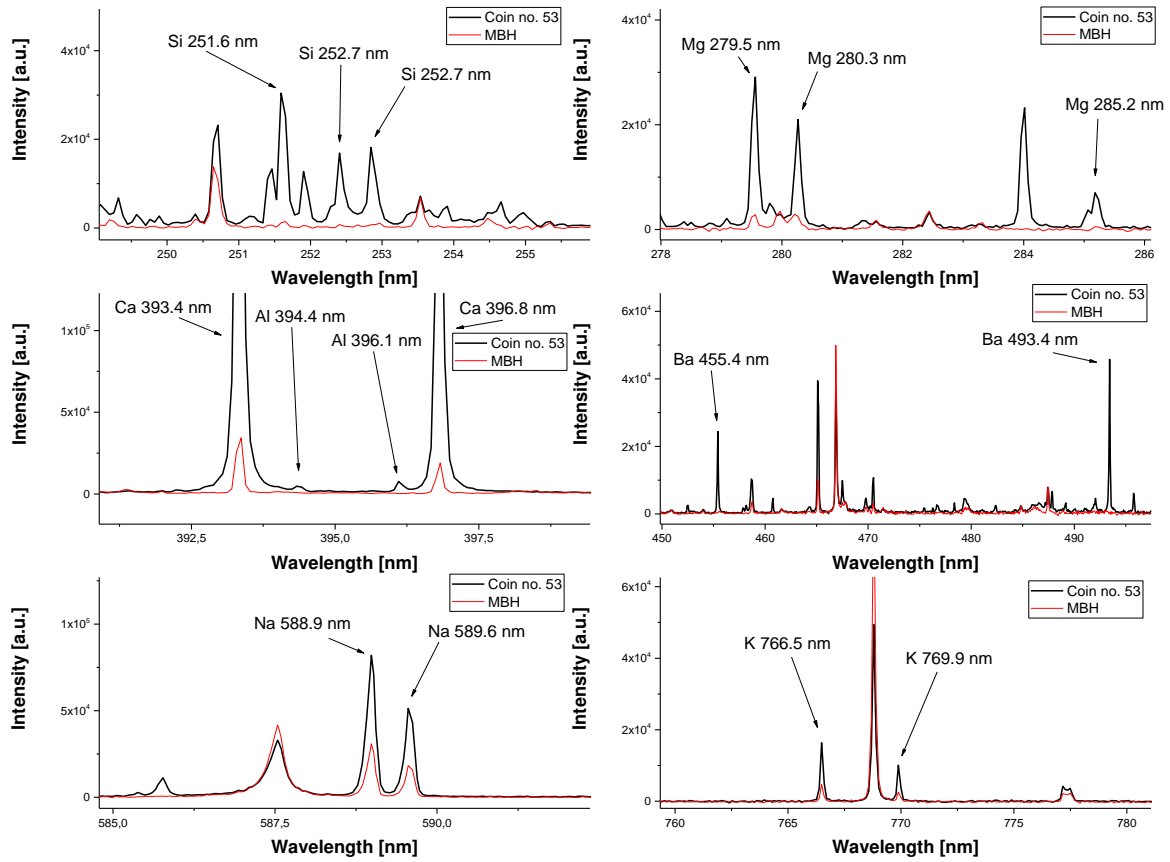


Figure 4.5: LIBS Spectra of the outer corrosion layer of a denarius (No. 53). The sections of interest for evaluated emission lines are magnified.

4.2.3 Crater Depth Determination – Profilometer

In Figure 4.6 and Figure 4.7 the crater effects on the MBH reference material can be seen. With an increase of the crater depth, the diameter of the craters decreases. Around the edges of the craters rises a ring with increased height due to redeposition of ablated material and to heat effects as melting. The more laser pulses are fired on the same spot, the more visible are the effects. For a better illustration of the crater profiles, the z-axis in Figure 4.7 is stretched by a factor $4 \cdot 10^3$.

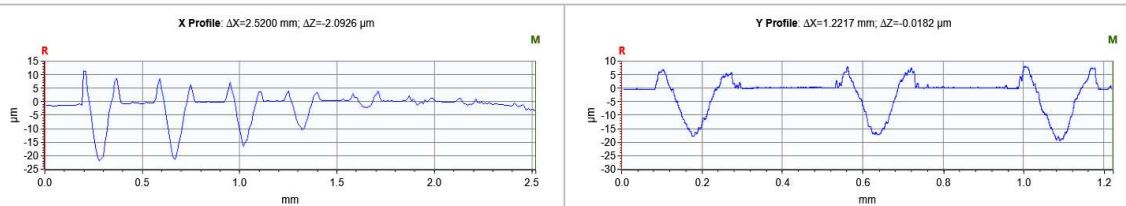
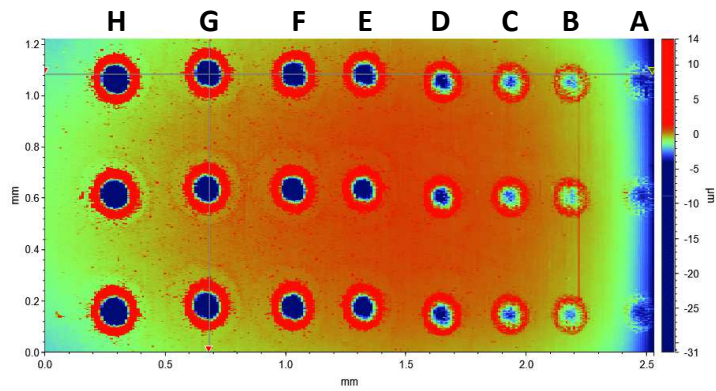


Figure 4.6: Above: 2D-plot of craters on MBH. Below: line profile over craters of different number of laser pulses (left) and same number of laser pulses (right).

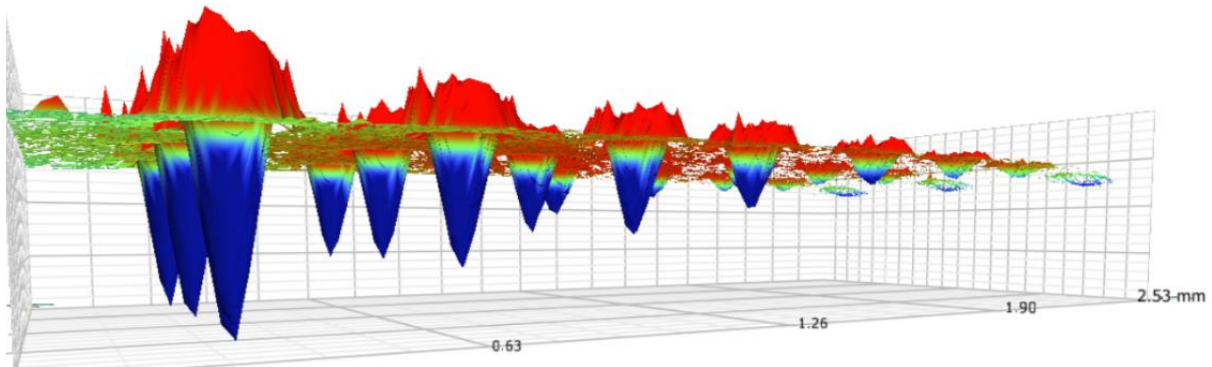


Figure 4.7: 3D-plot of craters on MBH.

The results of the depth measurements are shown in Table 4.2. With the used laser parameters (Table 4.1), the resulting average ablation depth equals $0.72 \pm 0.17 \mu\text{m}$ per laser pulse. The crater that resulted of a single laser pulse stands out of the trend, because with the first shot the laser is not yet in equilibrium.

Table 4.2: Average crater-depth and standard deviation (3 replicates):

Symbol	Number of shots	Average depth \pm standard deviation	Height increase on edges
A	1	$0.37 \pm 0.12 \mu\text{m}$	$0.2 \mu\text{m}$
B	2	$1.17 \pm 0.15 \mu\text{m}$	$0.8 \mu\text{m}$
C	3	$2.33 \pm 0.15 \mu\text{m}$	$2.0 \mu\text{m}$
D	5	$4.33 \pm 0.29 \mu\text{m}$	$3.0 \mu\text{m}$
E	10	$8.07 \pm 0.12 \mu\text{m}$	$3.2 \mu\text{m}$
F	15	$12.40 \pm 0.79 \mu\text{m}$	$5.6 \mu\text{m}$
G	20	$15.97 \pm 0.38 \mu\text{m}$	$5.9 \mu\text{m}$
H	30	$22.67 \pm 0.29 \mu\text{m}$	$7.6 \mu\text{m}$

4.2.4 Data Evaluation Strategy

After the measurement of all reference materials and standards, the spectra were thoroughly looked through to identify interference-free emission lines with sufficient intensity for each investigated element. For further evaluation and comparison of the samples, the selected descriptors emission lines were integrated using a linear background subtraction.

For the evaluation of the point measurements (4.2.5.1), this was done manually in EXCEL with ten accumulated spectra. The recorded spectra for the images (4.2.5.4) were evaluated with ImageLab® – software. Spectral descriptors for each emission line of interest were adjusted and set analogue to the point measurement evaluation using an integration procedure with a linear background subtraction. Based on the defined spectral descriptors, the images were created in the chemical map editor of ImageLab.

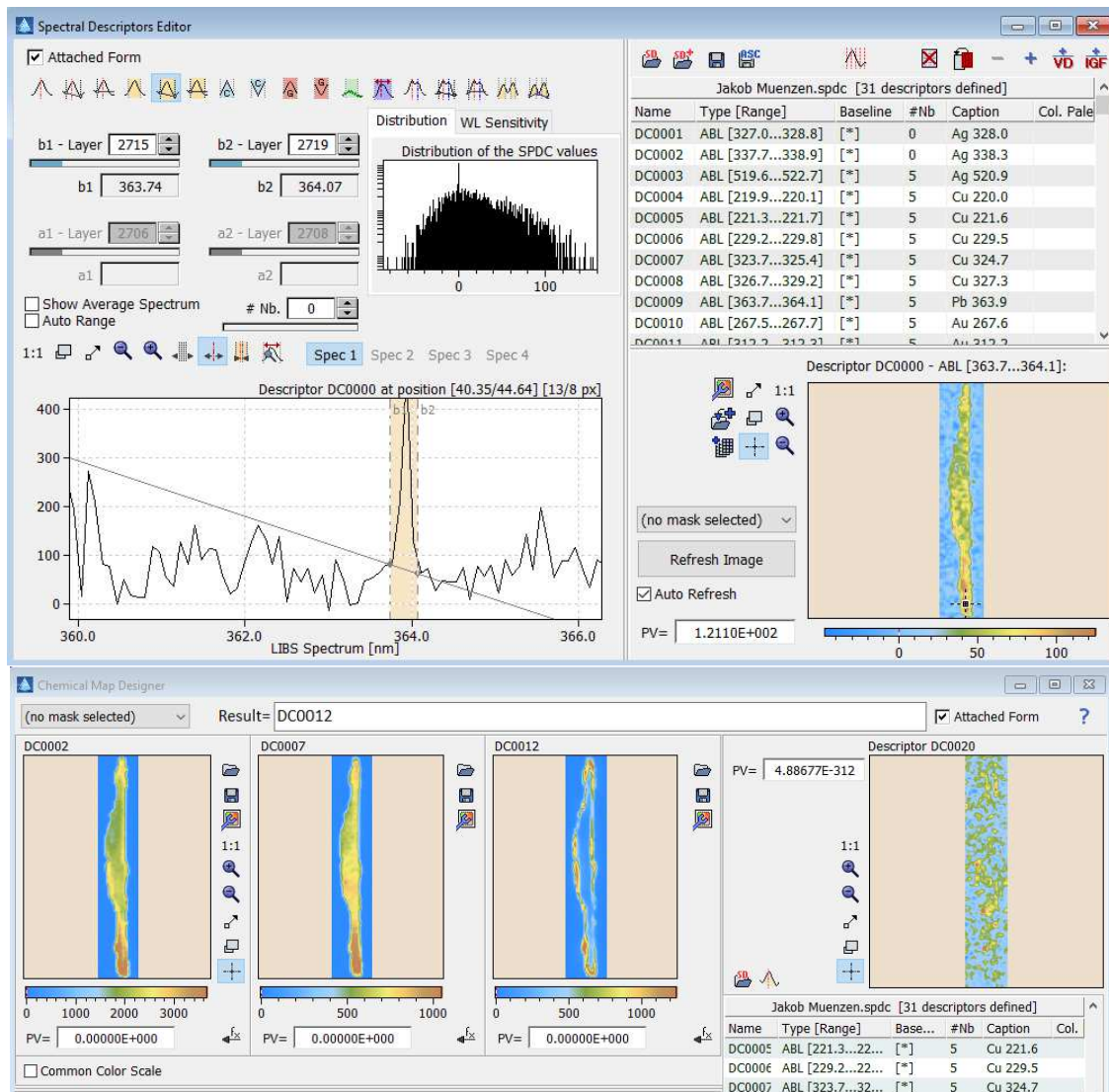


Figure 4.8: User-interface for the definition of a spectral descriptor (top) and the chemical map editor (bottom) in ImageLab®.

4.2.5 Sample Measurements

4.2.5.1 Spot Measurements – Comparison of the Core Alloy

As discussed in chapter 4.1, the microscopic images of the cross-sections show that the coins are very different in their appearance. Some are relatively homogeneous with almost no corrosion layer on the outside. Others have one or even two clearly distinguishable layers surrounding the core of the coin. Furthermore, some coins include spots that could be solid inclusions of some sort, that were introduced into the coin in the manufacturing process, or segregations of elements, that are soluble in the melt but when the melt crystallises, segregate and build separate phases. Therefore, performing LIBS measurements on random spots has little use for comparison of the coins and for allowing statements about individual coins.

Based on the microscopic images, spots were selected for point-measurements in the core, if present in the inner and outer corrosion layer, as well as on some visible inhomogeneities. Figure 4.9 shows a set of four coins and the selected measurement spots in the core, to compare the content of silver, copper, gold and lead in the original alloy. The results of the measurements are shown in Figure 4.10.



Figure 4.9: Microscopic images of the coins (no. 1, 2, 20, 39) used for comparison of the core alloy (Figure 4.10). The measured spots are marked by blue circles.

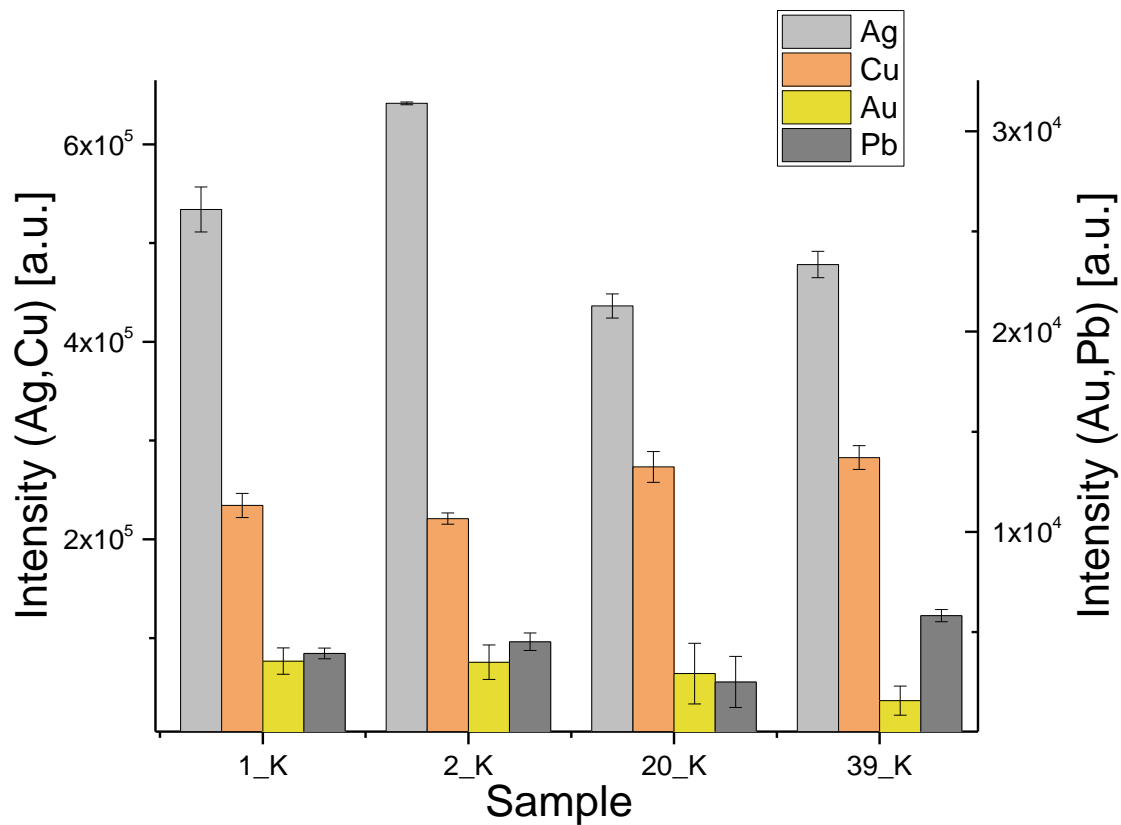


Figure 4.10: Comparison of the alloy of the coin core. Evaluated emission lines (Ag, Cu, Au, Pb) of the coins no. 1, 2, 20 and 39 (Figure 4.9). The error bars represent two times the standard deviation (3 replicates). The abbreviation “K” stands for core (dt. *Kern*).

In this work, no calibration and quantification were performed. The measured relative LIBS-intensities of silver, copper, gold and lead in the cores of the coins (Figure 4.10) show, with some limitations, a well according trend to the quantitative results of the XRF-measurements that were done in previous work (Table 4.3).

The coins no. 1 and 2 were manufactured during the ruling time of Traian’s predecessor Nerva and show a silver content of 87.0 and 93.2 %. This correlates with a high LIBS signal for Ag. The coin no. 20 (79.0 % Ag) is of Traian’s fourth consulate and coin no. 39 (80.3 % Ag) of COS V. Both were manufactured after the reported decrease of finesse from COS III on, due to financing the preparations for the Dacian wars, and show significantly lower intensities for silver.

Table 4.3: Results of μ -XRF and μ -SRXRF in previous work: [3]

Coin no.	μ -XRF				μ -SRXRF			
	Content of Elements [%]							
	Ag	Cu	Au	Pb	Ag	Cu	Au	Pb
1	87.0	12.7	0.13	0.22	88.22	11.05	0.20	0.52
2	93.2	6.5	0.13	0.21	93.67	5.67	0.22	0.43
20	79.0	20.7	0.16	0.24	80.95	18.72	0.23	0.53
39	80.3	19.3	0.05	0.39	83.62	15.34	0.04	0.99

The copper content in the two coins of Nerva's rule (no. 1 and 2) is approximately factor 2 (no. 1) and a factor 4 (no. 2) lower than in the shown coins of Traian. The LIBS results show the same trend, but the differences in the measured intensity is much below a factor 2 or even 4. The trend of gold intensities is in good accordance with the XRF results, showing the coins no. 1, 2 and 20 with a similar Au-content and coin no. 39 with a significantly lower Au-content. For lead, the trend does not match with the results of the previous work. The only according result for lead is, that coin no. 39 shows significantly the highest Pb-content. But it should be mentioned that also in the previous work, while the results for Ag and Cu match well between the μ -XRF and μ -SRXRF measurements, the results for gold and lead do not concur. An adequate comparison presupposes a homogeneous distribution, what is not yet verified at this point and will be discussed in chapter 4.2.5.4.

There are several possible errors in the measurement of a silver-copper-alloy using LIBS, μ -XRF and μ -SRXRF, that can explain the divergent results.

First, silver and copper are not miscible in the solid phase. The eutectic composition with 71.9 % Ag and 28.1 % Cu has a melting point of 779 °C (phase diagram attached in Appendix (8.3, Figure 8.1)). When the melt with a different composition cools down, the excess component crystallises first in nearly spherical grains (α -silver or β -copper), until the remaining melt has the eutectic composition. Then the eutectic melt crystallises fast, leading to a lamellar eutectic metallographic structure. Depending on the original composition of the melt and the cooling speed, the metallographic structure is different, showing smaller or bigger Ag or Cu grains up to over 100 μ m in diameter. [33], [34] Examples for the metallographic structure of a binary Ag/Cu mixture is shown in the Appendix (8.3, Figure 8.2).

In μ -XRF, the x-ray beam is focused on a small area of usually under 100 μ m down to 10 μ m [35]. The penetration depth in metals is usually lower than 20 μ m [36]. In this work, with LIBS a spot of 80 μ m in diameter and a penetration depth of approximately 10 μ m were used.

Because of the small information volume of the used methods and the nature of the metallographic structure of Ag-Cu alloys, the result depends strongly on the measurement spots, whether a grain or the eutectic laminar structure are measured or not. Additionally, in all applied method the signal is strongly dependent on the matrix. In XRF the nuclear charge play an important role for the interaction cross-section of the incident beam with the samples. Further, self-absorption and secondary fluorescence lead to an error in the result of the measurement. With LIBS, the interaction behaviour of the laser with the sample surface depends on the material and the morphology and the excitation characteristics of the plasma depend on the elements present.

4.2.5.2 Spot Measurements – Comparison of the Core with outer Layers

Figure 4.11 shows the microscopic images of three coins on which the core and two layers can be distinguished in their appearance. The inner layer stands out with a stronger bluish shade and the outer layer appears greyer and less bluish. In each coin, measurement spots were set in the core (blue circles) and in the inner (orange circles) and outer layer (green circles).

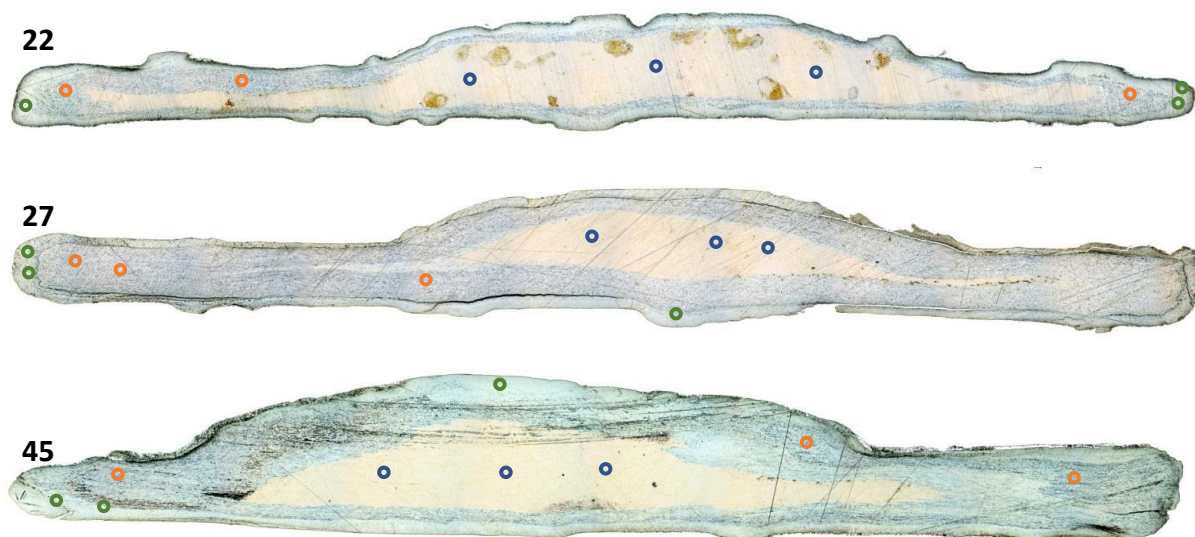


Figure 4.11: Microscopic images of the coins (no. 22, 27, 45) used for comparison of the silver and copper content of the core with the inner and outer corrosion layer (Figure 4.12). The measured spots are marked by circles (blue...core, orange...inner layer, green...outer corrosion layer).

The results are shown in Figure 4.12. It can be seen, that in all three coins the silver content increases from the core to the outside layers. In coin no. 22, the Ag intensity is even about 50 % higher in the outermost layer than in the core. This observation is well in accord to the reported silver enriched surface due to the acid leaching and partial oxidation in the manufacturing [3], [11].

Another explanation for silver surface enrichment in silver-copper-alloys is given by the phase diagram (Appendix 8.3, Figure 8.1). In a down cooling Ag-Cu melt that contains more than 71.1 % Ag (eutectic composition), which is the case for all analysed coins, at first a α -silver phase crystallises until the melt remains with a eutectic composition. A melt always cools from the outside to the inside and consequently the surface is enriched with α -silver grains. [34]

The copper content shows a slight decrease from the core to the outer layers, but regarding the error bars the decrease is not significant.

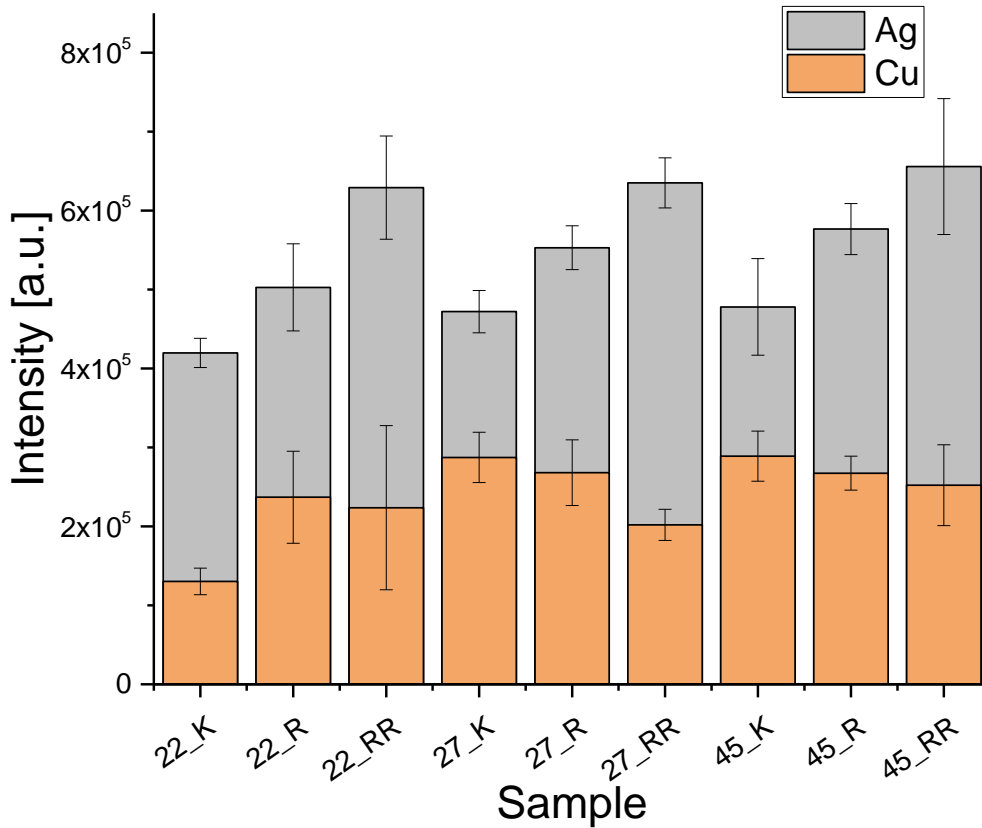


Figure 4.12: Comparison of the silver and copper content of the core, the inner and the outer corrosion layer of the coins no. 22, 27 and 45 (Figure 4.11). The error bars represent two times the standard deviation (3 replicates). K...core (dt. Kern), R...inner layer (dt. Rand), RR...outer corrosion layer.

The measured spots in the corrosion layer of coin no. 53 showed similar LIBS spectra with all the mentioned elements present. The evaluated results of five measurement spots were averaged including error bars, calculated as two times the standard deviation (Figure 4.13).

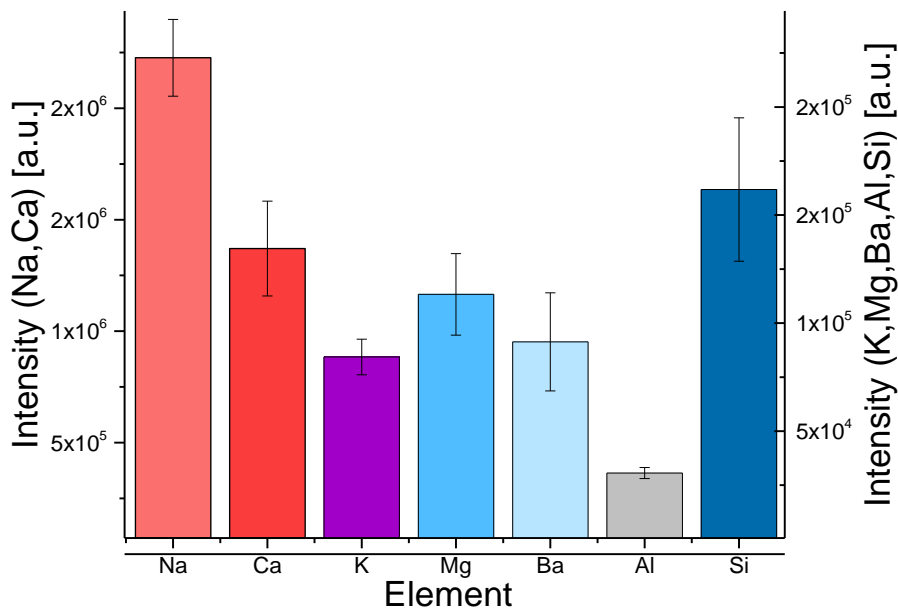


Figure 4.13: Evaluated emission lines (Na, Ca, K, Mg, Ba, Al, Si) of the outer corrosion layer of coin no. 53 (Figure 4.3, 5 measurements accumulated). The error bars represent two times the standard deviation.

In the outermost layers of the coins, several more elements were identified (Na, K, Ca, Mg, Ba, Al and Si). These are typical elements found in rock ground material and are present due to corrosion caused by environmental effects over the last two millennia.

4.2.5.3 Spot Measurements – Comparison of inhomogeneous Inclusions

As already mentioned, inhomogeneities inside the coins can be seen in several microscopic images. Therefore, measurements were performed on some spots of interest to obtain an insight of the elemental composition of such inhomogeneities. Figure 4.14 shows two examples of coins with markings on the measured spots. The results are shown in Figure 4.15. On each spot a single measurement with 10 accumulated pulses was performed, therefore, no error bars are displayed. Signal values that were below ten times of the standard deviation σ of the noise, have been set to zero. Investigated were the same elements that could be identified in the corrosion layers in the previous section 4.2.5.2: Na, K, Ca, Mg, Ba, Al and Si.

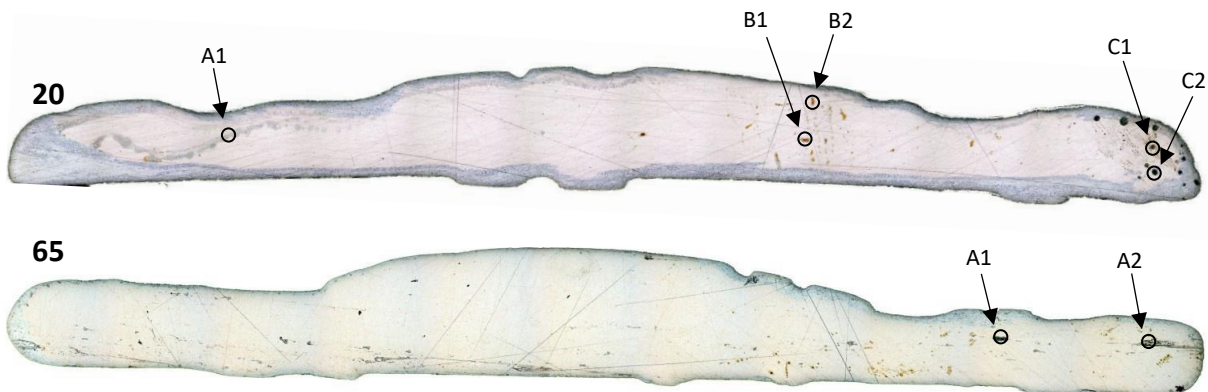


Figure 4.14: Coins no. 20 and 65 with markings on measured spots. The results are shown in Figure 4.15.

Generally, it can be observed, that some of the investigated spots contain elements that others do not, and some spots contain nearly, or even all the evaluated elements. The spot “A1” of coin no. 20 is set on a slightly greyish and blueish gleam, that proceeds diffuse inside the coins core. It contains calcium, barium, aluminium and silicon. The intensities are rather small. Therefore, it is possible that a small amount was dissolved in the melt and crystallised as a separate phase when the melt was cooled. It is also possible, that the discussed elements were originally embedded in the crystal lattice of the silver- or copper-phase and formed separate solid phases over the last two thousand years due to diffusion. Calcium and barium form double charged cations (Ca^{2+} , Ba^{2+}). Aluminium forms either a triple positively charged Al^{3+} cation or a complex anion as $[\text{Al}(\text{OH})_4]^-$ (tetrahydroxy aluminate) and silicon forms either a four times charged Si^{4+} or several species of complex anions with oxygen [37]. The most prominent is a $[\text{SiO}_4]^{4-}$ monomer with a tetrahedral structure. In amorphous silicate glasses and in plenty of

crystalline silicate minerals, they form condensed frameworks of corner-shared $[\text{SiO}_4]^{4-}$ - tetrahedrals as anions with metal cations incalated in the gaps [38].

Though the regions of “B1” and “B2” appear like very similar brown spots on the microscopic image of coin no. 20, the evaluated element intensities are different. “B1” contains magnesium, barium and silicon, suggesting a silicate compound, whereas “B2” contains sodium, potassium and barium. Na, K and Ba all form cations only. Therefore, they probably are present as oxides, sulfides, hydroxides carbonates, sulfates, nitrates or halogenides. [37]

Oxygen could also be seen in the LIBS spectra but was not taken into account in the evaluation of this section.

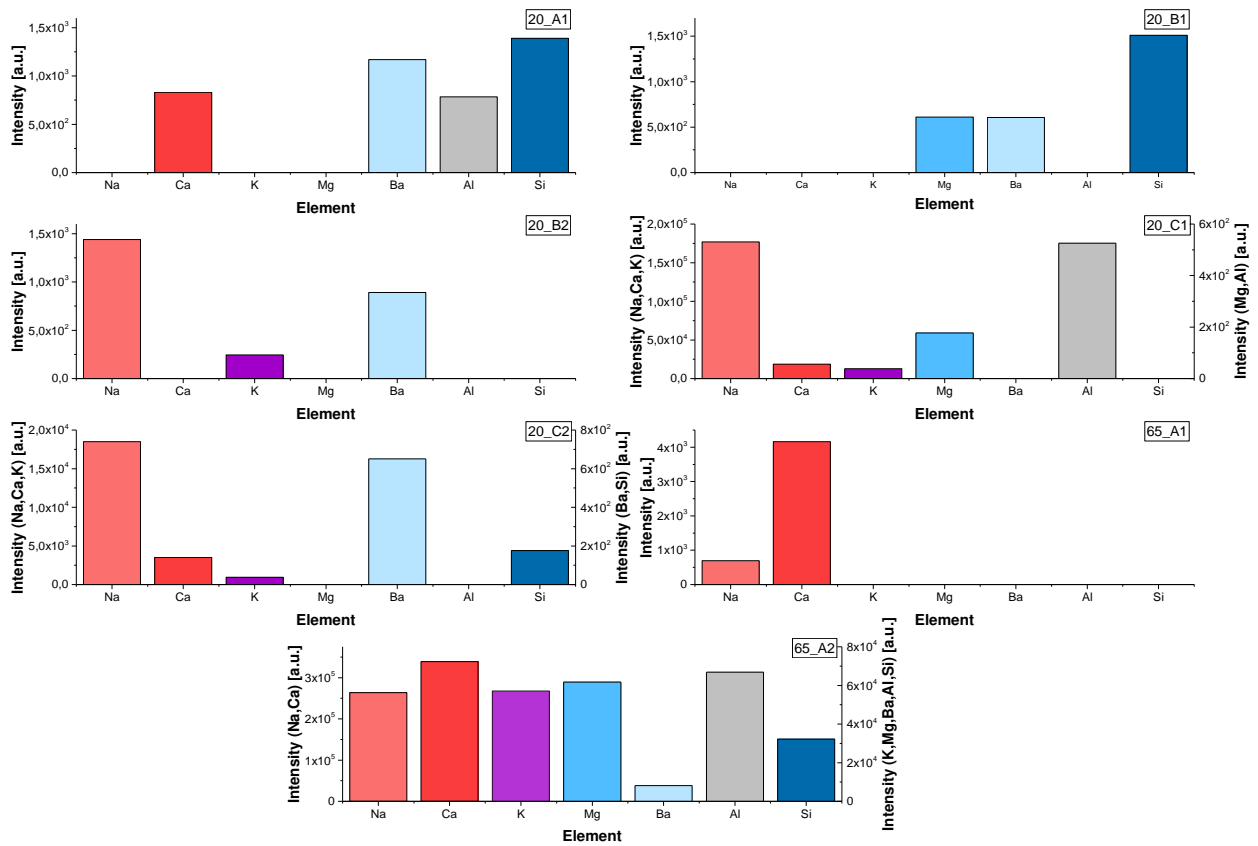


Figure 4.15: Elements found in visible inhomogeneities in the coins no. 20 and 39. The coins and the measured spots are shown in Figure 4.14. The signal values that were below 10σ of the noise have been set to zero.

The spots “C1” and “C2” of coin no. 20 appear similar as black spots, though the measurement results show different compositions. They both show high signals intensities for sodium and low calcium and potassium signals. But while in “C1” significant amounts of magnesium and aluminium are present, “C2” shows barium and silicon instead. Concluded it can be said, that coin no. 20 contains several types of different contaminations. Though some appear very similar in the microscopic image, the evaluated LIBS measurements (Figure 4.15) show that their elemental composition is different.

The black appearing spot “A1” in coin no. 65 (Figure 4.14) shows only the presence of sodium and calcium, again suggesting oxides, carbonates, etc. The spot “A2” is set on a shiny bluish line, that reaches from the edge of the coin into its core. The bluish line may have originated from a micro crack, allowing the elements from the environment to get into the coin along that path. The measurement of this spot shows all investigated elements present.

There are three possible causes for foreign phases in the coins. If the contaminations were dissolved in the melt, they might crystallise as separate phase caused by segregation during the down cooling. If the concentration of the contamination is small enough, they might also be built-in the crystal structure of the parent-phase and then segregated slowly in the last two-thousand years by lattice-diffusion. The third reason could be contamination by small particles suspended in the melt, that were brought in and were never liquified.

4.2.5.4 *Imaging*

The elemental images were created out of single shot spectra in each pixel and an interpolation between the pixels afterwards to obtain a better image resolution. Compared to the spot measurements with 10 accumulated spectra, the signal-to-noise-ratio and consequently the sensitivity is worse. However, the obtained sensitivity is easily sufficient to map the elemental distribution of major and minor components, as well as the other elements, that are either concentrated in the corrosion layer or in small spots or bigger sections inside the coins. A selection of coins that show characteristic features will be discussed in this section.

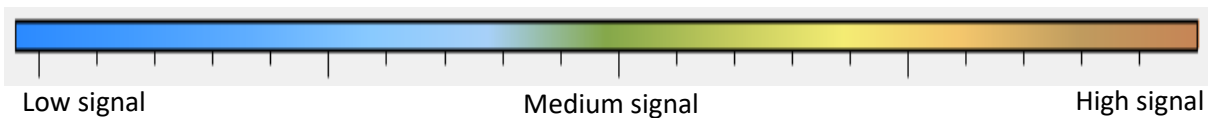


Figure 4.16: Colour scale for the relative element concentrations in the LIBS images [a.u.].

The relative element concentrations are displayed in the images using a colour scale (Figure 4.16). The line above the image stacks defines the element that is mapped below. For the microscopic image the shortcut “M” was used.

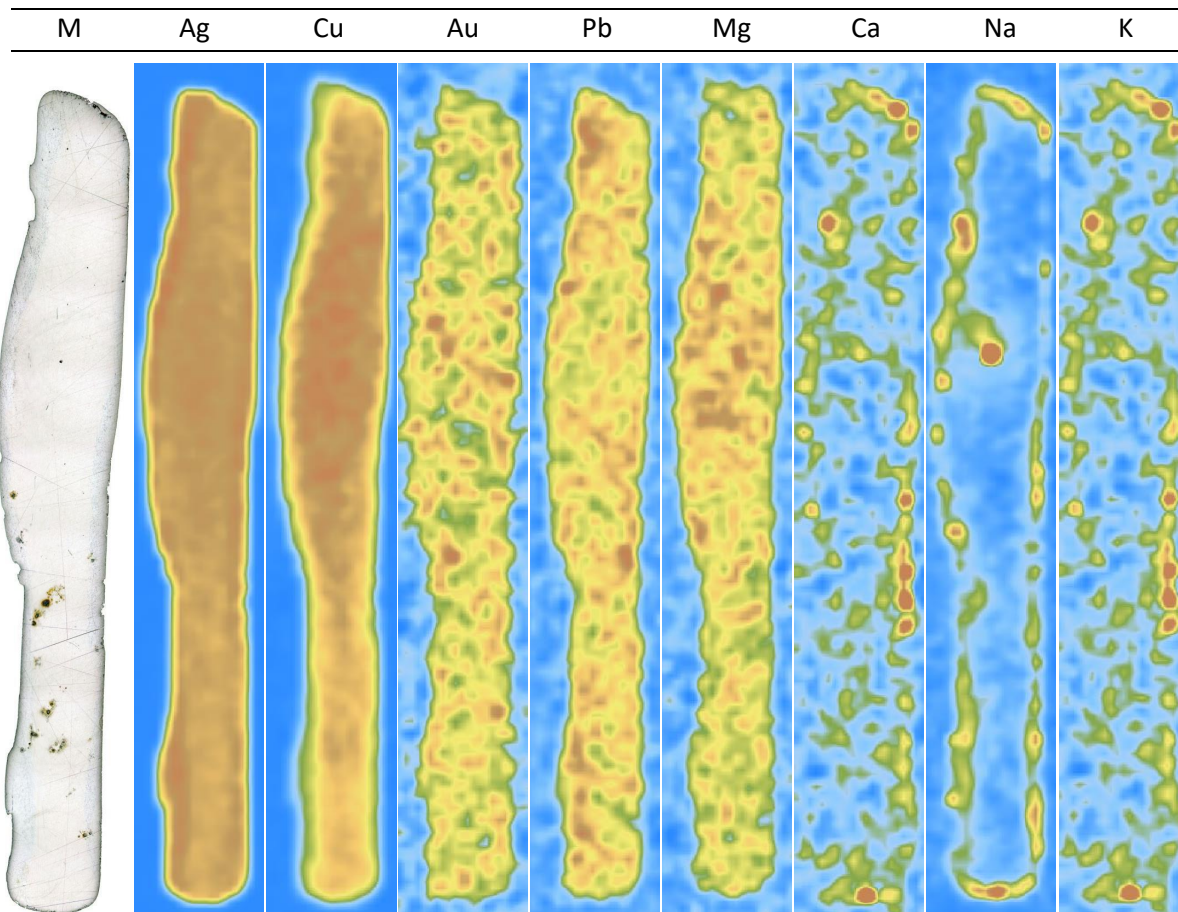


Figure 4.17: LIBS – Images: Elemental maps of coin no. 1 (Nerva, AD 97).

Figure 4.17 shows the microscopic image and the elemental maps created with LIBS - Imaging of coin no. 1 (Nerva, AD 97). The silver and copper distribution are relatively homogeneous, yet it is recognizable that silver is slightly enriched in the surface (the edges of the cross-section) whereas the copper content decreases there. The copper concentration in the lower part of the image is slightly lower. The whole coin contains gold, lead and magnesium in a sufficient concentration to be detected with single shot spectra. For all three of these elements, there are little sections with relatively high concentrations and others with lower concentrations. For the elements mentioned so far, no correlation is visible. The outermost layer of the coin shows some parts containing calcium, sodium and potassium. Ca and K are well correlated, whereas Na is only present in some of the parts that also show Ca and K. In the core of the coin, one spot with a high Na concentration can be seen, that is recognizable by a tiny black spot in the microscopic image.

Summed up, compared to the following coins, the observed coin is relatively homogeneous regarding the main components and has comparably high contents of gold, lead and magnesium. It is only slightly corroded, what may be a result of the circumstances under which it had passed its existence until now.

Further, with a relatively high silver and gold content, it is more noble and has a better resistance against corrosion compared to coins with less Ag and Au.

The microscopic image and the elemental maps of coin no. 39 (Traian COS V, approx. AD 107 – 108) are shown in Figure 4.18. Silver and copper are distributed less homogeneously than in the previously investigated coin of Nerva's rule. On the left side a slight silver enrichment is observable, whereas on the right side there is a layer with decreased silver content, that also shows the presence of aluminium and zinc. Zinc was not found in the outermost layer of any other of the over sixty analysed coins. Therefore, it is assumable that the zinc-aluminium alloy does not come from the environment but was pressed on the coin at a time after the coins original manufacturing, maybe to renew it. Compared to coin no. 1, where magnesium was present in the whole cross-section, in coin no. 39 it is nearly only found in the corrosion layer. The higher concentrated sections of magnesium also correlate with sodium and potassium, indicating that its presence in the coin is caused mainly through the environment by corrosion. It can further be observed that the right side of the coin, which contains the Al-Zn layer, is stronger corroded than the left side. This occurs due to the fact, that Al and Zn are less noble and therefore less corrosion resistant than Ag.

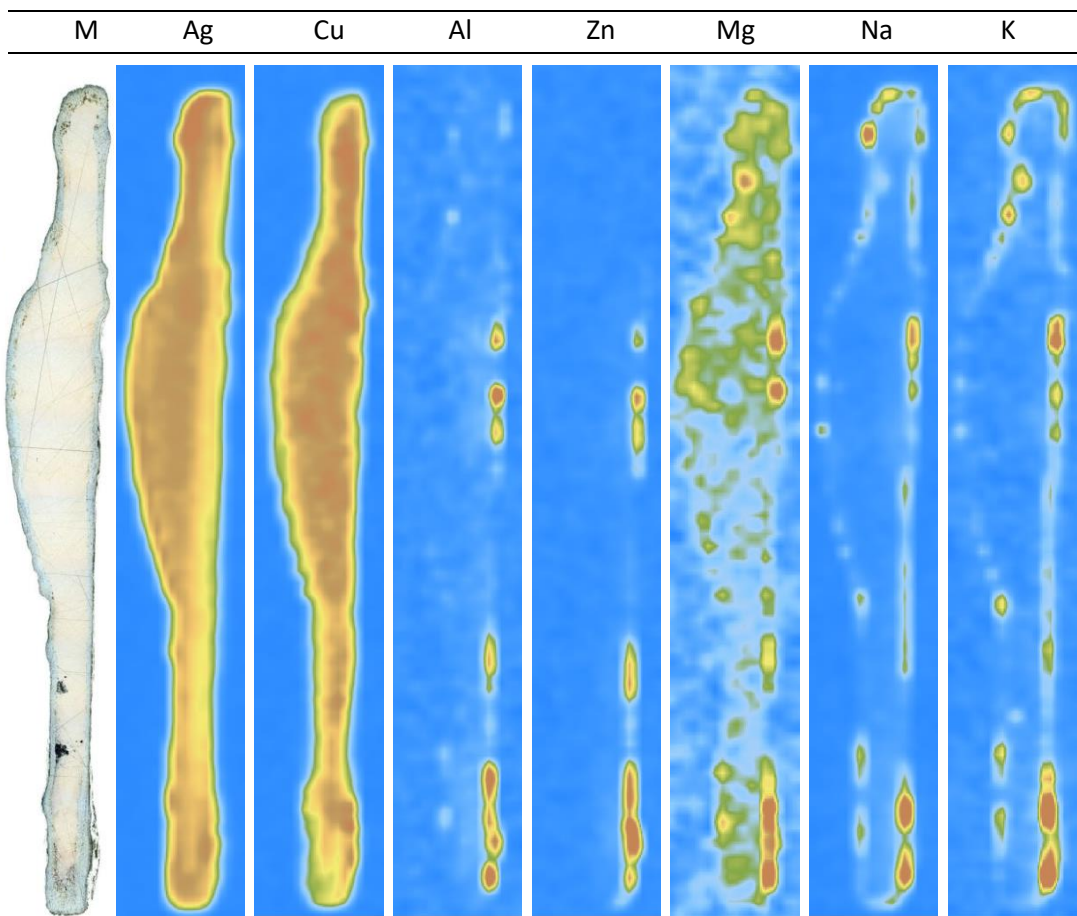


Figure 4.18: LIBS – Images: Elemental maps of coin no. 39 (Traian COS V, approx. AD 107 – 108).

Compared to the previously described samples, the elemental distribution in coin no. 57 (Figure 4.19) is rather inhomogeneous. The silver concentration is much higher in the lower part, whereas copper shows complementary behaviour with higher concentrations in the upper part of the cross-section. The lead distribution is very inhomogeneous and correlates with silver but shows some higher concentrated spots in the upper part of the image. Calcium is present in accumulated spots in the upper part of the image. Calcium is present in accumulated spots in the outermost layer, but no continuing layer can be observed.

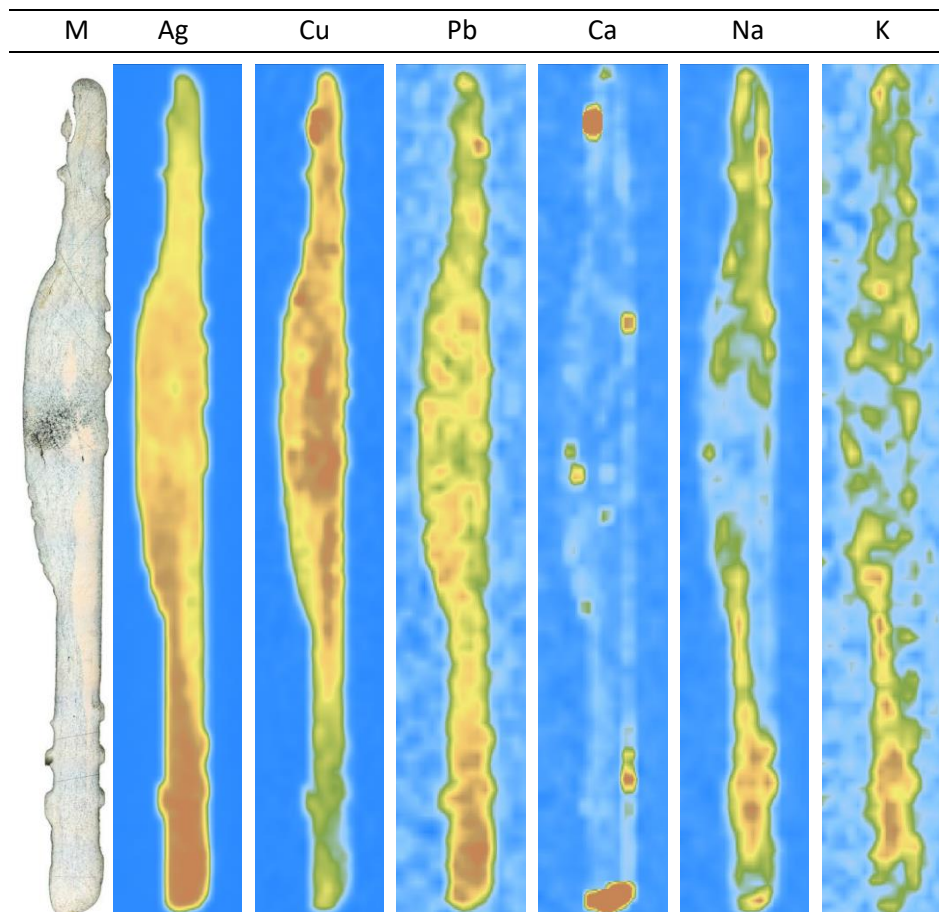


Figure 4.19: LIBS – Images: Elemental maps of coin no. 57 (Traian COS VI, AD 112).

Of particular significance are the sodium and potassium distributions, both correlating with each other and showing presence in a large part of the coin. In contrast to Ca, that is present in some spots of the corrosion caused layer, for Na and K no particular enrichment in that layer can be observed. This indicates, that those alkali metals remained in the melt out of which the coins were originally casted, because of poor refining quality. It is possible, that the original refining of the raw material was not done with enough care. But another possible reason could be, that the coin was produced out of recycled old coin material, possibly with decreasing its finesse by adding additional copper to the melt.

It can be assumed, that the recycling or recasting process was not done with the same metallurgical quality as is in the raw material production. As old coins that already had plenty of corrosion caused contaminations of the environment on and in their surface were used as raw materials, those elements are mixed in the melt and are a part of the alloy in the newly casted coins, if not detached in an additional process step.

Coin no. 61 (Traian COS VI, AD 114 - 116, Figure 4.20) shows similar features as described for coin no. 57. The silver concentration is relatively higher in the upper part of the coin, whereas copper shows the opposite trend. Further it can be seen, that silver is enriched in some parts of the surface. As already mentioned a possible reason for the surface enrichment of silver is the inhomogeneous cool-down through the coin. This could be responsible for the lower side of the coin containing more silver because it was cooled faster. Then the other side would contain the eutectic composition. Lead again shows a correlating trend to the silver concentration.

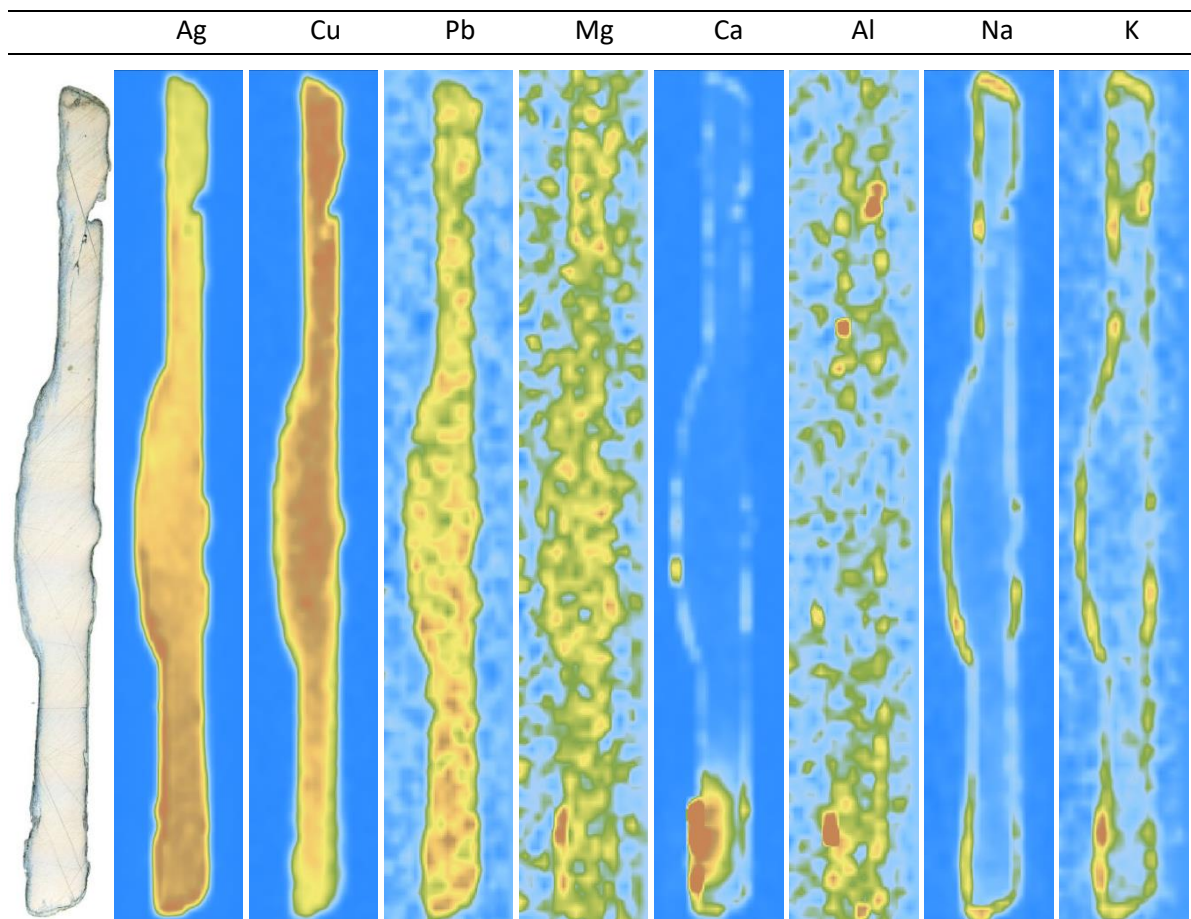


Figure 4.20: LIBS – Images: Elemental maps of coin no. 61 (Traian COS VI, approx. AD 114 – 116).

Magnesium is present in the alloy of this coin like in the one described of Nerva's ruling time. Here it is additionally enriched in a spot of the corrosion layer on the left side in the lower part of the image. In this part calcium, aluminium, sodium and potassium are present as well. The relatively high concentrated spots of Al correlate with Ca and K. While K and Na form, despite these spots, a nearly continuous layer around the coin, Al only is present in those spots and in low concentrations inside the coins core. But it is not at all present in the surrounding layer. Furthermore, the spot on the lower left side that contains a high Mg, Al, K, Na and Ca concentration is much bigger for Ca.

Summarised, the following observations can be made. Some coins show a relatively homogeneous silver and copper distribution, in others major differences are observed. Silver is generally correlated with lead and slightly enriched in the surface layer. Magnesium is sometimes a part of the alloy, even if other elements that are generally present in the corrosion layer are found only on the surface of the coin. There are stronger as well as weaker corroded coins, sometimes showing the elements Na, K, Mg, Ca, Al, Si in high concentrated spot and other times in a continuous layer. Further those elements can sometimes be found evenly distributed in some parts of the coins inner, indicating a possible recycling with worse refining quality. But they are also observed in small high concentrated spots in the coins inner, suggesting different phases that may be the result of small particle contaminations in the melt when the coins were casted.

4.3 LA-ICP-MS

4.3.1 Optimisation

Measuring the MBH reference material with laser ablation, the dwell times and the laser repetition rate were varied and optimized for as constant a signal as possible. The least standard deviation of a mean, calculated out of 50 datapoints, was received with a dwell time of 7 ms for each isotope and a laser repetition rate of 20 Hz.

4.3.2 Data Evaluation Strategy

To obtain adequate isotope ratios using quadrupole ICP-MS, several data processing and corrections need to be accounted for, including background subtraction, correction for mass bias and for instrumental drifts. Figure 4.21 shows a schematic illustration of the performed steps, which are explained in more detail in the following.

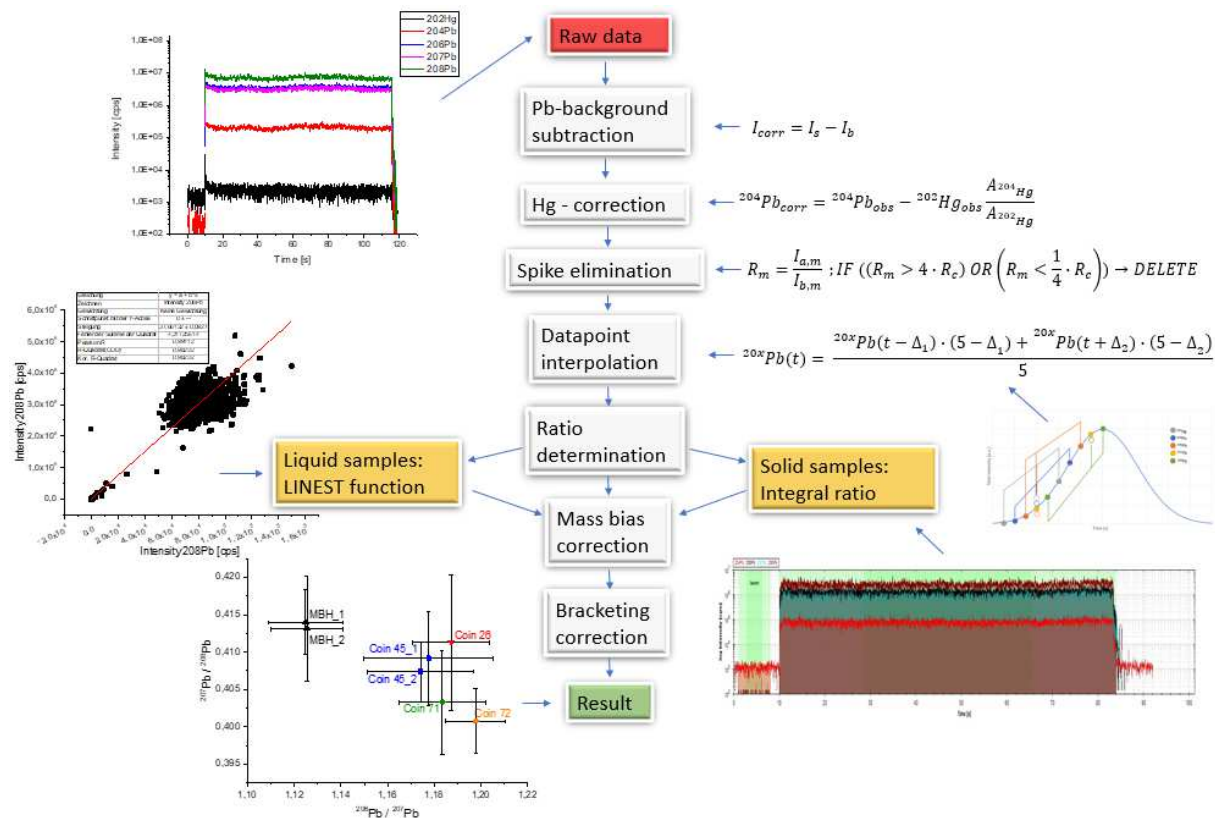


Figure 4.21: Scheme for Data processing and evaluation.

4.3.2.1 Pb – Background Subtraction

Because a Pb background signal was present in the gas blank and the liquid blanks, the signals of the measured samples were corrected by subtracting the mean value of the blank signal for each isotope according to Equation 1.

$$I_{corr} = I_s - I_b$$

Equation 1: Background subtraction.

I...Intensity
 s...sample signal
 b...blank signal

4.3.2.2 Hg – Background Correction

A mercury background signal was present in the gas blank as well as the reagents and in the digested standards for liquid measurements. The mercury isotope with a mass of 204 amu interferes with ²⁰⁴Pb and therefore needs to be corrected. This was done by also measuring ²⁰²Hg and subtracting the amount, that is caused by mercury and measured at the mass 204 (Equation 2), according to the natural abundances (Table 4.4).

Table 4.4: Natural Abundances of relevant mercury isotopes: [39]

Isotope	Natural abundance
²⁰² Hg	29.74 %
²⁰⁴ Hg	6.82 %

$${}^{204}Pb_{corr} = {}^{204}Pb_{obs} - {}^{202}Hg_{obs} \frac{A_{204Hg}}{A_{202Hg}}$$

Equation 2: Hg correction of ²⁰⁴Pb.

corr...corrected
 obs...observerd
 A...natural abundance

4.3.2.3 Interpolation

To determine a correct ratio of ideal constant signals, the time does not need to be considered. When the ratio of transient signals is looked-for, it can only be determined if both signals are measured at the same time (Equation 3).

$$\frac{{}^{20x}Pb}{{}^{20y}Pb}(t) = \frac{{}^{20x}Pb(t)}{{}^{20y}Pb(t)}$$

Equation 3: Correct ratio determination. x,y=4; x,y=6; x,y=7; x,y=8; x≠y.

The sequential scanning of masses by quadrupole analyser causes an error. To minimise the impact of that error, very long measurement times that produce large numbers of data points are required, to gain a good statistical mean and standard error. A way to improve the accuracy of shorter transient signals is to interpolate all measured isotopes in each sweep (measurement cycle) to a reference time and thereby imitate the signal that an interpolated isotope would have had if it would have been measured at the reference time. In this work ²⁰⁷Pb was defined as reference point. Figure 4.22 shows a scheme for the interpolation procedure and the calculation formulas are given in Equation 4 and Equation 5.

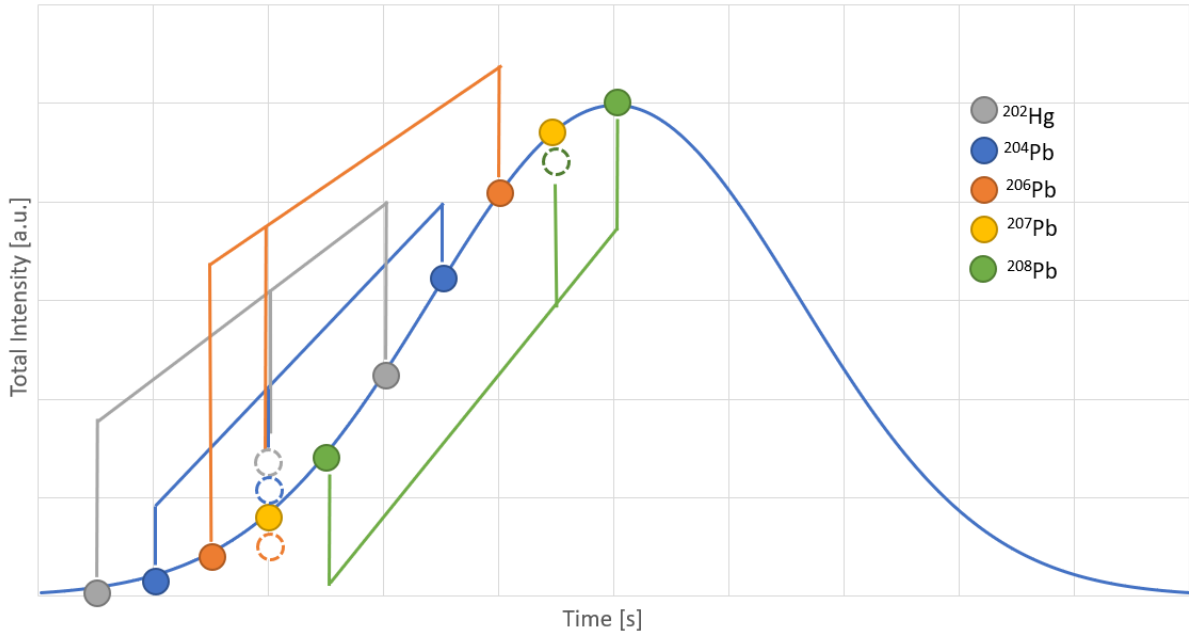


Figure 4.22: Scheme for interpolation of Pb-isotope-signals on an artificial transient signal.

$${}^{202}\text{Hg}(t) = \frac{{}^{202}\text{Hg}(t-3) \cdot 2 + {}^{202}\text{Hg}(t+2) \cdot 3}{5}$$

Equation 4: ${}^{202}\text{Hg}$ – Interpolation.

$${}^{20x}\text{Pb}(t) = \frac{{}^{20x}\text{Pb}(t-\Delta_1) \cdot (5-\Delta_1) + {}^{20x}\text{Pb}(t+\Delta_2) \cdot (5-\Delta_2)}{5}$$

Equation 5: ${}^{20x}\text{Pb}$ – Interpolation, $x=4$; $x=6$; $x=8$.

The parameters for the interpolation of the different lead isotopes are listed in Table 4.5.

Table 4.5: Δ - values for linear interpolation of lead isotope signals (Equation 5):

Isotope	Δ_1	Δ_2
${}^{204}\text{Pb}$	2	3
${}^{206}\text{Pb}$	1	4
${}^{208}\text{Pb}$	4	1

4.3.2.4 Spike Elimination

Signal spikes were eliminated by comparing the calculated ratios of each set of datapoints in a sweep with the certified values of the BAM reference material. If a ratio was four times bigger or four times smaller than the consensus value, the datapoint was defined as a spike and all datapoints of that sweep were removed from the data (Equation 6).

$$R_m = \frac{I_{a,m}}{I_{b,m}} ; IF ((R_m > 4 \cdot R_c) OR (R_m < \frac{1}{4} \cdot R_c)) \rightarrow DELETE$$

Equation 6: Condition for spike elimination.

$R_{m/c}$...measured/certified ratio
 $I_{a/b,m}$...intensity of measured signals a and b

4.3.2.5 Ratio Determination

The isotope ratios of the liquid sample measurements were evaluated with the LINEST function in EXCEL. Input values are x- and y-values of the measurement dataset. The function performs a linear regression and gives the slope, slope error and further parameters of the regression as output. The y – intercept was set to zero. By using one isotope signal as x-values and the other isotope signal as y-values, the slope of the regression corresponds to the isotope ratio.

The isotope ratios of the solid sample measurements with laser ablation were evaluated by integration of the isotope signals and subsequent division.

With integral evaluation, only one result is received out of a single measurement, therefore no error can be stated in a common way. To give a conservative estimation of the measurement uncertainty, the signals of each measurement were split in sections of 250 data points each. The standard deviation of the in this way calculated multiple ratios of one measurement, was used to represent the error bars in the ratio plots of LA-ICP-MS and Tandem – LIBS/LA-ICP-MS measurements.

4.3.2.6 Mass Bias Correction

A linear model was used for mass bias correction (Equation 7, [40]). According to literature this model is sufficiently accurate for quadrupole mass analysers due to their limited precision [19].

$$R_{corr} = R_{obs} \cdot (1 + k \cdot \Delta m)$$

Equation 7: Linear model for mass bias correction [40].
R_{corr/obs}...corrected/observed ratio
k...correction factor
Δm...mass difference of corresponding isotopes

The correction factor is determined by the measurement of a certified reference material with known isotope ratios. By using the determined correction factor, the observed ratios of the unknown samples are corrected for mass bias.

4.3.2.7 Bracketing Shift Correction

To correct for instrumental drifts during a measurement session, the measurements performed with laser ablation are bracketed by the measurement of reference materials with known isotopic composition. The measured sample values are corrected for mass bias and instrumental drift according to a linear interpolation between the two bracketing, bias corrected reference measurements.

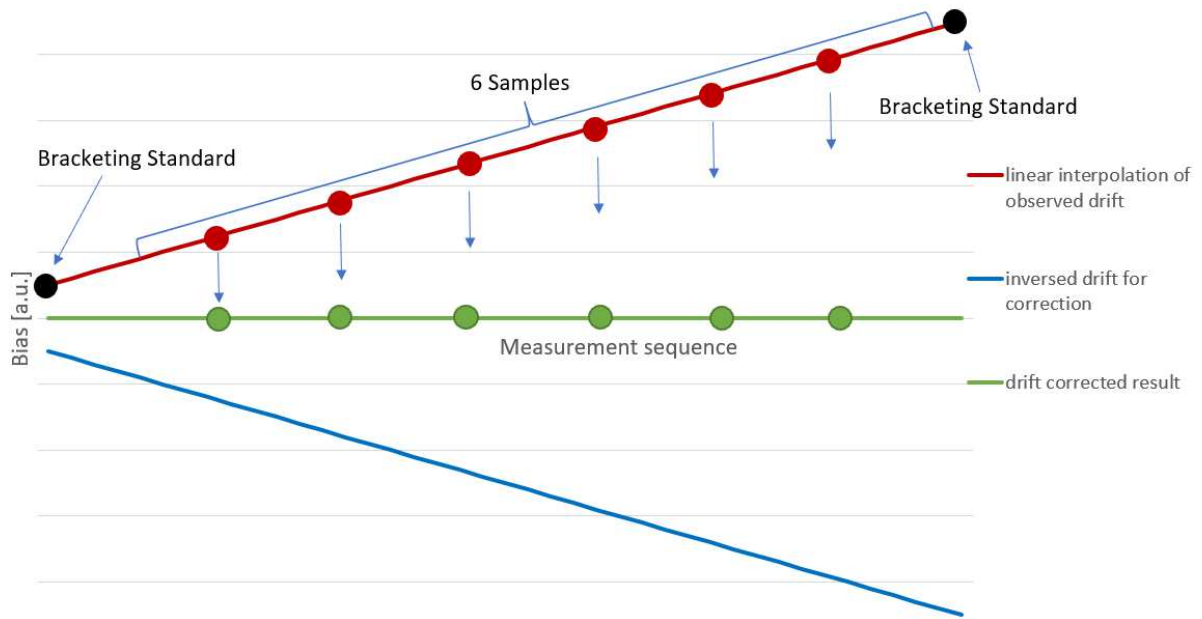


Figure 4.23: Scheme for bracketing correction of instrumental bias and drift.

4.3.3 Liquid Measurements of Reference Materials

The data of each dilution series was combined into a total dataset and the Pb-isotope ratios were calculated as the slope of a regression with one of the two corresponding isotope signals on the x-axis and the other on the y-axis. Due to a, for the purposes of ratio determination, insufficiently accurate cross-calibration of the two detectors of the instrument, data in which the intensity range lead to the use of both detectors cannot be evaluated correctly. Because the signal of ^{208}Pb (highest abundance) was too high and therefore detected by the analogue detector of the instrument, the data of the highest concentrated solution was not used for further data evaluation. The results of the BAM solutions, measured from two independent dilution series (referred to as BAM-1 and BAM-2), are shown in Table 4.6. The mean values were used for the calculation of the mass bias correction factors.

Table 4.6: Results, measured and calculated values of liquid BAM measurements:

Ratio	BAM-1	BAM-2	Mean value	Mean error ¹	Certified value	Offset ²	Δm^3	K^4
$^{206}\text{Pb}/^{204}\text{Pb}$	18.395	18.400	18.398	0.16 %	18.072	1.80 %	-2	0.00885
$^{207}\text{Pb}/^{204}\text{Pb}$	15.899	15.887	15.893	0.15 %	15.578	2.02 %	-3	0.00661
$^{208}\text{Pb}/^{204}\text{Pb}$	39.432	39.447	39.440	0.16 %	38.075	3.58 %	-4	0.00865
$^{206}\text{Pb}/^{208}\text{Pb}$	0.4661	0.4661	0.4661	0.09 %	0.4747	-1.82 %	2	0.00924
$^{207}\text{Pb}/^{208}\text{Pb}$	0.4025	0.4022	0.4023	0.12 %	0.4091	-1.66 %	1	0.01685
$^{206}\text{Pb}/^{207}\text{Pb}$	1.1556	1.1569	1.1562	0.12 %	1.1601	-0.33 %	1	0.00335

¹calculated as the mean of two times the standard error of the slope.

²percentual residue of the mean determined isotope ratio to the certified value.

³mass difference of the corresponding isotopes.

⁴calculated correction factor according to Equation 7

The obtained correction factors of the BAM solutions were applied to correct the measured isotope ratios of the MBH for mass bias. Table 4.7 shows the results.

Table 4.7: Measured and corrected values of liquid MBH measurements:

Ratio	Measured value	Error*	Corrected value
$^{206}\text{Pb}/^{204}\text{Pb}$	17.781	0.14 %	17.466
$^{207}\text{Pb}/^{204}\text{Pb}$	15.943	0.14 %	15.627
$^{208}\text{Pb}/^{204}\text{Pb}$	38.866	0.14 %	37.522
$^{206}\text{Pb}/^{208}\text{Pb}$	0.4572	0.07 %	0.4657
$^{207}\text{Pb}/^{208}\text{Pb}$	0.4098	0.09 %	0.4167
$^{206}\text{Pb}/^{207}\text{Pb}$	1.1145	0.09 %	1.1182

*calculated as two times the standard error of the slope (t-value for two tailed probability level of 95 % and 3998 degrees of freedom = 1.96)

The given uncertainty represents the precision of the measurement. Values around 0.1 % are received for the liquid measurements (Table 4.7). For measurements using laser ablation, the precision is a factor 10 - 20 worse (see chapter 4.3.4) because the signals are much less constant because of the sample intake using laser ablation. The strong fluctuation in combination with the sequential measurement of a quadrupole mass filter is leading to a bigger error.

A possible remaining systematic error source for the received isotope ratios of the liquid measurements arises from the different sample matrices of the used solutions. The target element Pb and the acid concentration are approximately the same in the solutions of the BAM and the MBH reference materials (shown in chapter 3.4.2.2, Table 3.3). But while the solid BAM contains 45 ppm Pb in a 95 % Cu / 5 % Ag matrix, the MBH contains 2070 ppm (0.207 %) Pb in a matrix of approximately 80 % Ag, 20 % Cu and several other elements from the ppm range up to 1.5 %. This has an influence on the plasma conditions regarding the ionisation efficiency and may lead to small errors. But the effect has mainly an influence on the gained absolute signal intensities rather than the relative intensities of different isotopes of one element. Because isotopic ratios of one chemical element (Pb) are determined, the effect should be neglectable with regard to the achieved precision.

The determined isotope ratios of the MBH reference material (Table 4.7) are used to correct for mass bias and instrumental drift in the coin sample measurements with laser ablation by bracketing each set of sample measurements with the MBH standard.

4.3.4 Sample Measurements

The measurement procedure and the LA and ICP-MS parameters are described in chapter 3.7.3.

Four lines with different laser parameters were measured with the goal to acquire data in different signal intensity levels. The measurement with the highest signal intensities that still lay low enough to be detected only with the counting detector (electron multiplier; $< 1.5 \cdot 10^6$ cps) for ^{208}Pb (highest abundance, 52.4 %) were used for evaluation. The line scans were set in the center of the coins cores to represent the Pb-isotopic composition of the original alloy without the influence of a corrosion caused change in the outer layers.

Figure 4.24 shows a plot of the isotopic ratio $^{206}\text{Pb}/^{207}\text{Pb}$ against $^{206}\text{Pb}/^{204}\text{Pb}$ of all measured coins and the MBH bracketing standard. It can be observed, that one big cluster is present and can clearly be distinguished from the reference material's result. Some coins separate from the cluster's center to lower $^{206}\text{Pb}/^{207}\text{Pb}$ and $^{206}\text{Pb}/^{204}\text{Pb}$ ratios (lower left side of the cluster) and some to higher $^{206}\text{Pb}/^{207}\text{Pb}$ and $^{206}\text{Pb}/^{204}\text{Pb}$ ratios (upper right side of the cluster), while most coins show ratios in between those edge values (center of the cluster).

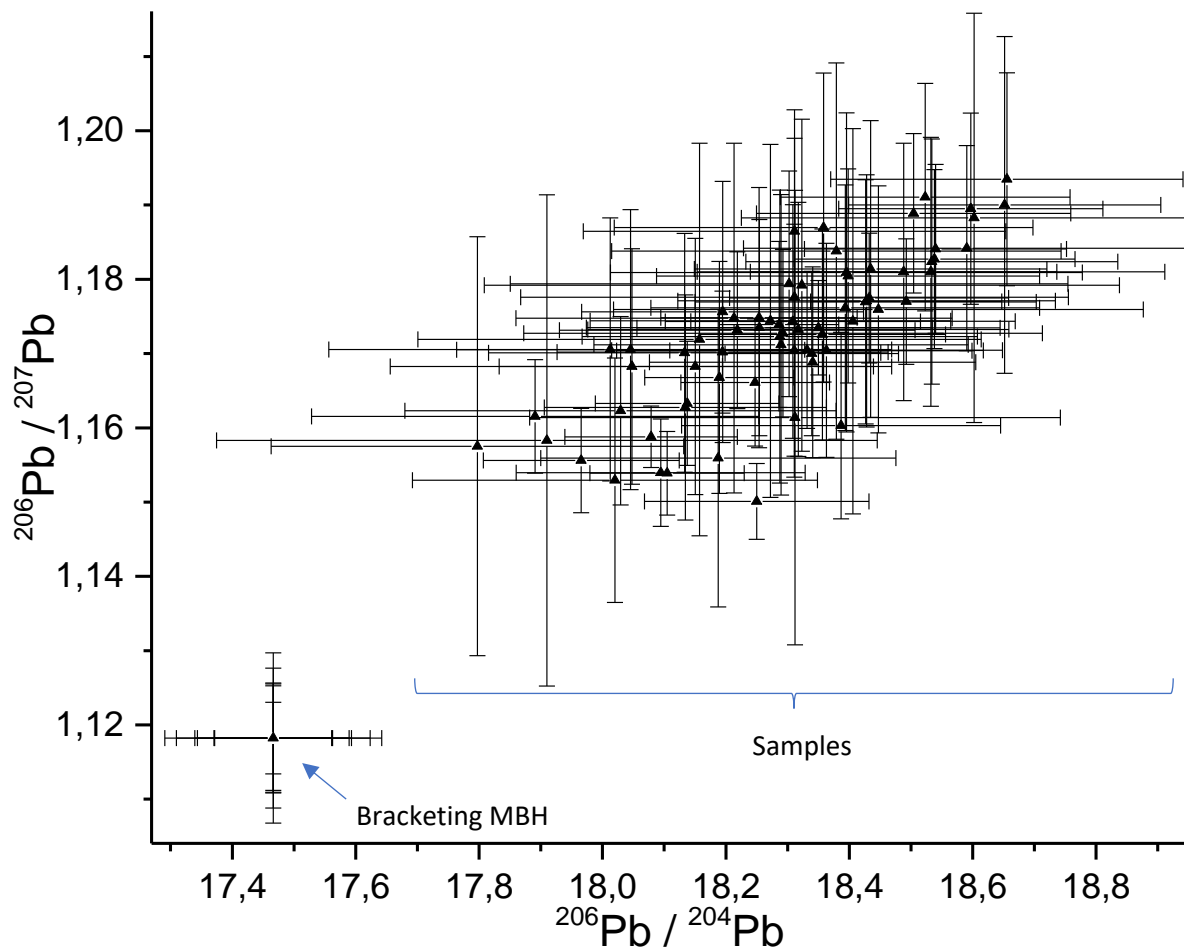


Figure 4.24: Ratioplot ($^{206}\text{Pb}/^{207}\text{Pb}$ | $^{206}\text{Pb}/^{204}\text{Pb}$) of LA-ICP-MS measurements of all coins and bracketing standard (MBH).

The error bars of most coins are several times larger as for the bracketing standard for several reasons: Because the MBH has a very homogeneous Pb distribution, the gained measurement signals are more constant than those of the coins, which generally show a very inhomogeneous Pb distribution (4.2.5.4). The quadrupole mass analyser, which the used instrument is equipped with, measures sequentially. Therefore, a changing signal results in a bigger uncertainty in the ratio determination. If the scanned line passes over a high concentrated spot in the coin measurements, the signal moves too high and the MS switches to analogue detection (Faraday cup; $> 1.5 \cdot 10^6$ cps). As a result, the data cannot be evaluated with the required precision. When relatively low concentrated sections are scanned during a measurement, the low signal intensities lead to an increasing error due to counting statistics. The mentioned reasons make the inhomogeneous lead distribution in the roman coins challenging for ratio determination with the available instrumentation.

The error bars, calculated as the standard deviation of the determined ratios in a split signal (described in 4.3.2.5), are a conservative estimation. By using the standard error of the mean and considering each section of the split signals as an independent measurement, the error values would be divided by the square root of the number of measurements. The signals were split in nine section of 250 data points each, therefore, the received error bars would be a factor three smaller than displayed in Figure 4.24 and Figure 4.25.

With respect to the conservatively estimated error bars, no clusters can be distinguished. If the coins would have been manufactured of resources that come from specific places, the isotopic signature would be preserved and with a reference standards of certain mining areas, the coin could be assigned. But in this time, due to the size of the Roman Empire and its numerous war efforts, an enormous number of silver sources were available through mining areas over the whole empire and the loot of in war conquered areas. It can be assumed, that the mined ores from different areas as well as other silver objects were refined and melted together in batches, leading to a mixing of the original Pb-isotopic composition and disguising the original source of the resources.

Figure 4.24 is meant to give a brief overview over all measured coins, but it is too crowded with data points and error bars to see any details. Therefore, a set of coins of different consulates and origin times were selected from the center and the edges of the cluster in Figure 4.24 and are shown in Figure 4.25. The isotopic ratios, the relative error and the consulate and time of origin of the displayed coins are listed in Table 4.8.

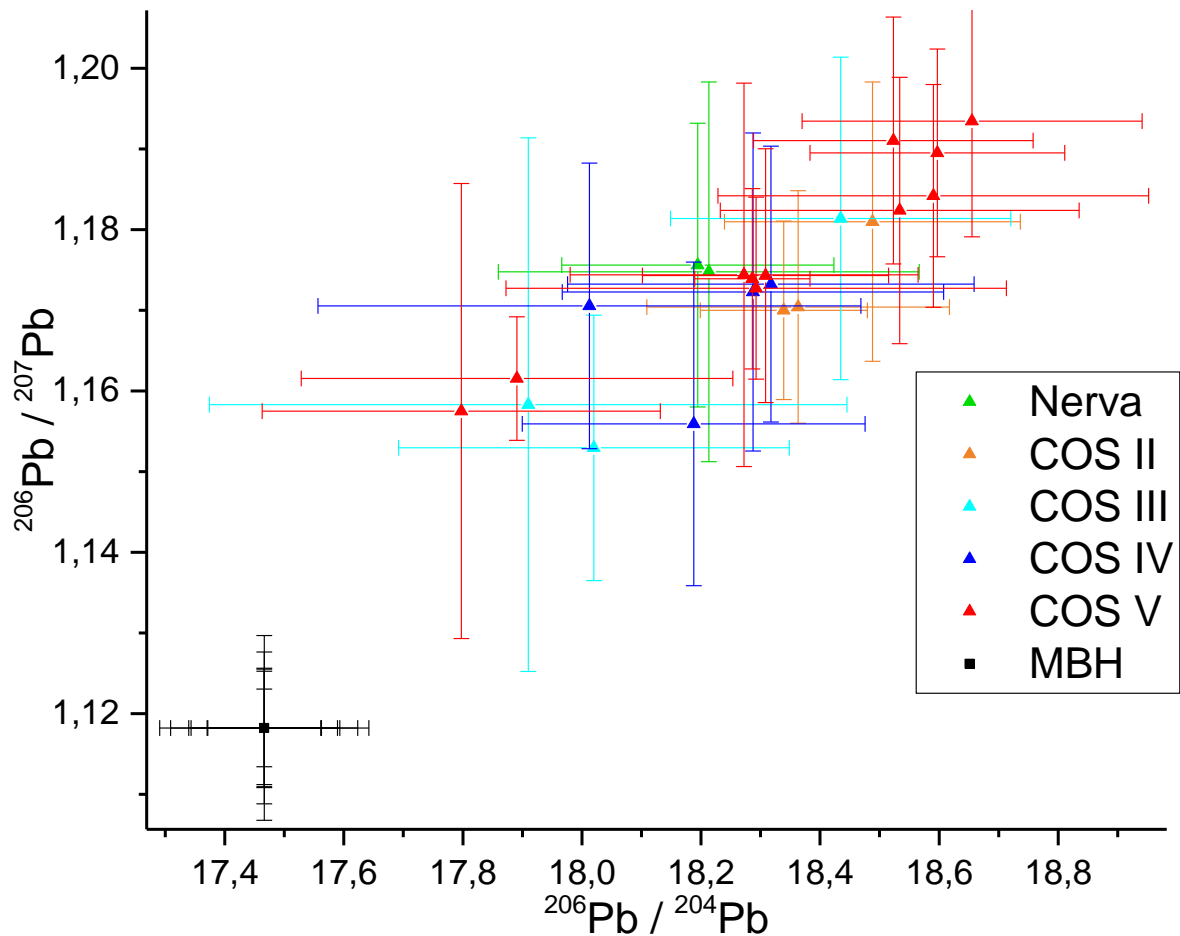


Figure 4.25: Ratioplot ($^{206}\text{Pb}/^{207}\text{Pb}$ | $^{206}\text{Pb}/^{204}\text{Pb}$) of LA-ICP-MS measurements of a selection of coins and bracketing standard (MBH). Colouring refers to Table 4.8.

The two coins of Nervas ruling time (green) lie close together in the center of the cluster, suggesting the same material origin. Of the analysed coins of Traians second consulate (orange), two are placed close together centered, whereas one is shifted to a higher $^{206}\text{Pb}/^{207}\text{Pb}$ and $^{206}\text{Pb}/^{204}\text{Pb}$ ratio. Two of the analysed coins of Traians fourth (blue) consulate are centered in the middle of the cluster and two are shifted to lower $^{206}\text{Pb}/^{207}\text{Pb}$ and $^{206}\text{Pb}/^{204}\text{Pb}$ ratios. The isotopic ratios of the third (azure) and fifth consulate scatter over the whole cluster, suggesting no connection of their material origin.

By a generalised comparison of the isotopic ratios with the consulate and year of the selected coins (Figure 4.25, Table 4.8), no clear connection can be observed. Coins of different consulates can be found in each region, and in each region, coins from different consulates and manufacturing times can be found. This again supports the already stated suggestion, that a mixing of the isotopic composition happened due to combination of resources from different origins and probably some recycling and remelting procedures over the centuries. This assumption also is supported by the fact, that the most coins are located in the center of the black cluster in Figure 4.24, which represents a mixture of edge values.

Table 4.8: Pb-isotope ratios and relative errors of the in Figure 4.25 shown selected coins with consulates and times of origin:

Colour ¹ / Consulate	Sample / Coin no.	Year	²⁰⁶ Pb/ ²⁰⁷ Pb	Error ² [%]	²⁰⁶ Pb/ ²⁰⁴ Pb	Error ² [%]
Black	MBH	-	1.118	0.71 ³	17.466	0.74 ³
Green Nerva	1	AD 97	1.176	1.49	18.195	1.26
	2	AD 97	1.175	2.00	18.213	1.94
Orange COS II	7	AD 98	1.181	1.47	18.488	1.34
	10	AD 98 – 99	1.170	1.23	18.363	1.38
	11	AD 98 – 99	1.169	0.95	18.339	0.77
Azure COS III	12	AD 100	1.153	1.43	18.020	1.82
	13	AD 100	1.158	2.86	17.910	2.99
	15	AD 100	1.181	1.69	18.435	1.55
Blue COS IV	17	AD 101 – 102	1.156	1.73	18.188	1.58
	19	AD 101 – 102	1.171	1.51	18.013	2.53
	23	AD 102	1.172	1.68	18.287	1.75
	28	AD 102	1.173	1.46	18.317	1.86
Red COS V	31	AD 104 – 105	1.173	0.96	18.293	2.30
	32	AD 104 – 105	1.182	1.40	18.534	1.63
	33	AD 104 – 105	1.184	1.17	18.590	1.95
	37	AD 107	1.190	1.08	18.597	1.15
	40	AD 107 – 108	1.191	1.29	18.523	1.27
	41	AD 107 – 108	1.174	0.95	18.286	0.53
	43	AD 107 – 109	1.183	1.02	18.538	1.23
	48	AD 108 – 109	1.158	2.44	17.797	1.88
	49	AD 108 – 109	1.162	0.66	17.891	2.03
	51	AD 110	1.190	1.20	18.655	1.53
	52	AD 110	1.168	1.36	18.048	2.17
	64	AD 114 – 116	1.174	1.34	18.308	1.13
	65	AD 114 – 116	1.174	2.02	18.272	1.60

4.4 Tandem – LIBS/LA-ICP-MS

The data of each measurement region for LIBS and ICP-MS was accumulated, wherefore the plots refer to an average value over the selected region. The measurements were performed with the same laser parameters as the separate LIBS measurements (Table 4.1), except that the repetition rate was set to 5 Hz. The measurement procedure is described in section 3.8. Figure 4.26 shows the selected coins with the measurement regions marked in coloured ellipses. The colouring refers to the sample names in the figures that show the evaluated results of the obtained LIBS data (Figure 4.27) and ICP-MS data (Figure 4.28).

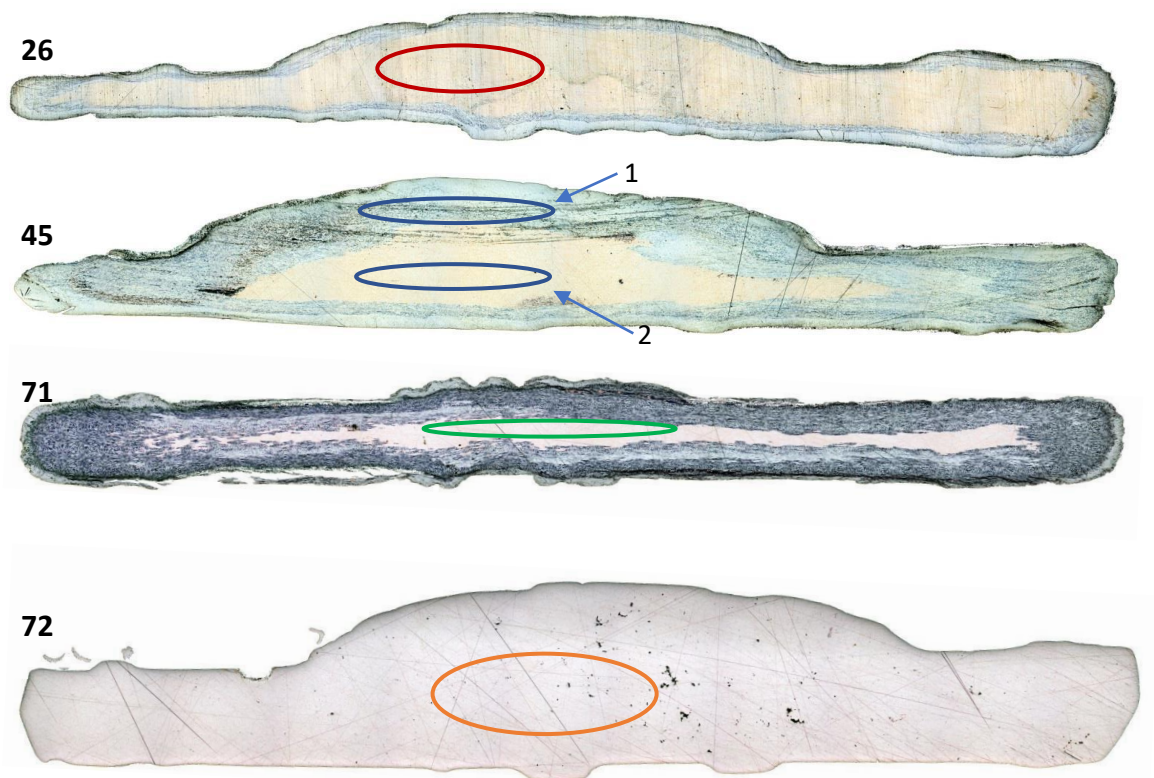


Figure 4.26: Coins no. 26, 45, 71, and 72 used for Tandem – LIBS/LA-ICP-MS measurements with measurement regions marked.

The MBH reference material was measured before (MBH.1) and after (MBH.2) the selected of coins in the Tandem LIBS/LA-ICP-MS setup. The evaluated emission lines of silver, copper, gold and lead in Figure 4.27 show the same results for MBH.1 and MBH.2 considering the mean intensities as well as the extent of the error bars. Each measurement series consisted of 15 spots on a different location of the sample and on each spot 15 shots were performed, in which the shots 6 – 15 were accumulated. The stability of the mean values demonstrates the stability of the LIBS instrument over a time of approximately 2 hours. The error bars, calculated as two times the standard deviation, demonstrate

the instruments precision, because the elements are distributed homogeneously in the MBH reference material.

It should be noted, that gold and lead are scaled on a secondary axis (Figure 4.27, right axis). Therefore, the error bars appear much bigger for gold and lead in the Figure 4.27, though in absolute numbers they are much smaller.

Generally, the errors of the evaluated emission lines of the coins are much bigger as of the reference material. This results from the inhomogeneous element distribution in the coins as can be seen in the LIBS imaging section (4.2.5.4) and because the evaluated results are displayed as mean values and standard deviation of several measurement spots in a selected region on the coins cross section.

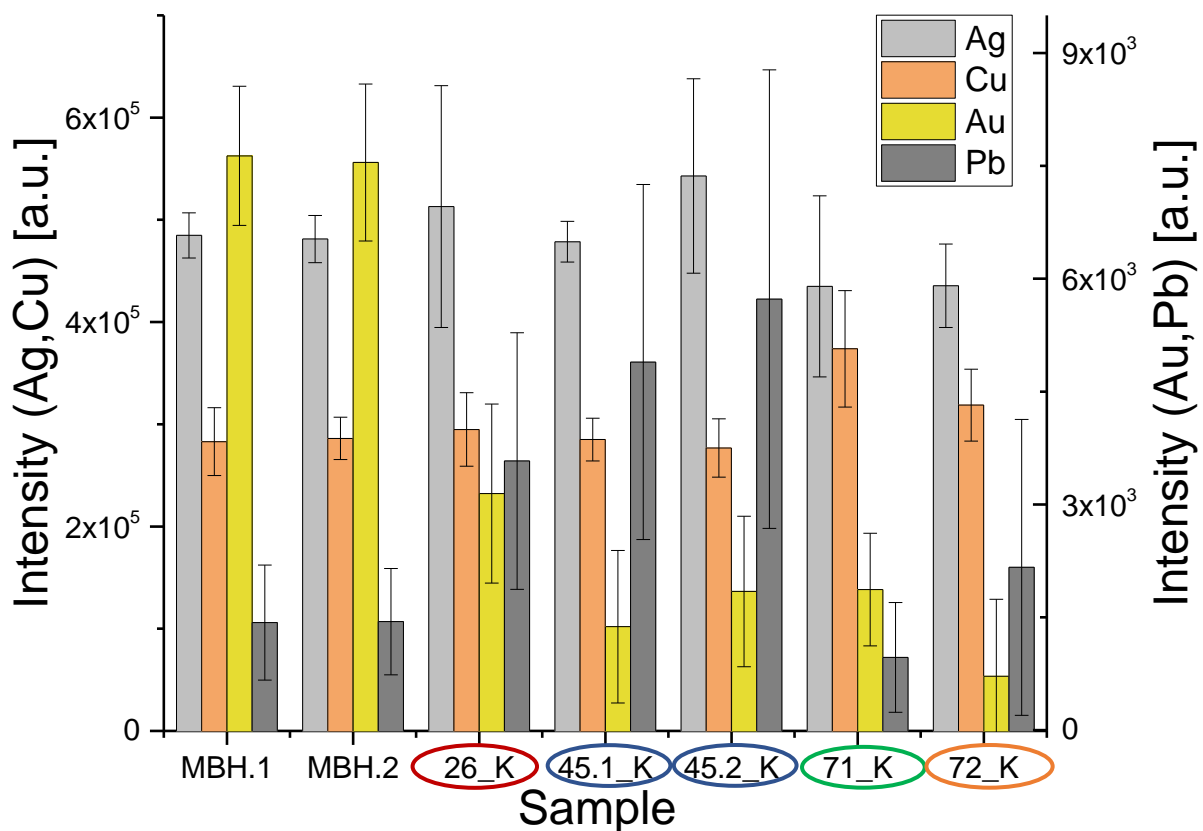


Figure 4.27: Comparison of the marked sections in the coins (Figure 4.26) measured with LIBS in Tandem setup. Evaluated emission lines (Ag, Cu, Au, Pb) of the coins no. 26, 45, 71 and 72. The colouring of the sample name surrounding circles refers to the marked measurement regions.

The silver and copper content in the MBH are approximately 78 % and 20 %, what is very similar to most of the roman coins. Some coins show a higher silver content and complementarily a lower copper content. For other coins the trend is exactly the opposite. It can be observed, that the gold content of the MBH (1.48 %) is much higher than in the analysed coins whose gold content varies from 0 – 0.3 % according to μ -XRF measurements in previous work (Appendix 8.2, Table 8.2). The relative intensity of gold in the MBH and the shown coin samples does not fit to this difference in concentration. The lead concentration in the MBH (0.2 %) and the μ -XRF results show contents from 0.05 % – 0.4 % Pb in the

coins. The lead intensity of the coins no. 26 and no. 45 is a factor 3 to four higher than for the MBH. As for gold, these relative intensities do not accord to the difference in concentration. This can also be explained with the observed inhomogeneity that could be observed with LIBS imaging. Depending on the selected measurement region the results vary strongly and lead to an uncertainty of the punctual LIBS measurements as well as of the μ -XRF results.

In coin no. 45 two measurement regions were selected. One in the core of the coin and one in the outer layer (regions shown in Figure 4.26). As shown before in the spot measurements using LIBS (chapter 4.2.5.2), in the outer layer a slight silver enrichment can be observed compared to the core of the coin.

Figure 4.28 shows a plot of the isotopic ratio $^{207}\text{Pb}/^{208}\text{Pb}$ against $^{206}\text{Pb}/^{207}\text{Pb}$ that were obtained in the Tandem-LIBS/LA-ICP-MS setup. The data comes from exactly the same measurement as the LIBS results shown in Figure 4.27.

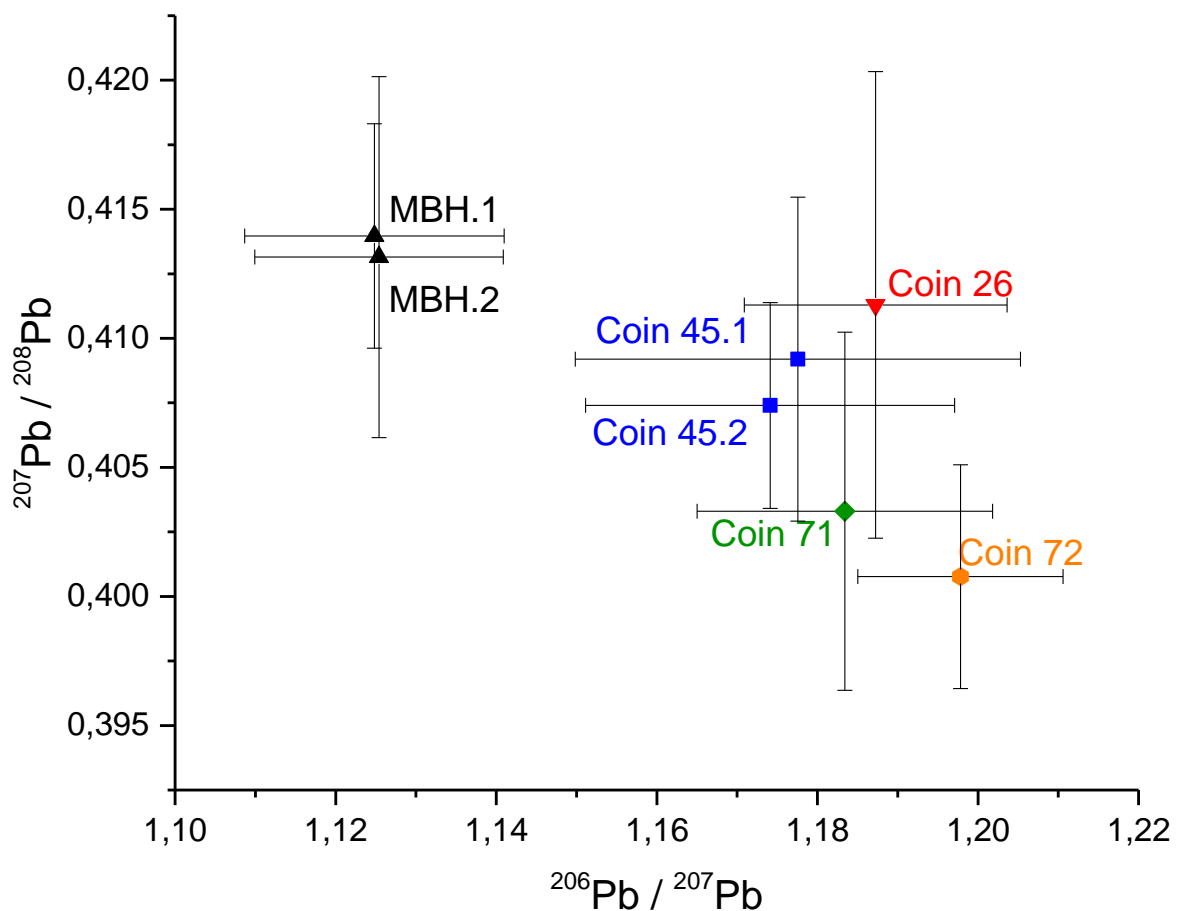


Figure 4.28: Ratioplot ($^{207}\text{Pb}/^{208}\text{Pb}$ | $^{206}\text{Pb}/^{207}\text{Pb}$) of Tandem – LIBS/LA-ICP-MS measurements. The colouring refers to the marked measurement regions on the coin's cross sections in Figure 4.26.

The MBH reference material was measured before and after the set of coins can be distinguished of the coin samples in the ratio plot (Figure 4.28). In respect to the error bars, the analysed coins cannot

be differentiated by their Pb-isotopic ratios. The mean values of both measured regions in coin no. 45 (45.1 and 45.2) are close together, to the other coins the distance is larger.

It should be noted, that the error bars represent the standard deviation. If the standard error of the mean would be displayed, the error bars would be smaller by the factor \sqrt{n} , where n is the number of measurements ($\sqrt{15} \sim 3.8$ for the MBH; $\sqrt{20} \sim 4.5$ for the coins). According to this uncertainty, the coins no. 45 and 26 could be distinguished from coin no. 71 and from coin no. 72.

The Tandem-LIBS/LA-ICP-MS setup produced data in acceptable quality about the elemental composition as well as the Pb isotopic composition, representing a method with a high information yield combined with the least possible sample invasiveness. The LIBS data has the same quality as in the separate LIBS point measurements (chapter 4.2.5), because the same laser parameters were used. The precision in the obtained ratio plot is comparable to those in the separate LA-ICP-MS measurements, but only because with the Tandem setup, the results of 15 to 20 measurements were combined, whereas in the separate LA-ICP-MS measurements, one line-scan with the best intensity level was evaluated. A major drawback in the Tandem setup was, that it could only be measured with 5 Hz repetition rate because else the signal would be too high for the ICP-MS to only use the counting detector. With a low repetition rate the signal is less stable, leading to less precision. This could not be compensated by milder laser parameters, because else the plasma conditions would not be suitable for a proper LIBS spectra's emission intensity. But the resulting imprecision can be counteracted by repeated measurements until the required precision is reached.

4.5 Example for the Procedure of Data Combination

Figure 4.29 shows a scheme for the procedure of data combination of the applied methods to clarify possible suggestions. At first a microscopic image of the cross section was recorded. On the it is observable if any abnormalities as different coloured phases or layers, segregations, cracks or other characteristics are present. Then either spot measurements can be performed in regions of interest or as in this case, the whole cross section was scanned using LIBS. The data was processed to elemental maps showing the distribution of the evaluated elements. In the given example (coin no. 39, Traian COS V, approx. AD 107 – 108), the characteristic particularity was a layer containing aluminium and zinc only on one side of the coin, which also was heavier corroded than the other side (elemental maps are shown in the imaging section 4.2.5.4, Figure 4.18). Such a characteristic was not found in any other of the analysed coins. Therefore, it was suggested that maybe the coin was renewed at a time later as its original manufacturing, by adding a new layer of a different alloy (plating). To verify that guess, LA-ICP-MS line scans were performed in the center of the coin and in the suspected layer. The significant

difference of the evaluated Pb-isotopic composition (Figure 4.29, right top) confirmed the suggestion, that the layer came from a different source than the original alloy.

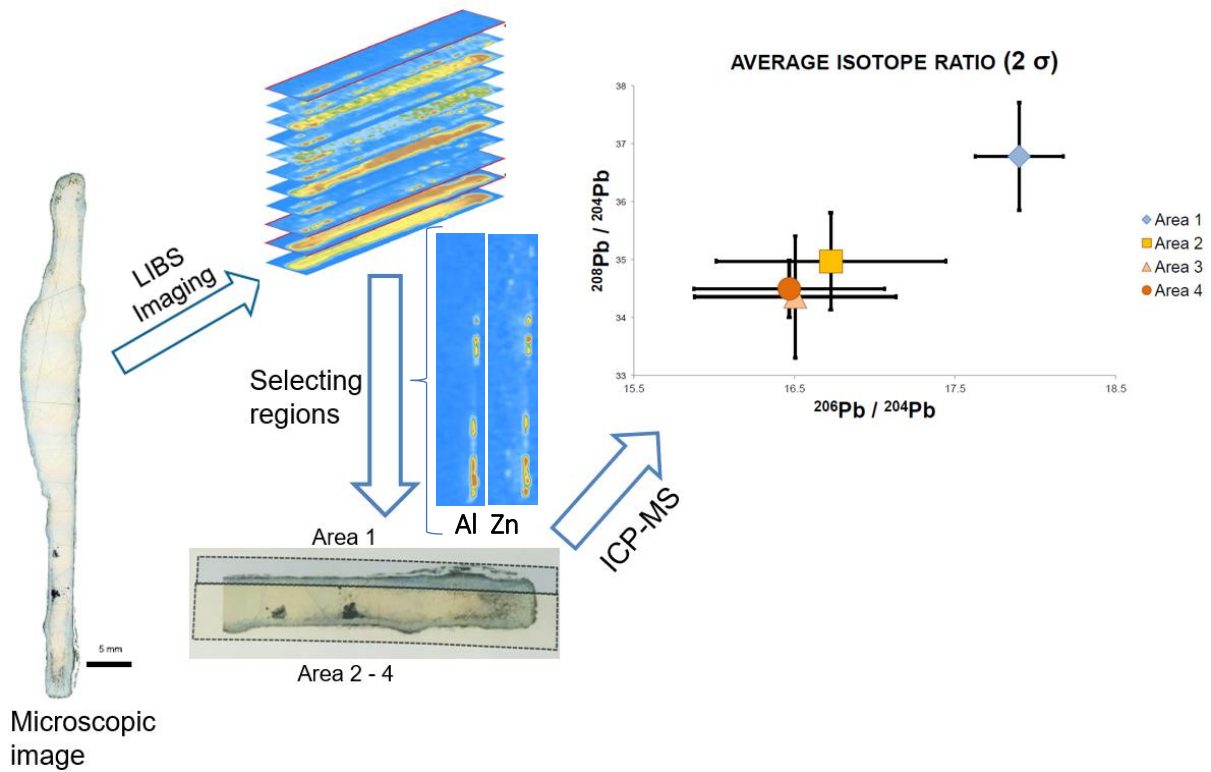


Figure 4.29: Example for the procedure of data combination of multiple methods.

By this principle some questions about the history and the whereabouts of particular objects might be clarified. It could also be used to identify forgeries, membership of an analysed object to a class and furthermore.

5 Summary and Conclusion

Modern analytical methods represent a powerful tool to gather information that can give answers or hints on question about cultures of our past. An important piece of remnant is given by the currency. The method development and application of an analysis technique for this research field could be shown in this thesis. Methods of three different instrumental setups for a minimal invasive determination of the elemental composition and distribution as well as the lead isotopic composition in silver coins were developed and optimised.

Using microscopic images, it was shown that some coins contain visible layers surrounding the core that is containing the original alloy with a eutectic silver-copper structure. Inside the coins different inhomogeneities appearing as lines, spots and other structures can be seen, seeming like inclusions or segregations (chapter 4.1). The core alloy and the visible layers and inhomogeneities were analysed with laser induced breakdown spectroscopy.

The developed LIBS method is capable of the simultaneous determination of the bulk elements silver and copper, and also impurities of gold, lead, bismuth, tin, zinc, sodium, potassium, calcium, magnesium, barium, aluminium and silicon (4.2.2) in the sampled denarii. By scanning the sample with repeating laser pulses and following evaluation of the identified non-interfered emission lines, elemental distributions could be imaged. By performing spot measurements with 10 or more accumulated spectra, a better signal to noise ratio is achieved. This was used to identify the elements present in small spots that were of particular interest after investigation of the microscopic images (chapter 4.2.5.3). Further, trends were investigated by comparing the core alloy's composition of different coins and comparing the elemental composition of the core alloy with the surrounding layers (chapter 4.2.5.1 and 4.2.5.2). Thereby a silver enrichment in the surface layers could be identified. The surface layers also showed the presence of the elements sodium, potassium, calcium, magnesium, barium, aluminium and silicon, which are elements that typically appear in the earth's crust and who are present in the coins surface due to contamination and corrosion.

The generated elemental maps (chapter 4.2.5.4) show inhomogeneous distribution of the main components in the core of some coins, while in others the distribution of silver and copper is comparably homogeneous. The corrosion influenced outer layers are clearly visualised, showing the presence of the mentioned elements that are most prominent in the earth's crust. Inside the coins these elements are present in some parts too. On the one hand in form of small spots, that were identified as inclusions which might have come into the melt as solid particle contamination in the

manufacturing process. On the other hand, larger regions containing sodium, potassium and calcium combined with an abnormal distribution of silver and copper point out a possible recycling or renewing of some coins.

A LA-ICP-MS method was developed to determine Pb-isotope ratios of ^{204}Pb , ^{206}Pb , ^{207}Pb and ^{208}Pb . To correct for the ^{204}Hg interference on the ^{204}Pb signal, ^{202}Hg was measured and the corresponding signal was corrected according to the natural abundance of the Hg isotopes. Further, a background subtraction and spike elimination were performed. For mass bias and instrumental drift was corrected by using a bracketing standard. To partially compensate for the error that is caused by the sequential measurement of the quadrupole mass analyser, the raw data in each sweep was linearly interpolated to a reference time (chapter 4.3.2).

The method was applied on the Roman coin samples (chapter 3.7.3). Results showed, that the Pb-isotope ratios of the samples do not cluster into separate distinguishable clusters. They only show one big cluster with the highest density of data points in the center. Coins with the edge values of the cluster can be distinguished from those on the other edge, but due to the estimated errors no certain statements regarding different classes and origins can be made. By comparing the mean values of selected coins of different consulates and times of original manufacturing (Figure 4.26, Table 4.8), it is observed that for most coins no connection of the isotopic signature of the used raw materials can be made with the consulate and the traditioned time of manufacturing.

The conclusion is made, that this is most probably caused by the use of resources that came from many different origins. Due to the enormous size and numerous wars and conquests, the Roman empire had access to many silver sources in form of mines throughout the empire, but also in form of plenty of loot of its successful war efforts. The written tradition which states that under Traian's rule a widespread coin collection initiative took place, that led to a decrease in the denarii's fineness by remelting and addition of more copper, further supports the suggestion that the isotopic signatures of the original sources are mixed up.

Further the methods of both mentioned separate techniques were successfully implemented and optimised in a combined Tandem-LIBS/LA-ICP-MS method (chapter 4.4). Thereby the elemental information and the Pb isotopic information are acquired in one measurement with the intrinsic identical sampling volume (corresponding to laser pulses). This represents the least invasive approach for the given application, what is of great importance in the field of analysis of ancient findings and art objects. At last an example was given, in which the combination of the acquired information of both techniques (elemental information + isotopic information, chapter 4.5) is used to verify suggestions. With LIBS

imaging a special characteristic in the outermost layer on one side of one coin was observed, that suggested a material not belonging to the original manufactured coin. After determination of the Pb-isotopic ratios and comparison of that specific layer with the rest of the coin, it could be shown that the layer is significantly different from the rest of the coin, what is proving that this material has a different origin and was probably added at a later time in an attempt to renew the coin.

6 Outlook

To further improve some aspects of the method as well as the quality of the obtained measurement data for the in this work given application, several suggestions can be made.

The developed LIBS method can be expanded to more elements by measuring more pure metal standards and finding non-interfered emission lines. Further, by measuring of matrix matched standards for the elements of interest with the used measurement parameters, a calibration and quantification can be created.

As pointed out, least possible invasiveness is an important issue in the field of analysis of ancient and valuable objects. With the least invasive approach, the Tandem LIBS/LA-ICP-MS setup, a major problem was the poor washout behaviour of the implemented sample chamber, which could be surpassed by designing and manufacturing an optimised ablation chamber for that purpose in the LIBS instrument.

To also take account for that requirement, a possible improvement would be the use of a femto-second laser for laser ablation. The pulse duration in a femto-second laser is so short, that no heat effects occur, leaving the sample surface with less recognizable damage. Another desired effect is the production of smaller particles and a narrower particle size distribution, leading to better ionisation conditions in the ICP.

A main issue with the measurement of lead isotopes was the inconstant signal that was produced by LA-ICP-MS with the maximum repetition rate of 20 Hz. This could be much enhanced by a laser that is capable of repetition rates up to the kHz range. A higher repetition rate, compensated by less energy per pulse to keep the produced signal in the same intensity range, would result in a much more constant signal. A more constant signal could also be gained by implementing a diffuser, which's purpose is to provide a mixing of the gas flow that exits the ablation chamber leading to a more uniform particle concentration.

By providing a more constant signal, the precision with the used quadrupole ICP-MS instrument could be improved for a certain extent. An even further improvement of the precision could be gained by using a multichannel magnetic sector ICP-MS instrument, which measures all incoming isotopes at the same time. Following a changing signal would not have such a big influence.

At last, by chemometric evaluation and the application of sophisticated statistic methods, the obtained data can be used to gain more information of the measured samples.

7 Acknowledgements

Finally, I want to express my greatest gratitude to all people directly or indirectly involved in this project. At first, Prof. Andreas Limbeck for offering me this project, for admitting me into his working group and for providing me all necessary requirements as well as numerous aids, tips and hints to surpass problems and reach progress in my work. Prof. Manfred Schreiner for originally coming up with the project and for providing the Roman coins that were used as samples.

My main student supervisor Felix Horak especially is to be thanked for the great amount of time he invested to help me in a general way and to teach me in scientific as in practical issues. Further gratitude I want to express to Felix and to Lukas Brunnbauer for correction-reading my final thesis.

At last I want to thank the entire working group, Andreas, Felix, Maxi, Max, Lukas and Christopher for the very comfortable atmosphere in our group, for willingly answering numerous questions and for the discussion of different matters in a work-related but also in an interpersonal way.

8 Appendix

8.1 Listing of Analysed Roman Denarii

Table 8.1: Analysed Roman denarii: [4]

NERVA								
Nr.	Nominale	Averslegende	Reverslegende	Reverstyp	Datierung	Zitat BMC	Gewicht	Stempelstellung
1 61	Denar	IMP NERVA CAES AVG P M TR P COS III P P	AEQVITAS AVGVST	Aequitas steht nach links	1. Jänner – 17. September 97	24	3,63 g	6 Uhr
2 62	Denar	IMP NERVA CAES AVG P M TR P COS III P P	FORTVNA AVGVST	Fortuna steht nach links	1. Jänner – 17. September 97	37	2,69 g	7 Uhr
3 63	Denar	IMP NERVA CAES AVG P M TR P COS III P P	SALVS PVBLICA	Salus sitzt nach links	1. Jänner – 17. September 97	48	3,28 g	6 Uhr

TRAIAN, CONSULAT II (98–99 n. Chr.)

Nr.	Nominale	Averslegende	Reverslegende	Reverstyp	Datierung	Zitat BMC	Gewicht	Stempelstellung
4 64	Denar	IMP NERVA CAES TRAIAN AVG GERM P M	TR P COS II P P	Abundantia sitzt nach links	28. Jänner – ca. Februar 98	47 Anm.	3,33 g	7 Uhr
5 65	Denar	IMP CAES NERVA TRAIAN AVG GERM	PONT MAX TR POT COS II	Abundantia sitzt nach links	ca. Februar 98 – ca. Spätherbst 98	9	3,28 g	6 Uhr
6 66	Denar	IMP CAES NERVA TRAIAN AVG GERM	PONT MAX TR POT COS II	Abundantia sitzt nach links	ca. Februar 98 – ca. Spätherbst 98	9	3,12 g	6 Uhr
7 67	Denar	IMP CAES NERVA TRAIAN AVG GERM	PONT MAX TR POT COS II	Pax steht nach links	ca. Februar 98 – ca. Spätherbst 98	14	3,36 g	7 Uhr
8 68	Denar	IMP CAES NERVA TRAIAN AVG GERM	P M TR P COS II P P	Victoria sitzt nach links	ca. Spätherbst 98 – Ende 99	42	3,31 g	6 Uhr
9 69	Denar	IMP CAES NERVA TRAIAN AVG GERM	P M TR P COS II P P	Victoria sitzt nach links	ca. Spätherbst 98 – Ende 99	42	2,88 g	6 Uhr
10 7	Denar	IMP CAES NERVA TRAIAN AVG GERM	P M TR P COS II P P	Victoria sitzt nach links	ca. Spätherbst 98 – Ende 99	42	2,78 g	6 Uhr
11 2	Denar	IMP CAES NERVA TRAIAN AVG GERM	P M TR P COS II P P	Victoria sitzt nach links	ca. Spätherbst 98 – Ende 99	42	2,56 g	6 Uhr

TRAIAN, CONSULAT III (100 n. Chr.)

Nr.	Nominale	Averslegende	Reverslegende	Reverstyp	Datierung	Zitat BMC	Gewicht	Stempelstellung
12 3	Denar	IMP CAES NERVA TRAIAN AVG GERM	P M TR P COS III P P	Concordia sitzt nach links	100	64 Var. Büste b	3,31 g	6 Uhr
13 70	Denar	IMP CAES NERVA TRAIAN AVG GERM	P M TR P COS III P P	Concordia sitzt nach links	100	64	3,15 g	6 Uhr
14 71	Denar	IMP CAES NERVA TRAIAN AVG GERM	P M TR P COS III P P	Pax steht nach links	100	72	3,45 g	5 Uhr
15 72	Denar	IMP CAES NERVA TRAIAN AVG GERM	P M TR P COS III P P	Pax steht nach links	100	72	3,21 g	6 Uhr

TRAIAN, CONSULAT IIII, „Hauptgruppe“ (101–102 n. Chr.)

Nr.	Nominale	Averslegende	Reverslegende	Reverstyp	Datierung	Zitat BMC	Gewicht	Stempelstellung
16 4	Denar	IMP CAES NERVA TRAIAN AVG GERM	P M TR P COS IIII P P	Abundantia sitzt nach links	101 – 102	98	2,46 g	6 Uhr
17 6	Denar	IMP CAES NERVA TRAIAN AVG GERM	P M TR P COS IIII P P	Statue des Hercules frontal	101 – 102	86 Var. Büste b	2,93 g	6 Uhr
18 5	Denar	IMP CAES NERVA TRAIAN AVG GERM	P M TR P COS IIII P P	Statue des Hercules frontal	101 – 102	86	2,89 g	6 Uhr
19 54	Denar	IMP CAES NERVA TRAIAN AVG GERM	P M TR P COS IIII P P	Statue des Hercules frontal	101 – 102	86 Var. Büste b	2,57 g	7 Uhr
20 7	Denar	IMP CAES NERVA TRAIAN AVG GERM	P M TR P COS IIII P P	Mars geht nach rechts	101 – 102	96	3,05 g	6 Uhr

TRAIAN, CONSULAT IIII, „Siegesgruppe“ (ca. 102 n. Chr.?)

Nr.	Nominale	Averslegende	Reverslegende	Reverstyp	Datierung	Zitat BMC	Gewicht	Stempelstellung
21 8	Denar	IMP CAES NERVA TRAIAN AVG GERM	P M TR P COS IIII P P	Victoria auf <i>prona</i> nach rechts	ca. 102 (?)	106	2,95 g	6 Uhr
22 9	Denar	IMP CAES NERVA TRAIAN AVG GERM	P M TR P COS IIII P P	Victoria auf <i>prona</i> nach rechts	ca. 102 (?)	106	2,32 g	6 Uhr
23 10	Denar	IMP CAES NERVA TRAIAN AVG GERM	P M TR P COS IIII P P	Victoria beschreibt Schild	ca. 102 (?)	111	2,96 g	6 Uhr
24 14	Denar	IMP CAES NERVA TRAIAN AVG GERM	P M TR P COS IIII P P	Victoria steht frontal	ca. 102 (?)	115 Var. Büste c	3,10 g	6 Uhr
25 12	Denar	IMP CAES NERVA TRAIAN AVG GERM	P M TR P COS IIII P P	Victoria steht frontal	ca. 102 (?)	120	2,90 g	6 Uhr
26 11	Denar	IMP CAES NERVA TRAIAN AVG GERM	P M TR P COS IIII P P	Victoria steht frontal	ca. 102 (?)	116	2,75 g	7 Uhr
27 13	Denar	IMP CAES NERVA TRAIAN AVG GERM	P M TR P COS IIII P P	Victoria steht frontal	ca. 102 (?)	120	2,66 g	6 Uhr
28 15	Denar	IMP CAES NERVA TRAIAN AVG GERM	P M TR P COS IIII P P	Victoria schwebt nach links	ca. 102 (?)	124	2,55 g	6 Uhr
29 16	Denar	IMP CAES NERVA TRAIAN AVG GERM	P M TR P COS IIII P P	Victoria opfert nach links	ca. 102 (?)	128	3,07 g	7 Uhr

TRAIAN, CONSULAT V, alte Legende (ca. 104–107 n. Chr.)

Nr.	Nominale	Averslegende	Reverslegende	Reverstyp	Datierung	Zitat BMC	Gewicht	Stempelstellung
30 17	Denar	IMP TRAIANO AVG GER DAC P M TR P COS V P P	S P Q R OPTIMO PRINCIPI	Dacia sitzt nach rechts	ca. 104–105	179	3,29 g	6 Uhr
31 18	Denar	IMP TRAIANO AVG GER DAC P M TR P COS V P P	S P Q R OPTIMO PRINCIPI	Dacia sitzt nach rechts	ca. 104–105	180	3,14 g	7 Uhr
32 19	Denar	IMP TRAIANO AVG GER DAC P M TR P COS V P P	S P Q R OPTIMO PRINCIPI	Fortuna sitzt nach links	ca. 104–105	203	2,82 g	7 Uhr
33 10	Denar	IMP TRAIANO AVG GER DAC P M TR P COS V P P	S P Q R OPTIMO PRINCIPI	Pax steht nach links auf Daker	ca. 104–105	214	3,30 g	6 Uhr
34 21	Denar	IMP TRAIANO AVG GER DAC P M TR P COS V P P	S P Q R OPTIMO PRINCIPI	Annona steht nach links	ca. 106–107	171	2,92 g	6 Uhr
35 22	Denar	IMP TRAIANO AVG GER DAC P M TR P COS V P P	S P Q R OPTIMO PRINCIPI	Felicitas steht nach links	ca. 106–107	193	3,18 g	7 Uhr
36 23	Denar	IMP TRAIANO AVG GER DAC P M TR P COS V P P	S P Q R OPTIMO PRINCIPI	Mars steht frontal	ca. 106–107	158	3,21 g	7 Uhr
37 24	Denar	IMP TRAIANO AVG GER DAC P M TR P COS V P P	S P Q R OPTIMO PRINCIPI	Mars eilt nach links	ca. 107	164	3,04 g	7 Uhr

TRAIAN, CONSULAT V, neue Legende (ca. 107–111 n. Chr.)

Nr.	Nominale	Averslegende	Reverslegende	Reverstyp (Zusatzleg.)	Datierung	Zitat BMC	Gewicht	Stempel- stellung
38 25	Denar	IMP TRAIANO AVG GER DAC P M TR P	COS V P P S P Q R OPTIMO PRINC	<i>tropaeum</i>	ca. 107–108	358 ff.	3,27 g	6 Uhr
39 24	Denar	IMP TRAIANO AVG GER DAC P M TR P	COS V P P S P Q R OPTIMO PRINC	<i>tropaeum</i>	ca. 107–108	358 ff.	2,95 g	6 Uhr
40 24	Denar	IMP TRAIANO AVG GER DAC P M TR P	COS V P P S P Q R OPTIMO PRINC	<i>tropaeum</i>	ca. 107–108	358 ff.	2,71 g	6 Uhr
41 28	Denar	IMP TRAIANO AVG GER DAC P M TR P	COS V P P S P Q R OPTIMO PRINC	Daker sitzt nach rechts auf Waffen, DAC CAP	ca. 107–108	385	2,77 g	6 Uhr
42 29	Denar	IMP TRAIANO AVG GER DAC P M TR P	COS V P P S P Q R OPTIMO PRINC	Aequitas steht nach links	ca. 107–109	281	3,18 g	6 Uhr
43 30	Denar	IMP TRAIANO AVG GER DAC P M TR P	COS V P P S P Q R OPTIMO PRINC	Aequitas steht nach links	ca. 107–109	284	3,19 g	6 Uhr
44 31	Denar	IMP TRAIANO AVG GER DAC P M TR P	COS V P P S P Q R OPTIMO PRINC	Aequitas steht nach links	ca. 107–109	284	3,02 g	6 Uhr
45 32	Denar	IMP TRAIANO AVG GER DAC P M TR P	COS V P P S P Q R OPTIMO PRINC	Aequitas sitzt nach links	ca. 108–109	288	2,59 g	6 Uhr
46 33	Denar	IMP TRAIANO AVG GER DAC P M TR P	COS V P P S P Q R OPTIMO PRINC	Felicitas steht nach links	ca. 108–109	301	3,14 g	7 Uhr
47 34	Denar	IMP TRAIANO AVG GER DAC P M TR P	COS V P P S P Q R OPTIMO PRINC	Felicitas steht nach links	ca. 108–109	303	3,23 g	6 Uhr
48 35	Denar	IMP TRAIANO AVG GER DAC P M TR P	COS V P P S P Q R OPTIMO PRINC	Roma sitzt nach links	ca. 108–109	276	2,96 g	6 Uhr
49 36	Denar	IMP TRAIANO AVG GER DAC P M TR P	COS V P P S P Q R OPTIMO PRINC	Victoria geht nach links auf Schilden	ca. 108–109	337	2,57 g	6 Uhr
50 37	Denar	IMP TRAIANO AVG GER DAC P M TR P	COS V P P S P Q R OPTIMO PRINC	Dacia sitzt nach links auf Waffen, DAC CAP	ca. 108–109	390	2,96 g	6 Uhr

Nr.	Nominale	Averslegende	Reverslegende	Reverstyp (Zusatzleg.)	Datierung	Zitat BMC	Gewicht	Stempel- stellung
51 38	Denar	IMP TRAIANO AVG GER DAC P M TR P	COS V P P S P Q R OPTIMO PRINC	Arabia steht frontal	ca. 110	297	3,60 g	7 Uhr
52 39	Denar	IMP TRAIANO AVG GER DAC P M TR P	COS V P P S P Q R OPTIMO PRINC	Arabia steht frontal	ca. 110	297	3,11 g	6 Uhr
53 40	Denar	IMP TRAIANO AVG GER DAC P M TR P	COS V P P S P Q R OPTIMO PRINC	Arabia steht frontal	ca. 110	297 Var. Büste c	2,97 g	6 Uhr
54 41	Denar	IMP TRAIANO AVG GER DAC P M TR P	COS V P P S P Q R OPTIMO PRINC	Felicitas steht nach links an Säule	ca. 110	305	3,09 g	6 Uhr
55 42	Denar	IMP TRAIANO AVG GER DAC P M TR P	COS V P P S P Q R OPTIMO PRINC	Aeternitas steht frontal, AET AVG	111	374	3,19 g	7 Uhr
56 43	Denar	IMP TRAIANO AVG GER DAC P M TR P	COS V P P S P Q R OPTIMO PRINC	Pax steht nach links, PAX	111	401	3,26 g	6 Uhr

TRAIAN, CONSULAT VI, vor der Annahme des Optimus-Namens (112–114 n. Chr.)

Nr.	Nominale	Averslegende	Reverslegende	Reverstyp (Zusatzleg.)	Datierung	Zitat BMC	Gewicht	Stempel- stellung
57 47	Denar	IMP TRAIANO AVG GER DAC P M TR P COS VI P P	S P Q R OPTIMO PRINCIPI	Arabia steht frontal, ARAB ADQ	ca. 112	474	2,70 g	6 Uhr
58 45	Denar	IMP TRAIANO AVG GER DAC P M TR P COS VI P P	S P Q R OPTIMO PRINCIPI	Bonus Eventus steht frontal	ca. Mitte 113– August 114	429	3,23 g	6 Uhr
59 44	Denar	IMP TRAIANO AVG GER DAC P M TR P COS VI P P	S P Q R OPTIMO PRINCIPI	Bonus Eventus steht frontal	ca. Mitte 113– August 114	427	3,15 g	6 Uhr
60 46	Denar	IMP TRAIANO AVG GER DAC P M TR P COS VI P P	S P Q R OPTIMO PRINCIPI	Adler zwischen zwei Standar- ten	ca. Mitte 113– August 114	461	3,50 g	6 Uhr

TRAIAN, CONSULAT VI, nach der Annahme des Optimus-Namens (114–116 n. Chr.)

Nr.	Nominale	Averslegende	Reverslegende	Reverstyp (Zusatzleg.)	Datierung	Zitat BMC	Gewicht	Stempel- stellung
61 48	Denar	IMP CAES NER TRAIANO OPTIMO AVG GER DAC	P M TR P COS VI P P S P Q R	Mars geht nach rechts	ca. Herbst 114– Anfang 116	536	3,35 g	6 Uhr
62 49	Denar	IMP CAES NER TRAIANO OPTIMO AVG GER DAC	P M TR P COS VI P P S P Q R	Mars geht nach rechts	ca. Herbst 114– Anfang 116	536	2,89 g	6 Uhr
63 50	Denar	IMP CAES NER TRAIANO OPTIMO AVG GER DAC	P M TR P COS VI P P S P Q R	Mars geht nach rechts	ca. Herbst 114– Anfang 116	536	2,56 g	6 Uhr
64 51	Denar	IMP CAES NER TRAIANO OPTIMO AVG GER DAC	P M TR P COS VI P P S P Q R	Traianssäule	ca. Herbst 114– Anfang 116	566	3,44 g	7 Uhr
65 52	Denar	IMP CAES NER TRAIANO OPTIMO AVG GER DAC	P M TR P COS VI P P S P Q R	Fortuna sitzt nach links, FORT RED	ca. Herbst 114– Anfang 116	578	3,09 g	6 Uhr

TRAIAN, CONSULAT VI, nach der Annahme des Parthicus-Namens (116–117 n. Chr.)

Nr.	Nominale	Averslegende	Reverslegende	Reverstyp (Zusatzleg.)	Datierung	Zitat BMC	Gewicht	Stempel- stellung
66 53	Denar	IMP CAES NER TRAIAN OPTIM AVG GER DAC PARTHICO	P M TR P COS VI P P S P Q R	Felicitas steht nach links	ca. Februar 116– Mitte 116	599	3,18 g	7 Uhr
67 54	Denar	IMP CAES NER TRAIAN OPTIM AVG GERM DAC	PARTHICO P M TR P COS VI P P S P Q R	Virtus steht nach rechts	ca. Mitte 116– August 117	631	3,23 g	7 Uhr
68 55	Denar	IMP CAES NER TRAIAN OPTIM AVG GERM DAC	PARTHICO P M TR P COS VI P P S P Q R	Fortuna sitzt nach links, FORT RED	ca. Mitte 116– August 117	634	3,15 g	6 Uhr

TRAIAN, PROVINZIALKURANT

Nr.	Nominale	Averslegende	Reverslegende	Reverstyp	Datierung	Zitat Syd.*	Gewicht	Stempel- stellung
69 56	Drachme	AYTOKP KAIC NEP TPAIAN CEB IEPM ΔAK	ΔHMAPX EE IZ(?) YIIAT Ϛ	Arabia steht nach links	Dezember 112– Dezember 113 (?)	185 (?)	3,20 g	6 Uhr

TRAIAN, ANTIKE FALSA

Nr.	Nominale	Averslegende	Reverslegende	Reverstyp (Zusatzleg.)	Datierung	Zitat BMC	Gewicht	Stempel- stellung
70 57	(Denar), AE-Guss	IMP TRAIANO AVG GER DAC P M TR P	COS V P P S P Q R OPTIMO PRINC	Aeternitas steht frontal, AET AVG	111	(374)	3,30 g	7 Uhr
71 59	(Denar), plattiert	IMP CAES NER TRAIANO OPTIMO AVG GER DAC	P M TR P COS VI P P S P Q R	Virtus steht nach rechts	ca. Herbst 114– Anfang 116	(559)	2,50 g	6 Uhr

8.2 μ -XRF and μ -SRXRF Results of Previous Work

Table 8.2: Results of μ -XRF and μ -SRXRF analysis of the Roman denarii: [3]

	Coin no.	μ -XRF				μ -SRXRF				
		Ag%	Cu%	Au%	Pb%	Ag%	Cu%	Au%	Pb%	Bi%
Nerva	1	87,00	12,70	0,13	0,22	88,22	11,05	0,20	0,52	0,00
	2	93,20	6,50	0,13	0,21	93,67	5,67	0,22	0,43	0,00
	3	86,20	13,40	0,17	0,26	87,82	11,33	0,25	0,59	0,00
Trajan COS II	4	85,30	14,30	0,18	0,22	86,90	12,30	0,27	0,52	0,00
	5	68,30	13,30	0,15	0,21	87,88	11,37	0,23	0,52	0,00
	6	85,50	14,20	0,15	0,19	86,54	12,71	0,22	0,45	0,06
	7	88,90	10,70	0,24	0,17	92,59	6,57	0,45	0,38	0,00
	8					88,87	10,36	0,40	0,35	0,00
	9	88,50	11,20	0,02	0,24	89,54	9,83	0,00	0,58	0,01
	10	86,80	12,70	0,24	0,19	87,97	11,19	0,40	0,42	0,00
	11	93,70	6,00	0,27	0,14	93,98	5,23	0,48	0,29	0,00
11	94,00	5,60	0,00	0,26	94,75	4,57	0,00	0,61	0,05	
Trajan COS III	12	79,10	20,70	0,03	0,25	81,07	18,21	0,03	0,64	0,03
	13	78,30	21,30	0,03	0,30	80,26	18,92	0,03	0,74	0,04
	14	77,90	21,80	0,07	0,16	79,51	19,89	0,09	0,40	0,11
	15	77,10	22,70	0,16	0,19	78,70	20,58	0,24	0,43	0,00
Trajan COS IV	16	77,10	22,50	0,22	0,21	79,55	19,60	0,33	0,51	0,00
	17	78,70	20,80	0,07	0,27	80,26	18,98	0,09	0,65	0,01
	18	80,30	19,50	0,13	0,21	81,12	18,19	0,20	0,47	0,00
	19	92,50	7,00	0,25	0,23	93,21	5,85	0,43	0,50	0,00
	20	79,00	20,70	0,16	0,24	80,95	18,27	0,23	0,53	0,00
	21	79,40	20,30	0,11	0,20	80,30	19,11	0,16	0,41	0,00
	22	81,50	18,10	0,27	0,05	83,54	15,69	0,06	0,68	0,03
	23	80,10	19,50	0,16	0,21	82,55	16,73	0,23	0,48	0,00
	24	82,40	17,20	0,07	0,27	84,03	15,17	0,10	0,68	0,01
	25	78,00	21,80	0,13	0,25	80,32	18,91	0,17	0,59	0,00
	26	77,60	22,00	0,14	0,22	80,28	18,99	0,20	0,52	0,00
	27	79,00	20,50	0,08	0,25	80,76	18,47	0,12	0,64	0,00
	28	78,60	21,00	0,00	0,26	80,81	18,48	0,00	0,67	0,02
29	78,80	21,00	0,00	0,25	80,94	18,32	0,00	0,63	0,09	

Coin no.	μ -XRF				μ -SRXRF					
	Ag%	Cu%	Au%	Pb%	Ag%	Cu%	Au%	Pb%	Bi%	
Trajan COS V	30	93,70	6,00	0,13	0,29	93,60	5,47	0,19	0,72	0,00
	31	78,00	21,70	0,07	0,25	80,14	19,11	0,08	0,65	0,00
	32	78,30	21,50	0,00	0,20	80,70	18,69	0,00	0,55	0,04
	33	81,30	18,70	0,00	0,23	83,28	16,09	0,00	0,58	0,02
	34	80,10	19,70	0,00	0,33	82,99	16,15	0,00	0,81	0,03
	35	79,80	20,00	0,04	0,28	82,43	16,78	0,04	0,71	0,03
						92,58	6,51	0,05	0,82	0,03
	36	80,30	19,30	0,03	0,29	83,24	15,93	0,04	0,72	0,07
	37	80,30	19,30	0,00	0,29	82,61	16,63	0,00	0,73	0,01
	38	78,80	21,00	0,03	0,24	81,00	18,37	0,03	0,58	0,01
	39	80,30	19,30	0,05	0,39	83,62	15,34	0,04	0,99	0,00
	40	82,40	17,30	0,05	0,24	91,33	7,94	0,08	0,64	0,00
	41	91,90	7,70	0,06	0,32	92,48	6,59	0,08	0,82	0,02
	42	79,40	20,30	0,00	0,34	82,87	16,20	0,00	0,84	0,08
	43	87,50	12,20	0,00	0,31	86,05	12,99	0,00	0,86	0,09
						90,62	8,35	0,00	0,92	0,10
	44	79,60	20,00	0,05	0,25	81,83	17,49	0,06	0,59	0,02
	45	80,90	18,80	0,06	0,29	92,02	7,03	0,10	0,82	0,02
						81,88	17,27	0,07	0,75	0,01
	46	77,90	21,80	0,00	0,36	81,26	17,70	0,02	0,92	0,09
	47	78,60	20,70	0,00	0,55	83,25	15,27	0,00	1,41	0,06
	48	92,40	7,30	0,00	0,28	93,54	5,63	0,03	0,72	0,07
	49	91,20	8,50	0,06	0,30	92,70	6,48	0,09	0,69	0,03
	50	77,50	22,00	0,00	0,33	80,19	18,87	0,00	0,86	0,07
	51	79,90	19,50	0,05	0,29	82,54	16,62	0,06	0,74	0,03
	52	79,80	19,90	0,04	0,33	82,06	17,01	0,05	0,85	0,02
	53	77,30	22,30	0,14	0,21	79,96	19,18	0,10	0,71	0,04
	54	80,30	19,50	0,00	0,31	82,59	16,52	0,00	0,82	0,05
	55	78,60	21,20	0,05	0,20	79,92	19,51	0,05	0,38	0,12
Trajan COS VI	56	76,70	23,00	0,03	0,28	79,23	20,00	0,02	0,71	0,03
	57	87,90	11,90	0,02	0,25	90,04	9,11	0,00	0,63	0,19
	58	78,80	20,80	0,00	0,27	81,58	17,68	0,00	0,65	0,07
	59	78,80	20,80	0,09	0,26	81,82	17,33	0,13	0,70	0,00
	60	79,80	19,70	0,00	0,32	82,35	16,71	0,02	0,81	0,10
	61	78,90	20,80	0,03	0,22	80,77	18,59	0,04	0,52	0,07
	62	93,90	5,70	0,28	0,15	93,41	5,65	0,24	0,70	0,00
	63	79,30	20,70	0,00	0,27	82,45	16,68	0,00	0,76	0,08
	64	79,70	20,00	0,03	0,34	82,34	16,67	0,04	0,88	0,07
	65	78,20	21,50	0,00	0,32	81,36	17,78	0,00	0,82	0,02
	66	79,90	19,70	0,07	0,31	82,04	16,99	0,10	0,81	0,05
	67	77,40	22,30	0,04	0,33	80,27	18,79	0,03	0,87	0,02
	68	78,10	21,50	0,07	0,33	80,38	18,61	0,08	0,82	0,10

8.3 Binary Ag/Cu Mixture

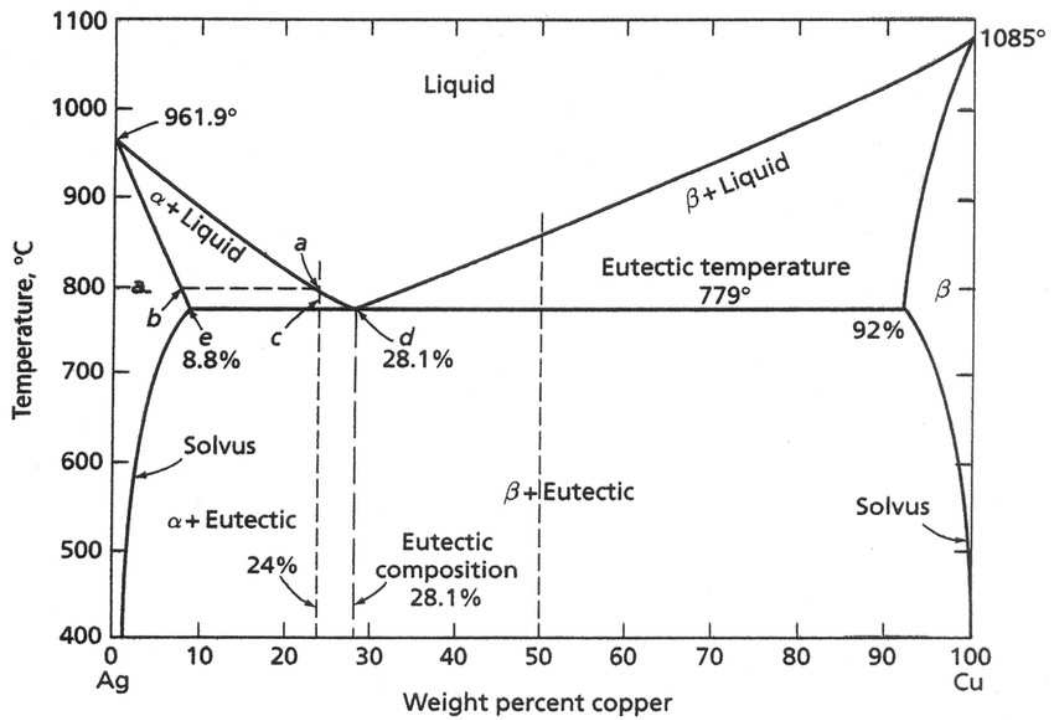


Figure 8.1: Binary phase diagram Ag/Cu [33].

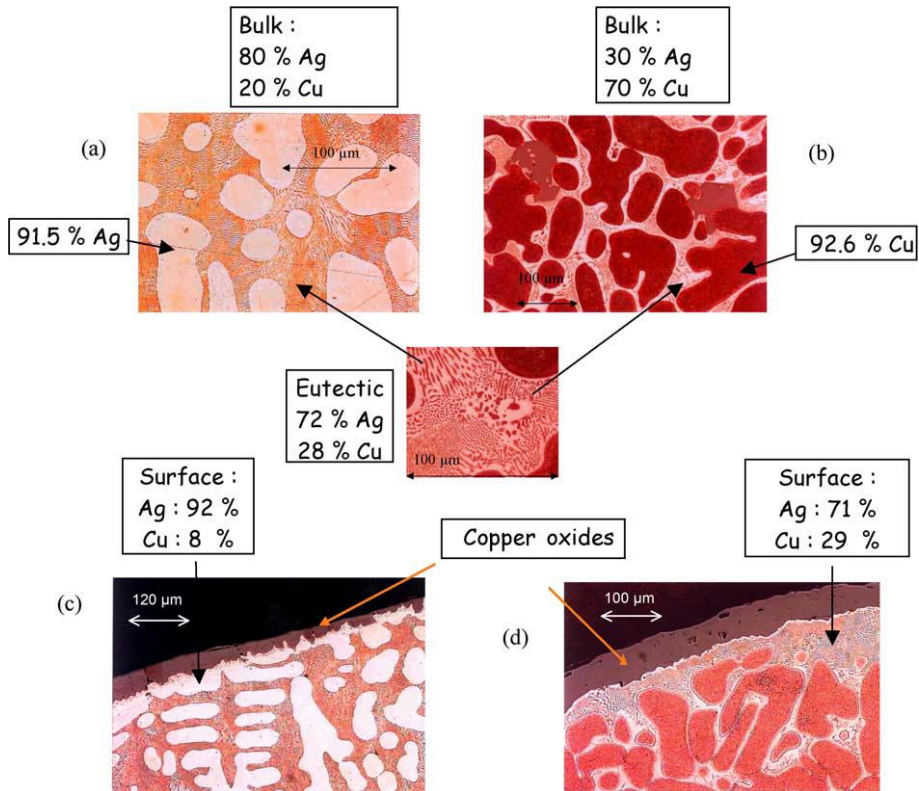
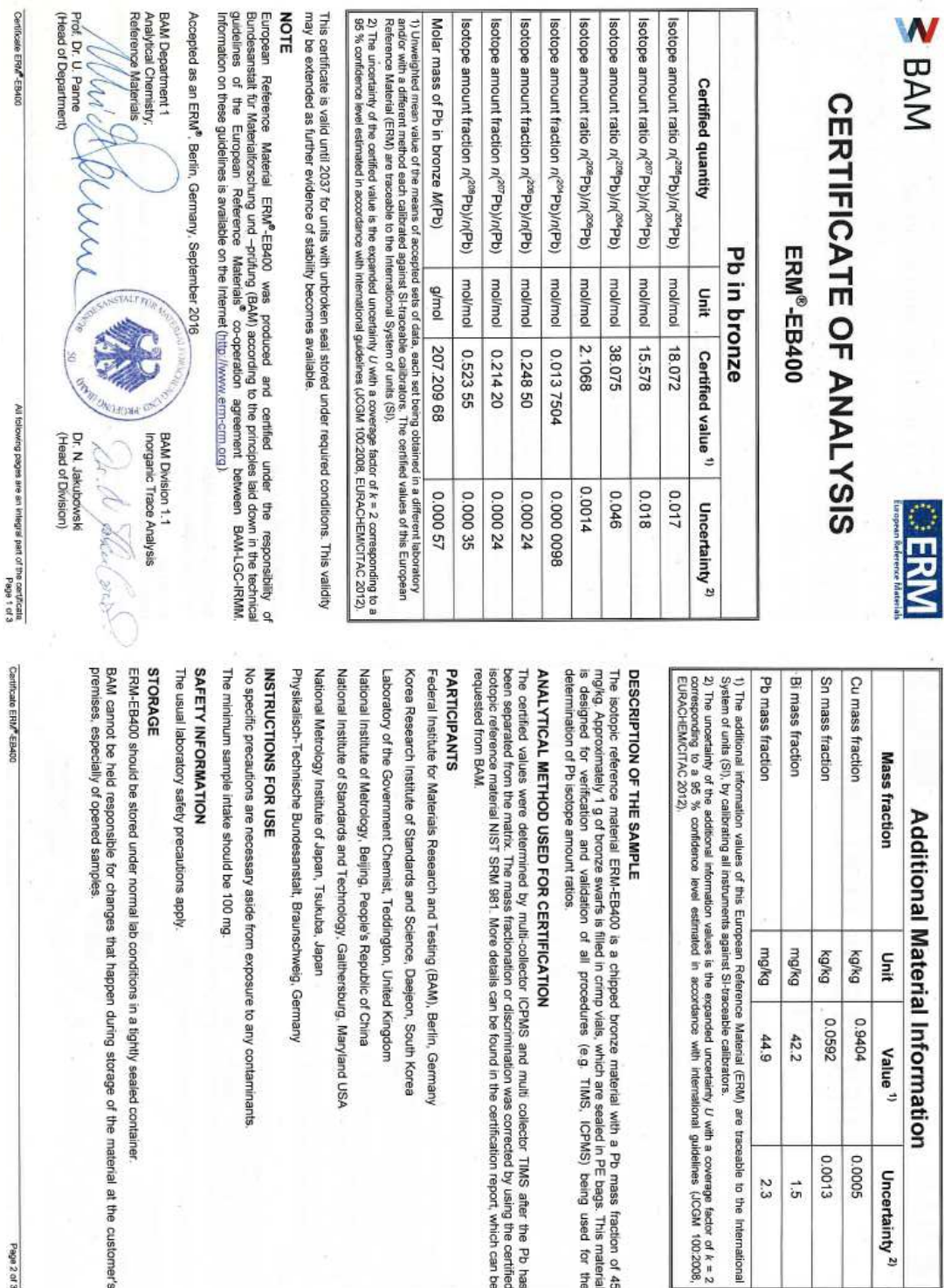


Figure 8.2. Metallographic microstructure of two silver-copper alloys. (a) and (c): core and surface of an 80 % Ag – 20 % Cu alloy. (b) and (d): core and surface of an 30 % Ag – 70 % Cu alloy [34].

8.4 Certificates of Purchased Reference Materials



Additional Material Information

Mass fraction	Unit	Value ¹⁾	Uncertainty ²⁾
Cu mass fraction	kg/kg	0.9404	0.0005
Sn mass fraction	kg/kg	0.0592	0.0013
Bi mass fraction	mg/kg	42.2	1.5
Pb mass fraction	mg/kg	44.9	2.3

1) The additional information values of this European Reference Material (ERM) are traceable to the International System of units (SI), by calibrating all instruments against SI-traceable calibrators.
2) The uncertainty of the additional information values is the expanded uncertainty U with a coverage factor of k = 2 corresponding to a 95 % confidence level estimated in accordance with international guidelines (JCGM 100:2008, EURACHEM/CITAC 2012).

DESCRIPTION OF THE SAMPLE
The isotopic reference material ERM-EB400 is a chipped bronze material with a Pb mass fraction of 45 mg/kg. Approximately 1 g of bronze swarfs is filled in crimp vials, which are sealed in PE bags. This material is designed for verification and validation of all procedures (e.g. TIMS, ICP-MS) being used for the determination of Pb isotope amount ratios.

ANALYTICAL METHOD USED FOR CERTIFICATION
The certified values were determined by multi-collector ICP-MS and multi collector TIMS after the Pb has been separated from the matrix. The mass fractionation or discrimination was corrected by using the certified isotopic reference material NIST SRM 981. More details can be found in the certification report, which can be requested from BAM.

PARTICIPANTS
Federal Institute for Materials Research and Testing (BAM), Berlin, Germany
Korea Research Institute of Standards and Science, Daejeon, South Korea
Laboratory of the Government Chemist, Teddington, United Kingdom
National Institute of Metrology, Beijing, People's Republic of China
National Institute of Standards and Technology, Gaithersburg, Maryland USA
National Metrology Institute of Japan, Tsukuba, Japan
Physikalisch-Technische Bundesanstalt, Braunschweig, Germany

INSTRUCTIONS FOR USE
No specific precautions are necessary aside from exposure to any contaminants.
The minimum sample intake should be 100 mg.

SAFETY INFORMATION
The usual laboratory safety precautions apply.

STORAGE
ERM-EB400 should be stored under normal lab conditions in a tightly sealed container.
BAM cannot be held responsible for changes that happen during storage of the material at the customer's premises, especially of opened samples.

Certificate ERM®-EB400

Page 2 of 3

Figure 8.3: Certificate of the reference material ERM-EB400.

CERTIFICATE OF ANALYSIS

133X AGA1 (batch A)

Reference Material Information

Type: Archaeological Silver
Form and Size: Disc, 25mm diameter
Produced by: Mayhan & Co Ltd
Analysed by: Birmingham Assay Office
Certified and supplied by: MBH Analytical Ltd

Assigned Values

Element by weight, % or µg/g (ppm)

Element	Cu	Pb	Au	Zn	Sn	Sb	Bi	Fe
percent %	19.95	0.207	1.48	0.211	0.291	0.050	0.194	0.039
uncertainty	0.21	0.007	0.03	0.005	0.010	0.001	0.006	0.001

Element	Al	As	Cd	Co	Cr	Ge	In	Mg	Mn
ppm	96	255	165	406	20	107	37	45	61
uncertainty	4	9	3	7	2	15	4	2	1

Element	Ni	Pd	Pt	Rh	Se	Si	Ti	Te
ppm	118	54	67	16	169	91	79	271
uncertainty	3	0	1	0	5	3	10	6

Notes

This sample was prepared by induction melting and chill-casting; the resultant ingot was rolled into strip of 3mm thickness.

The above values have been derived by one competent laboratory (UKAS accreditation 0667) only, using ICP-AES for all elements. Each value is a mean of four independent tests. The uncertainty value stated is the standard deviation of those results. All values should be treated with due caution.

The manufacture, analysis and certification of this product were supervised by C Eveleigh, PhD, Technical Director, MBH Analytical Ltd.

The material to which this certificate of analysis refers is supplied subject to our general conditions of sale.

Certified by:

MBH ANALYTICAL LIMITED _____ on 14th July 2014
C Eveleigh

Registered in England, No 1875653 • Registered Office: Holland House, Queens Road, Barnet, EN5 4DJ

Figure 8.4: Certificate of the reference material 133X AGA1.

List of Tables

Table 2.1: Laser sources used in LIBS: [13].....	18
Table 2.2: Medium abundance of lead isotopes: [29].....	30
Table 3.1: Used reference materials (numbering refers to Figure 3.4):	33
Table 3.2: Used chemicals:	33
Table 3.3: Sample intakes and resulting concentrations:	34
Table 3.4: Dilution series of dissolved reference materials:	34
Table 3.5: For S/N optimisation varied measurement parameters:	35
Table 3.6: Measurement parameters of the profilometer:	36
Table 3.7: Imaging parameters:.....	36
Table 3.8: Standard LA – parameters for signal check and optimisation:.....	37
Table 3.9: Liquid measurement parameters:	38
Table 3.10: LA – parameters of different line scans:.....	38
Table 3.11: LA – parameters of all line scans:	39
Table 3.12: ICP-MS – sample measurement parameters:.....	39
Table 3.13: Measurement sequence for Tandem – LIBS/LA-ICP-MS experiments:	39
Table 4.1: Optimised LIBS parameters:	41
Table 4.2: Average crater-depth and standard deviation (3 replicates):	45
Table 4.3: Results of μ -XRF and μ -SRXRF in previous work: [3]	48
Table 4.4: Natural Abundances of relevant mercury isotopes: [39]	61
Table 4.5: Δ - values for linear interpolation of lead isotope signals (Equation 5):	62
Table 4.6: Results, measured and calculated values of liquid BAM measurements:.....	64
Table 4.7: Measured and corrected values of liquid MBH measurements:.....	65
Table 4.8: Pb-isotope ratios and relative errors of the in Figure 4.25 shown selected coins with consulates and times of origin:	69
Table 8.1: Analysed Roman denarii: [4]	80
Table 8.2: Results of μ -XRF and μ -SRXRF analysis of the Roman denarii: [3]	86

List of Figures

Figure 1.1: Map of the Roman Empire at its biggest expansion in 117 AD. [5]	13
Figure 1.2: Silver content of analysed coins with SEM-EDX. [4].....	14
Figure 2.1: LIBS instrumental setup [13].	16
Figure 2.2: Schematic construction of a solid state Nd:YAG laser [15].	19
Figure 2.3: Energy scheme for absorption (left) and spontaneous emission (right) [14].	19
Figure 2.4: Energy scheme for stimulated emission [14].	19
Figure 2.5: Schematic of Czerny-Turner- (left) and Echelle-spectrometer (right). S...entrance slit, P...spherical mirror, G...diffraction grating, D...detector. [13].....	21
Figure 2.6: Schematic LA-ICP-MS setup. [19]	22
Figure 2.7: Material ablation and aerosol formation after laser impact. [20]	23
Figure 2.8: Scheme of a typical plasma torch. [19]	24
Figure 2.9: Schematic diagram of a quadrupole mass analyser. [19]	26
Figure 2.10: Natural radioactive decay chains. [27].....	29
Figure 2.11: Bivariate plot – Isotopic ratios of Pb from different mining areas. [30]	30
Figure 3.1: Tandem J200 LIBS instrument (left), iCAP SQ-ICP-MS instrument (center) and NWR 213 LA unit (right).	31
Figure 3.2: Olympus GX51 microscope (left) and DektakXT profilometer (right).	31
Figure 3.3: Roman denarius: whole (left), cut through (center) [31] and embedded (right).	32
Figure 3.4: Reference Materials: pure metals and MBH (left), BAM - scraps as purchased and after embedding (right). Numbering refers to Table 3.1.	33
Figure 3.5: Microscopic image of coin no. 63 before (above) and after recording 5 layers of LIBS image (below).....	37
Figure 4.1: Microscopic images of selected coins in 50x magnification (left to right: no. 1, 12, 16, 27, 35, 45, 48, 62).....	40
Figure 4.2: Section of the LIBS reference spectra of pure metals with markings to the evaluated emission lines.	42
Figure 4.3: Microscopic image of coin no. 53 (COS V, approx. AD 110) with measurement spot marked as black circle. The corresponding spectra is shown in Figure 4.5 and enlarged sections of interest in Figure 4.5.....	43
Figure 4.4: Total LIBS spectra of coin no. 53 and MBH.	43
Figure 4.5: LIBS Spectra of the outer corrosion layer of a denarius (No. 53). The sections of interest for evaluated emission lines are magnified.	44
	92

Figure 4.6: Above: 2D-plot of craters on MBH. Below: line profile over craters of different number of laser pulses (left) and same number of laser pulses (right).	45
Figure 4.7: 3D-plot of craters on MBH.	45
Figure 4.8: User-interface for the definition of a spectral descriptor (top) and the chemical map editor (bottom) in ImageLab®.....	46
Figure 4.9: Microscopic images of the coins (no. 1, 2, 20, 39) used for comparison of the core alloy (Figure 4.10). The measured spots are marked by blue circles.....	47
Figure 4.10: Comparison of the alloy of the coin core. Evaluated emission lines (Ag, Cu, Au, Pb) of the coins no. 1, 2, 20 and 39 (Figure 4.9). The error bars represent two times the standard deviation (3 replicates). The abbreviation “K” stands for core (dt. Kern).....	48
Figure 4.11: Microscopic images of the coins (no. 22, 27, 45) used for comparison of the silver and copper content of the core with the inner and outer corrosion layer (Figure 4.12). The measured spots are marked by circles (blue...core, orange...inner layer, green...outer corrosion layer).....	50
Figure 4.12: Comparison of the silver and copper content of the core, the inner and the outer corrosion layer of the coins no. 22, 27 and 45 (Figure 4.11). The error bars represent two times the standard deviation (3 replicates). K...core (dt. Kern), R...inner layer (dt. Rand), RR...outer corrosion layer.	51
Figure 4.13: Evaluated emission lines (Na, Ca, K, Mg, Ba, Al, Si) of the outer corrosion layer of coin no. 53 (Figure 4.3, 5 measurements accumulated). The error bars represent two times the standard deviation.....	51
Figure 4.14: Coins no. 20 and 65 with markings on measured spots. The results are shown in Figure 4.15.....	52
Figure 4.15: Elements found in visible inhomogeneities in the coins no. 20 and 39. The coins and the measured spots are shown in Figure 4.14. The signal values that were below 10σ of the noise have been set to zero.....	53
Figure 4.16: Colour scale for the relative element concentrations in the LIBS images [a.u.].....	54
Figure 4.17: LIBS – Images: Elemental maps of coin no. 1 (Nerva, AD 97).....	55
Figure 4.18: LIBS – Images: Elemental maps of coin no. 39 (Traian COS V, approx. AD 107 – 108).	56
Figure 4.19: LIBS – Images: Elemental maps of coin no. 57 (Traian COS VI, AD 112).	57
Figure 4.20: LIBS – Images: Elemental maps of coin no. 61 (Traian COS VI, approx. AD 114 – 116). ...	58
Figure 4.21: Scheme for Data processing and evaluation.....	60
Figure 4.22: Scheme for interpolation of Pb-isotope-signals on an artificial transient signal.	62
Figure 4.23: Scheme for bracketing correction of instrumental bias and drift.....	64

Figure 4.24: Ratioplot ($^{206}\text{Pb}/^{207}\text{Pb}$ $^{206}\text{Pb}/^{204}\text{Pb}$) of LA-ICP-MS measurements of all coins and bracketing standard (MBH).	66
Figure 4.25: Ratioplot ($^{206}\text{Pb}/^{207}\text{Pb}$ $^{206}\text{Pb}/^{204}\text{Pb}$) of LA-ICP-MS measurements of a selection of coins and bracketing standard (MBH). Colouring refers to Table 4.8.	68
Figure 4.26: Coins no. 26, 45, 71, and 72 used for Tandem – LIBS/LA-ICP-MS measurements with measurement regions marked.	70
Figure 4.27: Comparison of the marked sections in the coins (Figure 4.26) measured with LIBS in Tandem setup. Evaluated emission lines (Ag, Cu, Au, Pb) of the coins no. 26, 45, 71 and 72. The colouring of the sample name surrounding circles refers to the marked measurement regions.	71
Figure 4.28: Ratioplot ($^{207}\text{Pb}/^{208}\text{Pb}$ $^{206}\text{Pb}/^{207}\text{Pb}$) of Tandem – LIBS/LA-ICP-MS measurements. The colouring refers to the marked measurement regions on the coin’s cross sections in Figure 4.26.	72
Figure 4.29: Example for the procedure of data combination of multiple methods.	74
Figure 8.1: Binary phase diagram Ag/Cu [33].....	88
Figure 8.2. Metallographic microstructure of two silver-copper alloys. (a) and (c): core and surface of an 80 % Ag – 20 % Cu alloy. (b) and (d): core and surface of an 30 % Ag – 70 % Cu alloy [34].....	88
Figure 8.3: Certificate of the reference material ERM-EB400.....	89
Figure 8.4: Certificate of the reference material 133X AGA1.	90

List of Equations

Equation 1: Background subtraction.....	61
Equation 2: Hg correction of ^{204}Pb	61
Equation 3: Correct ratio determination. $x,y=4$; $x,y=6$; $x,y=7$; $x,y=8$; $x\neq y$	61
Equation 4: ^{202}Hg – Interpolation.	62
Equation 5: ^{20x}Pb – Interpolation, $x=4$; $x=6$; $x=8$	62
Equation 6: Condition for spike elimination.....	62
Equation 7: Linear model for mass bias correction [40].	63

Bibliography

- [1] M. Beard, *SPQR. Die tausendjährige Geschichte Roms*. Frankfurt am Main: S. Fischer, 2016.
- [2] M. Rodrigues *et al.*, "Further metallurgical analyses on silver coins of Trajan (AD 98-117)," *J. Anal. At. Spectrom.*, vol. 26, no. 5, pp. 984–991, 2011.
- [3] M. Rodrigues, "Analytical Chemistry for Cultural Heritage: Material analysis of archeological silver coins using X-ray based techniques," Vienna University of Technology, 2011.
- [4] K. Uhlir, B. Woytek, M. Schreiner, M. Alram, and M. Grießer, "Metallanalytische Forschungen zur Denarprägung Kaiser Traians (98-117 n. Chr.)," Vienna: Kunsthistorisches Museum Wien, 2007.
- [5] "Roman Empire AD 117." [Online]. Available: https://de.m.wikipedia.org/wiki/Datei:Roman_Empire_Trajan_117AD.png. [Accessed: 06-Jun-2019].
- [6] P. Grierson, *Numismatics*. Oxford: Oxford University Press, 1975.
- [7] G. Artioli, *Scientific Methods for Cultural Heritage*. Oxford University Press, 2010.
- [8] T. Mommsen, *Geschichte des römischen Münzwesens*. Berlin: Weidmann, 1860.
- [9] J. Hammer, "Der Feingehalt der griechischen und römischen Münzen. Ein Beitrag zur antiken Münzgeschichte," Universität Tübingen, 1906.
- [10] D. R. Walker, *The Metrology of the Roman Silver Coinage*. Oxford, 1978.
- [11] K. Butcher and M. Ponting, "The Roman denarius under the Julio-Claudian emperors: Mints, metallurgy and technology," *Oxford J. Archaeol.*, vol. 24, pp. 163–197, 2005.
- [12] T. H. MAIMAN, "Stimulated Optical Radiation in Ruby," *Nature*, vol. 187, p. 493, Aug. 1960.
- [13] S. Musazzi and U. Perini, *Laser-Induced Breakdown Spectroscopy*. Milan: Springer, 2014.
- [14] "Nd:YAG laser." [Online]. Available: <https://www.physics-and-radio-electronics.com/physics/laser/ndyaglaser.html>. [Accessed: 13-Jun-2019].
- [15] N. D Bahar, S. Marimuthu, and W. Yahya, "Pulsed Nd: YAG laser drilling of aerospace materials (Ti-6Al-4V)," *IOP Conf. Ser. Mater. Sci. Eng.*, vol. 152, p. 12056, 2016.
- [16] "Frequenzvervielfachung," *Lexikon der Physik*, 1998. [Online]. Available: <https://www.spektrum.de/lexikon/physik/frequenzvervielfachung/5342>. [Accessed: 13-Jun-2019].

- [17] "Atomic Emission Spectroscopy." [Online]. Available: https://en.wikipedia.org/wiki/Atomic_emission_spectroscopy. [Accessed: 04-Jun-2019].
- [18] "The 30-Minute Guide to ICP-MS." [Online]. Available: http://www.quimlab.com.br/PDF-LA/icp_ms_artigo_perkin_elmer.pdf. [Accessed: 04-Jun-2019].
- [19] S. J. Hill, A. J. Handley, and J. M. Chalmers, *Inductively Coupled Plasma Spectrometry and its Applications*. Plymouth, UK: Blackwell Publishing Ltd, 2007.
- [20] B. Hattendorf and D. Günther, "LA Short course," 2019.
- [21] G. D. Flesch and H. J. Svec, "International Review of Science (Mass Spectrometry)," *Phys. Chem.*, vol. 5, 1975.
- [22] F. Vanhaecke and P. Degryse, *Isotopic Analysis - Fundamentals and Applications Using ICP-MS*, no. March. Wiley-VCH, 2012.
- [23] K. G. Heumann, S. M. Gallus, G. Rädlinger, and J. Vogl, "Precision and accuracy in isotope ratio measurements by plasma source mass spectrometry," *J. Anal. At. Spectrom.*, vol. 13, no. 9, pp. 1001–1008, 1998.
- [24] J. R. Dean, *Practical Inductively Coupled Plasma Spectroscopy*, vol. 8. West Sussex: John Wiley & Sons, Ltd, 2005.
- [25] H. Krieger, *Strahlenphysik*, 4th ed. Springer, 1998.
- [26] "Lead." [Online]. Available: <https://de.wikipedia.org/wiki/Lead>. [Accessed: 11-Feb-2019].
- [27] C. M. Lederer, J. M. Hollander, and I. Perlman, *Table of Isotopes*, 6th ed. New York: John Wiley & Sons, Ltd, 1968.
- [28] M. Resano, P. Marzo, J. Pérez-Arantegui, M. Aramendía, C. Cloquet, and F. Vanhaecke, "Laser ablation-inductively coupled plasma-dynamic reaction cell-mass spectrometry for the determination of lead isotope ratios in ancient glazed ceramics for discriminating purposes," *J. Anal. At. Spectrom.*, vol. 23, no. 9, pp. 1182–1191, 2008.
- [29] J. Meija *et al.*, "Isotopic compositions of the elements 2013 (IUPAC Technical Report)," *Pure Appl. Chem.*, vol. 88, pp. 293–306, 2016.
- [30] G. Fortunato, A. Ritter, and D. Fabian, "Old Masters' lead white pigments: investigations of paintings from the 16th to the 17th century using high precision lead isotope abundance ratios," *Analyst*, vol. 130, no. 6, pp. 898–906, 2005.
- [31] K. Uhlir, E. Bidaud, M. Mäder, and M. Schreiner, "Naturwissenschaftliche Analyse an Münzen

des römischen Kaisers Traian,” Vienna, 2006.

- [32] A. Kramida, K. Olsen, and Y. Ralchenko, “NIST LIBS Database.” [Online]. Available: <https://physics.nist.gov/PhysRefData/ASD/LIBS/lib-form.html>. [Accessed: 14-Jun-2019].
- [33] S. Taylor, “An investigation of the mechanical and physical properties of copper-silver alloys and the use of these alloys in Pre-Columbian America,” 2013.
- [34] L. Beck, S. Besonnet, S. Réveillon, D. Eliot, and F. Pilon, “Silver surface enrichment of silver-copper alloys: A limitation for the analysis of ancient silver coins by surface techniques,” *Nucl. Instruments Methods Phys. Res. Sect. B Beam Interact. with Mater. Atoms*, vol. 226, no. 1–2, pp. 153–162, 2004.
- [35] G. Van der Snickt, W. De Nolf, B. Vekemans, and K. Janssens, “ μ -XRF/ μ -RS vs. SR μ -XRD for pigment identification in illuminated manuscripts,” *Applied Phys. A*, vol. 92, no. 1, pp. 59–68, 2008.
- [36] O. F. Vyvenko, T. Buonassisi, A. A. Istratov, E. R. Weber, M. Kittler, and W. Seifert, “Application of synchrotron-radiation-based x-ray microprobe techniques for the analysis of recombination activity of metals precipitated at Si/{SiGe} misfit dislocations,” *J. Phys. Condens. Matter*, vol. 14, no. 48, pp. 13079–13086, Nov. 2002.
- [37] C. E. Housecroft and A. G. Sharpe, *Anorganische Chemie*. München: Pearson Studium, 2006.
- [38] W. A. Deer, R. A. Howie, W. S. Wise, and J. Zussman, *Rock-forming minerals. Framework silicates: silica minerals, feldspathoids and the zelites*. Bath: Geological Society, Geological Society Publishing House, 2004.
- [39] J. Meija *et al.*, “Atomic weights of the 2013 (IUPAV Technical Report),” *Pure Appl. Chem.*, vol. 88, no. 3, pp. 265–291, 2015.
- [40] J. S. Begley and B. L. Sharp, “Characterisation and Correction of Instrumental Bias in Inductively Coupled Plasma Quadrupole Mass Spectrometry for Accurate Measurement of Lead Isotope Ratios,” *J. Anal. At. Spectrom.*, vol. 12, pp. 395–402, 1997.